Continental Arc Processes in British Columbia and Earthquake Processes in Virginia: Insights from Seismic Imaging

Kai Wang

Dissertation submitted to the faculty of the Virginia Polytechnic Institute and State University in partial fulfillment of the requirements for the degree of Doctor of Philosophy In Geosciences

John A. Hole, Chair

Esteban Gazel

Robert J. Tracy

Ying Zhou

January 9th, 2014

Blacksburg, VA

Keywords: Batholith, Travel Time Tomography, Mafic Garnet Granulite, Reverse Time Migration, Aftershocks.

Continental Arc Processes in British Columbia and Earthquake Processes in Virginia: Insights from Seismic Imaging

Kai Wang

ABSTRACT

Travel times from a refraction and wide-angle reflection seismic survey across the Coast Plutonic Complex and Stikine terrane of British Columbia were inverted to derive two dimensional P and S-wave seismic velocity models of the crust and uppermost mantle. A felsic upper crust and a felsic to intermediate middle crust are observed in both the batholith complex and the accreted Stikine island arc terrane. The P and S wave models demonstrate a high-velocity (P 7.0 km/s, S 3.8 km/s) layer in the lower crust beneath the youngest (late Cretaceous to Eocene) portion of the continental arc complex. In contrast, the lower crust under the Stikine terrane has lower velocities consistent with amphibolite or other hydrated mafic rocks. The Moho is at ~35 km depth under the Stikine terrane, deepens to ~38 km beneath the youngest portion of the arc, then shallows towards the coast. The high velocity zone under the younger portion of the Coast Plutonic Complex has a 1.81 Vp/Vs ratio and is interpreted to have a bulk composition of mafic garnet granulite. This garnet granulite and large volumes of granodiorite-dominated melt were created by arc dehydration melting of amphibolite (or hydrated gabbro) in the pre-existing lower crust

Reverse time migration method was applied to image aftershocks recorded by a dense array deployed after the 2011 Virginia earthquake. Events as tiny as magnitude -2 were successfully imaged as point sources. The propagation of energy release as a function of time and space was observed for events larger than magnitude 2.5. Spatial resolution of the images was ~200 m, which synthetic data tests show was primarily limited by the temporal sampling rate. Improved temporal and spatial sampling could produce images with sharper resolution.

ACKNOWLEDGEMENT

I would like to express my sincere appreciation to my Ph.D. advisor Dr. John. A. Hole for his support on my research in the past five years, for his professional advice on my research, for his consideration during the tough days when I face to the illness, for his patience, motivation, enthusiasm, and immense knowledge. His wonderful guidance helped me in all the time of research during the past five years and writing of this thesis.

I really appreciate the professional sprit of Dr Hole, he put all his energy on the research and teaching, which benefit me a lot in the past five years on my research. His high enthusiasm and hard-work on research impressed me very much and will be very helpful in my future career. I appreciate his patience on my study and research. He spent a lot of time on modifying my papers, advising my research, practicing presentation with me. During the period I struggling with the illness, his consideration and help support me to go through the hard times.

I would also like to thank my committee member Dr Ying Zhou, who gave me a lot of important suggestions during my research, which greatly improved my study. As the only Chinese professor in my committees, she also helped me to be familiar with the new style of research as a new Chinese student.

My sincere thank also goes to Dr Robert Tracy and Dr Esteban Gazel as my committee members. As two famous petrologists, both of them give very good suggestion and advise on petrology part of my first project. Their professional ideas greatly improved the interpretation part of my papers on batholith arc process. Dr Tracy's petrology class give me very basic but useful background on petrology area.

I would like to appreciate the fund from NSF for the Batholith Project and I appreciate the help from Dr G.D. Spence and his student A. L. Stephenson from University of Victoria, Dr K.C. Miller from Texas A&M University, Dr R.M. Clowes from University of British Columbia and Dr C. L. Andronicos from Purdue University, they are the co-authors for the Chapter 2 and Chapter 3. My thanks also give to all the volunteers from different universities who did the field work for us during the summer 2009.

I would like to appreciate the help from Dr Martin Chapman and graduate student Kathy Davenport from Virginia Tech, Dr Larry Brown and his student D. A. Quiros from Cornell University who are the co-authors for Chapter 4.

I would like to appreciate the help and instructions I get from Dr Martin Chapman and Jake Bale. Their professional knowledge and suggestion save me a lot of time during my research.

I would like to thank all the colleagues in the Geophysics group, I appreciate the help, and instructions they give to me. My fellow students Kathy Davenport, Ellen Gilliland, Pavithra Sekhar, Kate Craft, Sharmin Shamsalsadati, Eric Kazlaukas, Samuel Fortson, Karina Cheung, Oluyinka Oyewumi, Tannistha Maiti, Aida Farough, Shreya Singh, and Cable Warren, are always fun to talk with.

I would like to thank administrative staff, Connie Lowe, Ellen Mathena, Mary McMurray, and Linda Bland for their kind assistance, and Mark Lemon for their technical support in the past five years.

At the end, I would like to appreciate the endless support I get from my parents and my wife. They never give up to support me even when I face to the edge of death. It is them who

helped me in both life and spirit to go through the very hard time in my life. I accept that I lost a lot during the past five years. However, I never lose the confident that the god will stay with me forever, because he has already give a lot of things which is much more than what I lost.

Table of Contents

List of Figures

List of Tables

Chapter 1. Introduction

1.1 Seismic Investigation of Continental Arc Processes in British Columbia, western Canada

The generation and evolution of continental crust is a fundamental and socially relevant topic in geoscience. All crust derives from partial melt of the mantle. The dominant magma from the mantle is basaltic, or equivalently, gabbroic, and this is the composition of oceanic crust. However, the bulk composition of the continental crust is mainly andesitic in the middle and upper crust level with granulite faces rock compositions dominating the lower crust level [*Christensen and Fountain*, 1975; *Christensen*, 1996]. Continental subduction-zone magmatic arcs are the primary location at which large volumes of andesitic, or equivalently, granitoid rocks are created by partial melt of a gabbroic protolith. However, in order to generate the granitoid magmas, a complementary ultra-mafic residue is required. The fate of the residue is key to the formation of continental crust. Two hypotheses exist for the fate of the residue [*Kay and Mahlburg-Kay*, 1991; *Kay and Mahlburg Kay*, 1993]. It may hide below the geophysical Moho, above the petrological Moho, because the expected residue has similar geophysical properties to upper mantle rocks. On the other hand, it may be delaminated to sink back into the upper mantle because of its slightly heavier density. Delamination may occur during collapse of the arc or after subduction stops [*Herzberg et al.*, 1983; *Ducea and Saleeby*, 1998].

To investigate the fate of the residue, the multidisciplinary Batholiths project was initiated to study the Coast Plutonic Complex (CPC), also called the Coast Mountains Batholith,

of British Columbia in western Canada. The Jurassic to Eocene CPC is the largest Phanerozoic arc complex, and was generated by several pulses of magmatism during rapid subduction of Pacific basin plates beneath the North American margin [*Monger et al.*, 1982; *Armstrong*, 1988]. Post-subduction extension and exposure of the arc to mid-crustal depths makes it an ideal place to investigate the process of crustal evolution. Batholiths collaborative studies included structural geology, metamorphic and igneous petrology, geochemistry and geochronology, broadband seismology using global teleseisms, and controlled-source seismology.

As a part of the Batholith project, we acquired a seismic refraction and wide-angle reflection survey along a 400 km long line across the CPC and adjacent accreted terranes. Two-dimensional models of compressional P-wave (Chapter 2) and shear S-wave (Chapter 3) seismic velocity were built using tomographic inversion of observed travel times. These velocity models and the Vp/Vs ratio provide robust constraints on the lithology of the whole crust and upper mantle, and constrain evolution of arc continental crust.

1.2 Aftershock Imaging using Reverse Time Migration from the Dense AIDA Array Deployed after The 2011 Virginia Earthquake

Reverse time migration (RTM) is a proven and the most accurate method for imaging complicated subsurface structure in multichannel seismic reflection data [*Monger et al.*, 1982; *Baysal et al.*, 1983; *Mcmechan et al.*, 1985; *Chang and Mcmechan*, 1987; *Zhu and Lines*, 1998]. Early papers demonstrated the ability of RTM to image earthquakes from densely recorded wavefields [*Mcmechan et al.*, 1985]. A recent paper by Ishii et al. [2005] successfully applied

RTM to image a magnitude 9.8 subduction zone earthquake, and created a new excitement for the potential of the method [*Ishii et al.*, 2005; 2007; *Kiser et al.*, 2011]. Of particular interest to study earthquake rupture processes, the energy of the earthquake has been back-projected to the right location underground as a function of time, mapping slip propagation along the fault plane (e.g.,[*Ishii et al.*, 2007; *Kiser et al.*, 2011; *Koper et al.*, 2012]). Recently, RTM of earthquakes has also attracted industry attention to characterize hydraulic fracturing (e.g., [*Chambers et al.*, 2010; *Artman et al.*, 2010; *Zhebel and Eisner*, 2012]).

Challenges for RTM of earthquakes include the requirement to record the wavefield with dense spatial sampling, only possible with modern seismograph arrays. The success of RTM is more dependent than other migration imaging methods on the accuracy of the pre-existing seismic velocity model. Finally, RTM using the full wavefield is the most computationally intensive migration method. Recent approaches reduce the computation by a purely kinematic migration that ignores wavefield amplitude effects. However, recent successes demonstrate that both datasets and computation power have evolved so that RTM migration of earthquakes has become a powerful method to understand earthquake processes.

After the 2011 magnitude 5.8 Virginia earthquake, we deployed a densely sampled array, dubbed AIDA (Aftershock Imaging Using Dense Arrays), to record aftershocks. The reverse time migration method was applied to a few aftershocks from this dataset in Chapter 4. Very small earthquakes are successfully imaged in space and time without picking arrival times. For the largest aftershocks, rupture propagation was successfully imaged – at a scale that is orders of magnitude smaller than has previously been accomplished.

1.3 References

Armstrong, R. L. (1988), Mesozoic and early Cenozoic magmatic evolution of the Canadian Cordillera, *Geological Society of America Special Papers*, *218*, 55-92, doi:10.1130/SPE218-p55.

Artman, B., Podladtchikov, I., and Witten, B. (2010), Source location using time-reverse imaging, *Geophysical Prospecting*, *58*(5), 861-873.

Baysal, E., Kosloff, D., and Sherwood, J. (1983), Reverse time migration, *GEOPHYSICS*, *48*(11), 1514-1524, doi:doi:10.1190/1.1441434.

Chambers, K., Kendall, J., Brandsberg-Dahl, S., and Rueda, J. (2010), Testing the ability of surface arrays to monitor microseismic activity, *Geophysical Prospecting*, *58*(5), 821-830.

Chang, W., and Mcmechan, G. (1987), Elastic reverse-time migration, *GEOPHYSICS*, *52*(10), 1365-1375, doi:doi:10.1190/1.1442249.

Christensen, N. I. (1996), Poisson's ratio and crustal seismology, *J. Geophys. Res.*, *101*(B2), 3139-3156, doi:10.1029/95JB03446.

Christensen, N. I., and Fountain, D. M. (1975), Constitution of the Lower Continental Crust Based on Experimental Studies of Seismic Velocities in Granulite, *Geological Society of America Bulletin*, *86*(2), 227-236, doi:10.1130/0016-7606(1975)86<227:cotlcc>2.0.co;2.

Ducea, M. N., and Saleeby, J. B. (1998), The age and origin of a thick mafic–ultramafic keel from beneath the Sierra Nevada batholith, *Contr. Mineral. and Petrol.*, *133*(1-2), 169-185, doi:10.1007/s004100050445.

Ishii, M., Shearer, P. M., Houston, H., and Vidale, J. E. (2005), Extent, duration and speed of the 2004 Sumatra-Andaman earthquake imaged by the Hi-Net array, *Nature*, *435*(7044), 933-936, doi:http://www.nature.com/nature/journal/v435/n7044/suppinfo/nature03675_S1.html.

Ishii, M., Shearer, P. M., Houston, H., and Vidale, J. E. (2007), Teleseismic P wave imaging of the 26 December 2004 Sumatra-Andaman and 28 March 2005 Sumatra earthquake ruptures using the Hi-net array, *Journal of Geophysical Research: Solid Earth*, *112*(B11), B11307, doi:10.1029/2006JB004700.

Herzberg, C., Fyfe, W., and Carr, M. (1983), Density constraints on the formation of the continental Moho and crust, *Contr. Mineral. and Petrol.*, *84*(1), 1-5.

Kay, R., and Mahlburg-Kay, S. (1991), Creation and destruction of lower continental crust, *Geologische Rundschau*, *80*(2), 259-278.

Kay, R. W., and Mahlburg Kay, S. (1993), Delamination and delamination magmatism, *Tectonophysics*, *219*(1), 177-189.

Kiser, E., Ishii, M., Langmuir, C. H., Shearer, P. M., and Hirose, H. (2011), Insights into the mechanism of intermediate-depth earthquakes from source properties as imaged by back projection of multiple seismic phases, *Journal of Geophysical Research: Solid Earth*, *116*(B6), B06310, doi:10.1029/2010JB007831.

Mcmechan, G. A., Luetgert, J. H., and Mooney, W. D. (1985), Imaging of earthquake sources in Long Valley Caldera, California, 1983, *Bulletin of the Seismological Society of America*, *75*(4), 1005-1020.

Monger, J. W. H., Price, R. A., and Tempelman-Kluit, D. J. (1982), Tectonic accretion and the origin of the two major metamorphic and plutonic welts in the Canadian Cordillera, *Geology*, *10*(2), 70-75, doi:10.1130/0091-7613(1982)10<70:taatoo>2.0.co;2.

Zhebel, O., and Eisner, L. (2012), Simultaneous microseismic event localization and source mechanism determination, in *SEG Technical Program Expanded Abstracts 2012*, edited, pp. 1-5, Society of Exploration Geophysicists.

Zhu, J., and Lines, L. R. (1998), Comparison of Kirchhoff and reverse-time migration methods with applications to prestack depth imaging of complex structures, *Geophysics*, *63*(4), 1166-1176, doi:10.1190/1.1444416.

Chapter 2. Seismic Investigation of the Generation and Collapse of a Batholith Complex, Coast Mountains, Western Canada

2.1 Abstract

Travel times from a refraction and wide-angle reflection seismic survey across the Coast Plutonic Complex and Stikine terrane of British Columbia were inverted to derive a two dimensional seismic velocity model of the crust and uppermost mantle. East of the batholith complex, the Mesozoic Nechako sedimentary basin is underlain by crystalline rocks of the Stikine terrane with seismic velocities of <5 km/s extending to ~5 km depth. A seismic reflector is observed below the Stikine terrane at 20-22 km depth. The lower crustal velocity averages ~6.7 km/s, representative of an intermediate to mafic lithology interpreted to be accreted arc amphibolite. The Moho beneath Stikinia is at ~35 km depth and the underlying upper mantle has a velocity of ~8.1 km/s.

To the west, in the continental arc complex, velocities of 5-6.3 km/s indicate felsic plutonic rocks to >20 km depth. West of the Coast Shear Zone, beneath the Jurassic to mid-Cretaceous arc complex, felsic velocities (<6.6 km/s) continue to an eastward-dipping Moho at 30-33 km depth. East of the Coast Shear Zone, beneath the younger Cretaceous to Eocene arc complex, a strong seismic reflector and refractor is observed at ~27 km depth and a minor Moho root extends to ~37 km depth. Between the strong reflector and the Moho root, a high seismic

velocity of 7.0-7.1 km/s is observed. This high velocity is interpreted to indicate the presence of a mafic garnet granulite residual generated by dehydration melting of an amphibolitic protolith.

2.2 Introduction

The large volume of granitic batholiths created by magmatic differentiation in arcs above subduction zone makes continental crust more felsic than the original materials derived from the mantle [*Christensen and Fountain*, 1975; *Crawford et al.*, 1987; *Armstrong*, 1988]. Generating large amounts of andesitic crust from a mafic protolith requires the production of a complementary ultramafic, but not peridotitic, residue. This residue is enriched in pyroxene and/or garnet and is petrologically part of the crust.

The fate of this residue raises key questions about crustal evolution. It may reside hidden beneath the geophysical Moho and above the petrological Moho [*Herzberg et al.*, 1983; *Kay and Kay*, 1991; *Kay and Mahlburg Kay*, 1993;], or it may have delaminated to sink into the mantle due to its relative density [*Herzberg et al.*, 1983; *Kay and Kay*, 1993; *Ducea and Saleeby*, 1998]. Delamination may occur during collapse of the arc or after subduction stops [*Herzberg et al.*, 1983; *Kay and Kay*, 1993].

To investigate continental arc processes, the multidisciplinary Batholiths project studied the Coast Plutonic Complex (CPC), also called the Coast Mountains Batholith, of western Canada (Figure 2.1). The Jurassic to Eocene CPC is the world's largest Phanerozoic batholith complex [*Monger et al.*, 1982; *Armstrong*, 1988; *Gehrels et al.*, 2009; *Mahoney et al.*, 2009; *Cecil et al.*, 2011]. It represents Jurassic to Eocene subduction-zone magmatism that intruded and modified terranes accreted earlier in the Mesozoic. The CPC ended with a large pulse of

magmatism in the Eocene, then subduction ceased and the arc underwent extensional collapse [*Monger et al.*, 1982; *Coney and Harms*, 1984]. It is now exposed at mid-crustal level in deep river valleys and fjords [*Andronicos et al.*, 1999]. The Batholiths project investigated the CPC using petrologic, geochronologic, structural, and seismic methods [*Hollister and Andronicos*, 2006; *Chang and Andronicos*, 2009; *Gehrels et al.*, 2009; *Calkins et al.*, 2010; *Wolf et al.*, 2010; *Cecil et al.*, 2011; *Depine et al.*, 2011; *Girardi et al.*, 2012].

As part of Batholiths, a 400-km long east to west seismic refraction and wide-angle reflection profile was acquired in 2009 across the CPC and adjacent Stikine terrane (Figure 2.1). This paper uses travel time inversion of direct, turning, reflected and refracted P-waves to derive a seismic velocity model of the crust and upper-most mantle. This model is interpreted in terms of regional tectonics and magmatic processes, with emphasis on interesting features that were observed in the lower crust and at the Moho.

2.3 Tectonic and Geologic Setting

The interaction of oceanic plates of the Pacific basin with the leading edge of North America is the main driving force of the formation of the northeast Pacific geology and tectonics. Major deformation events and the construction of Cordilleran batholiths along the length of the North American plate margin were driven by collision and subduction processes [*Monger et al.*, 1982]. Recent refinements of this model, particularly relating to the southern Coast Mountains, suggest that the tectonic development was more complex than this general statement indicates (Monger and Brown, in press). Two aspects may be relevant for this study. First, evidence from

northern and central British Columbia indicates that all terranes were accreted to the western margin of North America by the Early to Middle Jurassic (>170 Ma) [van der Heyden, 1992; McClelland et al., 1992; Gehrels, 2001]. A subduction zone and convergence west of the accreted terranes followed, but from about Middle Jurassic to Early Cretaceous (170-105 Ma), this convergence was oblique and southeasterly directed, rather than orogen normal as generally assumed, leading to sinistral faulting. During the Middle Cretaceous (105-85 Ma), the direction of convergence shifted by almost 90 degrees to northeasterly directed, resulting in north-northwest directed dextral faulting that is commonly observed today. Second, associated with the southeasterly directed convergence, a south-southwest directed sinistral fault transected a Middle and Late Jurassic arc along the western margin [Monger et al., 1994; Umhoefer et al., 2002] and moved the northern part of the arc southward, relative to its counterpart in the east, during Middle Jurassic through Early Cretaceous time. However, much of this tectonic development occurred mainly to the south of the locus of the Batholiths profile [*Bustin et al.*, 2013].

Two main tectonic belts are identified in the study area. To the east of the CPC lies, the interior Intermontane Belt superterrane which is composed of the Paleozoic-Mesozoic Stikinia accreted island-arc terrane. Stikinia is covered by early-mid Jurassic Nechako basin sediments and younger volcanic rocks [*Hickson*, 1990]. To the west of the CPC, the outboard Insular Belt superterrane is mainly composed of Paleozoic-Jurassic Wrangellia and Alexander accreted oceanic-arc terranes. The Mesozoic batholiths of the CPC obscure the boundary between the Intermontaine and the Insular superterranes. The CPC itself, is cut by the steeply east-dipping, 800-km long Coast Shear Zone (CSZ) [*Crawford et al.*, 1987; *Gabrielse*, 1991; *Hollister and*

Andronicos, 2006] (Figure 2.1).The CSZ experienced intense ductile dextral and sinistral shear deformation and juxtaposed batholith complexes of different origin [*Crawford et al.*, 1987; *Rusmore et al.*, 2005; *Rusmore et al.*, 2010].

The CPC is composed of granodiorite to granite with an average composition of tonalite [*Hollister and Andronicos*, 2000]. The age of batholiths west of the CSZ decreases systematically from west to east, with pulses of magmatism at ~150, ~120, and 120-80 Ma [*Armstrong*, 1988; *Gehrels et al.*, 2009]. East of the CSZ, magmatism occurred at ~120 Ma with no systematic age progression. Late Cretaceous to early Eocene magmatism is not voluminous along the transect, but is voluminous to the north and south. [*Armstrong*, 1988; *Gehrels et al.*, 2009; *Cecil et al.*, 2011]. Upper amphibolite to granulite facies metamorphism occurred within the CPC between late Cretaceous and Tertiary [*Hollister*, 1975; *Andronicos et al.*, 1999; *Hollister and Andronicos*, 2000; *Andronicos et al.*, 2003]. The spatial distribution of granulite in outcrop indicates that middle crustal plutons provided the heat for the highest degree of the metamorphism

A change from dextral transpression to extension and exhumation occurred in the Eocene [*Coney and Harms*, 1984; *Andronicos et al.*, 2003; *Depine et al.*, 2011]. Late-stage plutons and the CSZ played active roles in extensional collapse of the arc.

2.4 Seismic Refraction and Wide-Angle Reflection Data

In 2009, as part of the multidisciplinary Batholiths project, a 400-km long controlled-source seismic survey was acquired in an east-west line across the CPC and Stikine terrane

(Figure 2.1). Sixteen explosive shots were detonated in 50-m deep boreholes at an average spacing of 29 km. Shot size was targeted to be 1000 kg, but permitting considerations restricted most of the shots to be smaller (Table 1). Shots in Stikinia were larger than 510 kg, while in the CPC all but two shots were less than 388 kg and there were larger gaps between shots. All of the shots were recorded on 1811 vertical-component seismometers deployed at a 200-m spacing onshore and 500-m spacing along fjord shorelines (Figure 2.1). Three-component seismometers were deployed at a 2 km spacing. A short line segment that recorded the large shots and two additional shots were deployed offline to constrain structure along strike (Figure 2.1), but these are not considered in the present analysis.

The seismic turning wave in the upper crust (Pg) is easily observed in the shot gathers (Figures 2.2 , 2.3and 2.4). East of shot 27 in Stikinia, the Pg signal is visible to greater than ~170 km offset from the shot. Smaller shot sizes, larger station spacing, and river and ocean noise affect signal quality in the western half of the line, where signal deteriorates beyond ~130 km offset. The refracted phase from the upper-most mantle (Pn), with an apparent velocity of ~8 km/s, is observed at more than ~150 km offset in eleven shot gathers (Figures 2.2 2.3 and 2.4). Large-amplitude secondary arrivals are interpreted to be reflections from the Moho (PmP). S-wave arrivals turning in the upper crust (Sg) are clearly observed later in the data but these are not considered in this analysis (Figures 2.2 2.3 and 2.4).

Secondary arrivals can be observed earlier than the Moho reflection in some of the shots, and these are interpreted to be mid-crustal reflections. Four shots show mid-crustal reflections, which are here named PiP1, with midpoints under the Stikine terrane (Figure 2.2). No

refractions are observed corresponding to this reflector. A very strong reflection, which is named PiP2, is observed on five shots gathers (Figure 2.3). Midpoints for PiP2 extend from the CSZ to the eastern boundary of the CPC, under the younger portion of the arc. A refraction event with an apparent velocity of ~7 km/s, labeled P7, corresponds to the PiP2 reflector in shots 20 and 22 (Figure 2.3).

Travel times for all P-wave phases were picked manually (Table 1). Pg travel-time picking errors are less than half the dominant period (<40 ms). Pn and secondary arrivals are subject to larger picking errors due to smaller signal strength and/or noise from earlier arrivals. Picking error is about 1 period (~80 ms) for PmP, and larger than about two periods (~160 ms) for the middle crustal reflections (PiP1 and PiP2). The slope of the weak P7 phase is well determined, but the picks may be delayed by up 300 ms from the emergent first arrival.

2.5 Data Analysis

2.5.1 Travel Time Computation

In order to properly consider the effects of the spherical Earth while using Cartesian modeling software, the curved Earth was embedded into a 3-dimensional (3-D) Cartesian grid. The grid was centered at shotpoint 27 at 52.4˚N, -125.603˚W, set to X = 190.95 km, Y = 0.02 km. The X axis is oriented at an azimuth of 85˚ (roughly east), and the Z axis points downward, with Z = 0 at sea level beneath shotpoint 27. With the curved Earth, sea level at the ends of the line is at (X = -2 km, Z = 3.2 km) on the west and (X = 396 km, Z = 2.95 km) on the east (Figure 2.1b).

In order to include the crooked line, upper mantle, and a buffer above the land surface, the model extends 405 km in the X direction, 37 km in Y, and from -5 to 50 km in Z.

Travel times were computed using a 3-D finite difference solution of the Eikonal equation [*Vidale*, 1990; *Hole and Zelt*, 1995], which computes first arrival travel times to all nodes in a gridded velocity model. The travel time at a receiver is computed by interpolation between grid nodes. Ray paths are calculated by following the gradient of the travel time field from the receiver back to the shot point [*Hole*, 1992]. Hole and Zelt [1995] extended the algorithm to calculate reflection travel times from a 3-D reflecting boundary. Times are first computed from the source to the reflector, then times at the reflector are used as a source to compute up-going reflected travel times. Travel times were computed in a 3-D model to account for true distance between shot and receiver on the crooked line. A grid sampling of 1 km was used for a travel-time accuracy that is better than the picking errors.

2.5.2 Layer Stripping

As is typical for this type of seismic data, signal strength is strongest and thus travel-time errors are lowest for the Pg phase that turns in the upper crust. Secondary phases with later arrival times and/or arrivals at long shot-receiver offsets are subject to larger picking errors during modeling. Thus we adopt a layer-stripping philosophy (Figure 2.5) [*Parsons et al.*, 1996; *Zelt et al.*, 1996]. First, a seismic velocity model of the upper crust was derived from travel time tomography of the Pg arrivals. A 2-D non geophysical and geological surface was derived from the resulting Pg ray coverage, under which the ray cover of Pg is very sparse and structure above this surface was kept fixed during modeling of deeper structure. Next, reflection travel times

from the shallowest reflector (PiP1, PiP2, or PmP, depending on location along the line) were used to derive a simple 1-D velocity structure in the middle crust above the reflector, and to invert for depth of the reflector. Structure above these reflectors was then held fixed, and PmP travel times were inverted to obtain velocity of the lower crust and depth to Moho. Finally, the velocity structure of the crust and the Moho depth were held fixed, and Pn arrivals were used to invert for seismic velocity in the uppermost mantle.

Due to the crooked line geometry, all travel-time computations were performed in 3 dimensions using the true shot and receiver geometries. However, the roughly linear geometry does not provide sufficient 3-D coverage to constrain 3-D velocity structure. Therefore, the velocity model at all depths was forced to be 2-D, with velocity smoothed to constant in the Y direction, perpendicular to the line.

2.5.3 Inversion of First Arrival Travel Times For Upper Crustal Velocity

Sixteen shots and a total of 17712 Pg first-arrival travel-time picks (Table 1) were inverted for the upper crustal velocity model using the tomography algorithm Hole [1992] . An average travel time vs. offset curve (Figure 2.6) was used to derive a smooth 1-D velocity model (Figure 2.7) that was used as the starting model for tomography. The 1-D velocity was draped onto the curved Earth to build the 3-D velocity model.

Smoothing with a horizontal to vertical ratio of about 4:1 was applied to the change in velocity during each iteration of the tomography. Large smoothing was used during early iterations and gradually reduced. This process reduces the effect of the starting model and pushes the result towards a model with minimum structure [*Zelt*, 1999]. Initial smoothing size was 400

km horizontally by 80 km vertically, and the final smoothing size was 12 x 3 km. Smaller smoothing resulted in streaking along the ray paths, defining a resolution limit caused primarily by the shot spacing. Smaller smoothing only modestly improved the root-mean-square travel-time misfit. A range of smooth 1-D starting velocity models, including constant velocity and linear gradient, as well as a variety of smoothing aspect ratios, from 8:1 to 1:1, were also tested. Most tests converged to solutions similar to the preferred model.

The final model display good Pg ray coverage to depths of 12-15 km below sea level (Figure 2.8a), and laterally varying upper crustal velocities ranging from 3.2 km/s to 6.3 km/s (Figure 2.9). Based upon the tests with different parameters and the final smoothing size, the spatial resolution of the velocity model is ~10 km horizontally and 2-3 km vertically.

2.5.4 Inversion of Reflection Travel Times for Middle and Lower Crust and Moho

To invert for the depth to interfaces below the Pg ray coverage, a model boundary was created at 10-12 km depth. Velocity above this boundary was fixed to match the results from the Pg tomography. Below this boundary, the middle crustal velocity must be sufficiently slow that it does not result in earlier first arrivals, so velocity was smoothly extrapolated in 1-D with a small increase with depth. Then, travel times from deeper-traveling phases were used to analysis deeper structure (Figure 2.5).

Based on where reflections were observed in the data, the line was split into three segments for the modeling of deeper structure. These include an eastern Stikine terrane segment (model X = 190-400 km), a central segment corresponding to the younger CPC east of the CSZ (X = 90-190 km), and a western CPC segment (X = 0-90 km). Velocity structure below Pg ray

coverage was assumed to be 1-D within each segment, but topography was modeled on the reflecting boundaries between layers.

Through a mixed forward modeling and inversion process, travel times from the shallowest reflection were used to obtain both average velocity above the reflector and reflector topography within each segment (Figure 2.5). Travel times were computed through the 2-D tomography result in the upper crust merged with a smooth 1-D velocity structure in the middle crust. Several 1-D mid-crustal velocity models were tested, each of which increased smoothly with depth but at different rates. For each of these velocity models the inversion algorithm of [*Zelt et al.*, 1996] was used only to derive depth to the reflector as a function of distance along the line. A preferred velocity model was chosen basis of whether a) it produced first arrival times consistent with observed Pg, b) it matched the reflection travel times well, especially as a function of distance, and c) reflector structure that was as smooth as possible (Figure 2.8).

The depth to the reflector that produced the PiP1 reflection beneath the Stikine segment was modeled on the basis of 452 picks from 4 shots (Table 1), Since there was no evidence of a refracted arrival from the PiP1 reflector in the data, it was modeled as a "floating" reflector [*Zelt*, 1999]. It is common for crustal reflections to be produced by thin (hundreds of meters) low or high velocity zones, in the absence of a significant overall velocity increase. The PiP1 reflection is absent in the western third of the Stikine segment. Lacking evidence for lateral velocity variations in the middle and lower crust the 1-D velocity derived from PiP1 was extended across the western portion of the Stikine segment (Figure 2.8).

The PmP reflector was modeled in a similar fashion to that used for PiP1 to obtain the

velocity of the lower crust and the Moho topography. The velocity above the PiP1 reflector and the reflector depth were held fixed, and PmP travel times were inverted for Moho depth using several smooth 1-D models of the lower crust, and a simplest model was chosen (Figure 2.8).

In the western CPC segment of the line, no crustal reflectors were observed, so PmP travel times were used to derive velocity structure of the middle and lower crust as well as the Moho topography (Figure 2.8).

In the eastern, CPC segment, the PiP2 phase was used to derive mid-crustal in a procedure similar to that used for PiP1 in the Stikine segment (Figure 2.8). The PiP2 phase was modeled on the basis of 639 arrivals from 5 shots (Table 1) that were used to determine mid-crustal velocity and depth to the reflector.

In this case, an additional refracted phase, P7, was observed on Shots 20 and 22 (Table 1), providing evidence for a sharp velocity discontinuity associated with the PiP2 reflector. Based upon the depth, length, and position of the reflector, a refraction should have been observed on shots to the west of the CSZ. Unfortunately, these shots were small (163 kg; Table 1) and the seismic signal did not carry to sufficiently long offsets to record the refraction. Nevertheless, the velocity immediately below the interface was directly constrained from the observed refraction travel times by fixing the velocity and structure of the PiP2 reflector as derived from the PiP2 travel times, the velocity immediately below the interface was directly constrained from the observed 7.0 km/s refraction travel times.

PmP moveout was then used to independently confirm the lower crustal velocity below the P7 refractor and to derive Moho topography (Figure 2.8). PmP travel time moveout as a

function of distance constrains the average velocity of the crust (Figure 2.10), and requires high (7.0-7.1 km/s) average velocity below the PiP2 – P7 reflector-refractor. Testing of different 1-D velocity models indicates that the average layer velocity is accurate to about 0.1 km/s. The depths to the deep crustal reflectors and Moho are accurate to about 2 km, caused by picking errors and accuracy of the overlying velocity. Lateral resolution of reflector depth is constrained by the shot spacing and horizontal smoothing to be ~20 km on the crustal reflectors and ~40 km on the Moho.

2.5.5 Inversion of the Moho Refraction Pn

Although the Moho was derived independently under the three segments of the line, the results of 8095 picks on 12 shots produced a consistent, smooth depth profile along the line. The upper mantle velocity then was modeled using the observed refraction event (Pn) The crustal velocity and Moho depth were fixed during this inversion, and Pn travel times were inverted only for uppermost mantle velocity. The starting velocity model had a low velocity gradient from 8.0 to 8.1 km/s below the Moho. A total of 2580 picks (Table 1) from 10 shots were applied to inversion. Lateral resolution of the upper mantle velocity is ~80 km.

2.6 Results

The layer-stripping approach produced a seismic velocity model of the entire crust and upper-most mantle (Figures 2.9 and 2.11). In the shallow upper crust, velocities <5km/s extends to depths of up to 5 km. The vertical resolution at the surface is ~2 km due to smoothing applied

during Pg tomography, and therefore the lowest-velocity bodies are smoothed images of thin sediment or sedimentary rock layers. Details in the shallow velocity model under the CPC may be caused by the large gaps between shots and the sparser and noisier seismograph sites along fjords and rivers. Throughout the model, velocity increases rapidly to ~6 km/s at 5-8 km depth, then increases gradually to ~6.3 km/s at 15-20 km depth where the PiP1 and PiP2 reflectors occur (Figures 2.9 and 2.11).

The PiP1 reflector under Stikinia dips modestly westward at 20-22 km depth (Figure 2.11). The variable shot spacing produces discontinuous coverage on this reflector (Figure 2.8), but since the reflections have similar strength and moveout in the shot gathers and occur at similar depth, they are interpreted to be the same reflector. . The lower crust under Stikinia beneath this reflector has an average velocity of 6.7 km/s.

The PiP2 reflector extends from the CSZ to the eastern margin of the CPC at ~27 km depth (Figures 2.8 and 2.11). The P7 refraction and the PmP each independently constrain velocity in the lower crust beneath this reflector to be 7.0-7.1 km/s (Figures 2.9 and 2.11). West of the CSZ, there is no evidence for a middle or lower crustal reflector or refractor. PmP travel times constrain the lower crust west of the CSZ to have an average velocity <6.6 km/s (Figures 2.9 and 2.11), much slower than on the other side of the CSZ.

The Moho is nearly flat beneath Stikinia at ~35 km depth. It deepens to ~37 km depth beneath the highest topography of the eastern CPC (Figure 2.11). West of the CSZ, the Moho rises to ~30 km depth near the coast. The upper mantle velocity is 8.0 km/s under the CPC which is slightly slower than the upper mantle velocity of 8.1 km/s below Stikinia (Figure 2.9).

2.7 Discussion

2.7.1 Stikinia

Stephenson et al. [2011] previously interpreted the Batholiths seismic data for structure in the Stikinia portion of the line. Velocities of <5 km/s at ~5 km depth (Figure 2.11) are interpreted to represent the sedimentary Nechako Basin and thin overlying volcanic rocks. The data image two deeper sub-basins at model distances 250-275 km and 320-370 km, consistent with Stephenson et al. [2011]. Figure 2.11 has lower resolution of the basin than the model of Stephenson et al. [2011] because it used larger smoothing to maintain stability at larger scale.

Beneath the Nechako Basin, at 5-20 km depth, the velocity increases rapidly to ~ 6 km/s, then gradually increases to ~6.3 km/s (Figures 2.9 and 2.11). These values are indicative of a felsic crystalline lithology and are consistent with other seismic studies in Stikinia [*Hammer and Clowes*, 2004; *Clowes et al.*, 2005]. These velocities are interpreted to represent arc volcanic basement rocks of the Intermontane Belt Stikine and Cache Creek terranes. In the lower crust, the velocity of ~6.7 km/s is consistent with an amphibolite or hydrated mafic composition *[Christensen and Mooney, 1995]*, as proposed by Hollister and Andronicos [2006]. The Moho beneath Stikinia is relatively flat at around ~35 km. The underlying mantle has a slightly fast velocity of 8.1 km/s, perhaps due to an evolved lithospheric lid.

2.7.2 Coast Plutonic Complex West of the Coast Shear Zone

In the Jurassic to mid-Cretaceous CPC west of the CSZ, the velocity quickly increases with depth from ~5 km/s to <6.3 km/s (Figure 2.11), consistent with the felsic plutonic rocks

exposed at the surface. As constrained by reflections from the Moho, the average velocity of the entire crust is sufficiently slow that velocity in the lower crust is <6.6 km/s. This velocity is consistent with the lower crust being of similar felsic-intermediate bulk composition as the upper crust [*Christensen and Fountain,* 1975]. Rocks of the Wrangellia terrane and perhaps the Alexander terrane are exposed along this portion of the line. However, the observed velocity in the lower crust is much slower than the 6.8-6.9 km/s observed under Wrangellia ~80 km to the west [*Yuan et al.,* 1992]. The lower crustal velocity of the CPC west of the CSZ is also slower than that observed along strike in the CPC ~250 km to the northwest (6.6-6.7 km/s) [*Hammer and Clowes,* 2004; *Clowes et al.,* 2005] and ~150 km southeast (6.7 km/s) [*Zelt et al.,* 1996; *Spence and Mclean,* 1998]. The lower velocity is interpreted to indicate that the accreted terranes at this latitude were nearly completely replaced by arc batholiths, and any residual materials were delaminated, perhaps during arc collapse, or lie beneath the geophysical Moho.

The thickness of the crust decreases westward from ~37 km at the CSZ to 30 km-33km near the coast. Immediately offshore, Miocene extension thinned the crust and created the Queen Charlotte Basin. The observed westward thinning is consistent with crustal thickness of <33 km observed by Yuan et al. [1992] offshore.

2.7.3 Younger Coast Plutonic Complex East of the Coast Shear Zone

In the CPC east of the CSZ, low velocity of <5 km/s exists near the surface (Figure 2.11). It coincides with the Bella Coola Valley and is interpreted to be due to alluvial sediment. The low velocity is stretched vertically by the spatial resolution of the smoothed tomography, and helps to visualize resolution in the near surface.

Velocity rapidly rises to ~6 km/s, and then rises very slowly through the middle crust (Figures 2.9 and 2.11). The velocity is similar to both the CPC to the west and Stikinia to the east, consistent with felsic plutons and perhaps Stikine country rocks extending to >25 km depth.

A strong seismic reflector is observed at ~27 km depth beneath the eastern CPC (Figure 2.11). The extent of the reflector is constrained by the presence or absence of wide-angle reflections observed in several shots (Figure 2.8). The east end of the reflector underlies the eastern margin of the CPC. The west end of the reflector is not as well constrained due to smaller shot sizes (Table 1), but lies a short distance east of the CSZ. Below this reflector, a high velocity of 7.0-7.1 km/s extends to the Moho (Figures 2.9 and 2.11). This high velocity is independently constrained by both a refracted arrival and the difference in reflection moveout from the top and bottom of the layer. The lateral extent of the reflector is shorter than that required by the refraction event. However, after considering gaps in coverage due to small shots and gaps between shots, the data allow the reflector to extend as far as the refractor is shown in Figure 2.11. This may indicate that the CSZ extends into the lower crust with a near-vertical orientation [*Andronicos et al.*, 1999; *Hollister and Andronicos*, 2006]. The high-velocity layer in the lower crust is much faster than under Stikinia to the east or under the older CPC west of the CSZ. It is inconsistent with velocity observed in other studies for Stikinia [*Clowes et al.*, 2005] or for Wrangellia [*Yuan et al.*, 1992]. This unique layer occurs only within the younger Cretaceous to Eocene arc to the east of the CSZ, and must be associated with magmatic processes of the younger arc. Similar high velocities are not observed in the CPC ~250 km along strike to the northwest [*Hammer and Clowes*, 2004; *Clowes et al.*, 2005] or ~150 km to the

southeast [*Zelt et al.*, 1996; *Spence and Mclean*, 1998], not even within the Eocene portion of the arc.

A velocity of 7.0-7.1 km/s at this depth is consistent with either dry gabbro or mafic garnet granulite [*Christensen and Fountain*, 1975; *Christensen and Mooney*, 1995]. While gabbroic melt is produced from the mantle in subduction-zone continental arcs, this setting is water-rich [*Hollister and Andronicos*, 2006], which produces a slower seismic velocity than that observed. The high-velocity layer is instead interpreted to be mafic garnet granulite created by partial melting within the crust. When a hydrous mafic protolith such as amphibolite is partially melted, it produces a melt of granodiorite composition that rises to create batholiths in the upper crust. Left behind is a solid residual of mafic garnet granulite composed of clinopyroxene + orthopyroxene + quartz + plagioclase under >10kbar pressure at >25km depth [*Beard and Lofgren*, 1991; *Douce and Beard*, 1995].

Petrologic models indicate that dehydration melting should produce a residual that is one to two times the volume of the magma. The residue should be mostly in the granulite facies which is gravitationally stable in the lower crust [*Ducea*, 2002]. The seismic velocity model indicates ~27 km of overlying felsic crust, plus 5-10 km of exhumation , which is much thicker than the ~11 km of interpreted residual in the lower crust. Some unknown proportion of the felsic crust might consist of Stikinia protolith, which has a similar seismic velocity, but surface exposure is predominantly batholiths. This suggests that the observed residual is only a small portion of a much larger residual that has been delaminated.

A large magmatic residual has only been detected under one other magmatic arc. A mafic to ultramafic residue is observed as xenoliths in younger, Miocene volcanic rocks that cut through the Mesozoic Sierra Nevada arc batholith complex in California [*Ducea and Saleeby*, 1998]. The residue is garnet rich, pyroxene rich and granulitic, and is interpreted to be extracted from 35 to 40 km depth by two-step magmatic differentation [*Ducea and Saleeby*, 1998; *Ducea*, 2002]. Additionally, a high-velocity anomaly is observed in the upper mantle and interpreted to be actively delaminating ultramafic, pyroxene-rich residual [*Zandt et al.*, 2004]. A west-dipping Moho at 40-45 km depth with higher upper-mantle velocity overlies the ultramafic residue [*Frassetto et al.*, 2011]. The overlying crustal seismic velocity indicates a felsic composition.

Compared to the Sierra Nevada batholith, no seismic velocity anomaly has been observed in the upper mantle beneath the CPC [*Calkins et al.*, 2010]. However, in the CPC east of the CSZ, broadband receiver functions observed complex receiver functions that were not easily modeled by simple geologic models. This is consistent with our interpretation of a mafic, not ultramafic residual in the lower crust.

The crustal thickness is ~37 km beneath the high-velocity lower crust. The Moho is modestly deeper than under Stikinia but is much deeper than west of the CSZ. Crustal thickness mimics topography (Figure 2.1b), and the existence of a modest Moho root under the garnet-granulite lower crust is qualitatively consistent with isostasy. The upper mantle velocity is 8.0 km/s, slightly slower than that under Stikinia. It is also slightly slower than upper mantle velocities of 7.9 km/s for the CPC further north [Hammer and Clowes, 2004; Clowes et al.,

2005] or to the south [Zelt et al., 1996; Spence and Mclean, 1998], although all values are similar within their velocity resolution.

2.8 Conclusions

The lower crust of the Coast Plutonic Complex in the Central Coast of British Columbia has seismic velocities that are inconsistent with the accreted terranes of the region, representative of arc processes. Different structures are observed across the Coast Shear Zone, which separates two arc complexes of different magmatic ages. The older arc to the west of the CSZ has a seismic velocity in the lower crust that indicates a more felsic lithology than the accreted terranes, suggesting that it has been replaced by felsic-intermediate batholiths. In contrast, a high-velocity layer is observed in the lower crust east of the CSZ, where the arc includes a younger pulse of Eocene magmatism. This high-velocity layer is faster than the accreted terranes. It is interpreted to be evidence for a mafic garnet granulite residual that resulted from magmatic fractionation of an amphibole to create felsic arc batholiths and a mafic-ultramafic residual. No residual layer is observed west of the CSZ. There is a minor Moho root beneath the residual layer, and the crust thins rapidly west of the CSZ.

2.9 Acknowledgements

This work was funded by National Science Foundation (NSF) grant numbers EAR-0310126 and EAR-XXXXXX in the USA and by the Natural Sciences and Engineering

Research Council (NSERC) in Canada. We gratefully acknowledge the 67-person field crew, mostly student volunteers from 13 different universities. IRIS-PASSCAL provided the seismic instruments and field support. Several First Nations bands allowed the project on their traditional lands.

2.10 References

Andronicos, C. L., Chardon, D. H., Hollister, L. S., Gehrels, G. E., and Woodsworth, G. J. (2003), Strain partitioning in an obliquely convergent orogen, plutonism, and synorogenic collapse: Coast Mountains Batholith, British Columbia, Canada, *Tectonics*, *22*(2), 1012, doi:10.1029/2001TC001312.

Andronicos, C. L., Hollister, L. S., Davidson, C., and Chardon, D. (1999), Kinematics and tectonic significance of transpressive structures within the Coast Plutonic Complex, British Columbia, *Journal of Structural Geology*, *21*(2), 229-243, doi:http://dx.doi.org/10.1016/S0191-8141(98)00117-5.

Armstrong, R. L. (1988), Mesozoic and early Cenozoic magmatic evolution of the Canadian Cordillera, *Geological Society of America Special Papers*, *218*, 55-92, doi:10.1130/SPE218-p55.

Beard, J. S., and Lofgren, G. E. (1991), Dehydration Melting and Water-Saturated Melting of Basaltic and Andesitic Greenstones and Amphibolites at 1, 3, and 6. 9 kb, *Journal of Petrology*, *32*(2), 365-401.

Bustin, A. M. M., Clowes, R. M., Monger, J. W. H., and Journeay, J. M. (2013), The southern Coast Mountains, British Columbia: New interpretations from geological, seismic reflection, and gravity data, *Canadian Journal of Earth Sciences*, *50*(10), 1033-1050, doi:10.1139/cjes-2012-0122.

Calkins, J. A., Zandt, G., Girardi, J., Dueker, K., Gehrels, G. E., and Ducea, M. N. (2010), Characterization of the crust of the Coast Mountains Batholith, British Columbia, from P

to S converted seismic waves and petrologic modeling, *Earth and Planetary Science Letters*, *289*(1–2), 145-155, doi:http://dx.doi.org/10.1016/j.epsl.2009.10.037.

Cecil, M. R., Gehrels, G., Ducea, M. N., and Patchett, P. J. (2011), U-Pb-Hf characterization of the central Coast Mountains batholith: Implications for petrogenesis and crustal architecture, *Lithosphere*, *3*(4), 247-260, doi:10.1130/l134.1.

Chang, J. M., and Andronicos, C. L. (2009), Constraints on the depth of generation and emplacement of a magmatic epidote-bearing quartz diorite pluton in the Coast Plutonic Complex, British Columbia, *Terra Nova*, *21*(6), 480-488.

Christensen, N. I., and Fountain, D. M. (1975), Constitution of the Lower Continental Crust Based on Experimental Studies of Seismic Velocities in Granulite, *Geological Society of America Bulletin*, *86*(2), 227-236, doi:10.1130/0016-7606(1975)86<227:cotlcc>2.0.co;2.

Christensen, N. I., and Mooney, W. D. (1995), Seismic velocity structure and composition of the continental crust: A global view, *J. Geophys. Res.*, *100*(B6), 9761-9788, doi:10.1029/95JB00259.

Clowes, R. M., Hammer, P. T. C., Fernández-Viejo, G., and Welford, J. K. (2005), Lithospheric structure in northwestern Canada from Lithoprobe seismic refraction and related studies: a synthesis, *Canadian Journal of Earth Sciences*, *42*(6), 1277-1293, doi:10.1139/e04-069.

Coney, P. J., and Harms, T. A. (1984), Cordilleran metamorphic core complexes: Cenozoic extensional relics of Mesozoic compression, *Geology*, *12*(9), 550-554.

Crawford, M. L., Hollister, L. S., and Woodsworth, G. J. (1987), Crustal deformation and regional metamorphism across a terrane boundary, Coast Plutonic Complex, British Columbia, *Tectonics*, *6*(3), 343-361, doi:10.1029/TC006i003p00343.

Depine, G. V., Andronicos, C. L., and Hollister, L. S. (2011), Response of continental magmatic arcs to regional tectonic changes recorded by synorogenic plutons in the middle crust: An example from the Coast Mountains of British Columbia, *Journal of Structural Geology*, *33*(6), 1089-1104, doi:http://dx.doi.org/10.1016/j.jsg.2011.03.012.

Ducea, M. N. (2002), Constraints on the bulk composition and root foundering rates of continental arcs: A California arc perspective, *J. Geophys. Res.*, *107*(B11), 2304, doi:10.1029/2001JB000643.

Ducea, M. N., and Saleeby, J. B. (1998), The age and origin of a thick mafic–ultramafic keel from beneath the Sierra Nevada batholith, *Contr. Mineral. and Petrol.*, *133*(1-2), 169-185, doi:10.1007/s004100050445.

Frassetto, A. M., Zandt, G., Gilbert, H., Owens, T. J., and Jones, C. H. (2011), Structure of the Sierra Nevada from receiver functions and implications for lithospheric foundering, *Geosphere, 7*(4), 898-921, doi:10.1130/ges00570.1.

Gabrielse, H. (1991), Late Paleozoic and Mesozoic terrane interactions in north-central British Columbia, *Canadian Journal of Earth Sciences*, *28*(6), 947-957, doi:10.1139/e91-086.

Gehrels, G., Rusmore, M., Woodsworth, G., Crawford, M., Andronicos, C., Hollister, L., Patchett, J., Ducea, M., Butler, R., Klepeis, K., Davidson, C., Friedman, R., Haggart, J., Mahoney, B., Crawford, W., Pearson, D., and Girardi, J. (2009), U-Th-Pb geochronology

of the Coast Mountains batholith in north-coastal British Columbia: Constraints on age and tectonic evolution, *Geological Society of America Bulletin*, *121*(9-10), 1341-1361, doi:10.1130/b26404.1.

Girardi, J. D., Patchett, P. J., Ducea, M. N., Gehrels, G. E., Cecil, M. R., Rusmore, M. E., Woodsworth, G. J., Pearson, D. M., Manthei, C., and Wetmore, P. (2012), Elemental and Isotopic Evidence for Granitoid Genesis From Deep-Seated Sources in the Coast Mountains Batholith, British Columbia, *Journal of Petrology*, *53*(7), 1505-1536, doi:10.1093/petrology/egs024.

Hammer, P. T. C., and Clowes, R. M. (2004), Accreted terranes of northwestern British Columbia, Canada: Lithospheric velocity structure and tectonics, *J. Geophys. Res.*, *109*(B6), B06305, doi:10.1029/2003JB002749.

Herzberg, C., Fyfe, W., and Carr, M. (1983), Density constraints on the formation of the continental Moho and crust, *Contr. Mineral. and Petrol.*, *84*(1), 1-5.

Hickson, C. (1990), A new Frontier Geoscience Project: Chilcotin-Nechako region, central British Columbia, *Current Research, Part F, Geological Survey of Canada, Paper*, 115-120.

Hole, J. A. (1992), Nonlinear high-resolution three-dimensional seismic travel time tomography, *Journal of Geophysical Research: Solid Earth*, *97*(B5), 6553-6562, doi:10.1029/92JB00235.

Hole, J. A., and Zelt, B. C. (1995), 3-D finite-difference reflection travel times, *Geophysical Journal International*, *121*(2), 427-434, doi:10.1111/j.1365-246X.1995.tb05723.x.

Hollister, L., and Andronicos, C. (2000), The Central Gneiss Complex, Coast Mountains, *British Columbia*.

Hollister, L. S. (1975), Granulite Facies Metamorphism in the Coast Range Crystalline Belt, *Canadian Journal of Earth Sciences*, *12*(11), 1953-1955, doi:10.1139/e75-172.

Hollister, L. S., and Andronicos, C. L. (2006), Formation of new continental crust in Western British Columbia during transpression and transtension, *Earth and Planetary Science Letters*, *249*(1–2), 29-38, doi:http://dx.doi.org/10.1016/j.epsl.2006.06.042.

Kay, R., and Mahlburg-Kay, S. (1991), Creation and destruction of lower continental crust, *Geologische Rundschau*, *80*(2), 259-278.

Kay, R. W., and Mahlburg Kay, S. (1993), Delamination and delamination magmatism, *Tectonophysics*, *219*(1), 177-189.

Mahoney, J. B., Gordee, S. M., Haggart, J. W., Friedman, R. M., Diakow, L. J., and Woodsworth, G. J. (2009), Magmatic evolution of the eastern Coast Plutonic Complex, Bella Coola region, west-central British Columbia, *Geological Society of America Bulletin*, *121*(9-10), 1362-1380, doi:10.1130/b26325.1.

Monger, J.W.H., and Brown, E.H. Tectonic evolution of the southern Coast-Cascade Orogen, northwestern Washington and southwestern British Columbia. Rocks, Fire, and Ice: The Geology of Washington. Edited by E. S. Cheney. University of Washington Press. In press

Monger, J. W. H., Price, R. A., and Tempelman-Kluit, D. J. (1982), Tectonic accretion and the origin of the two major metamorphic and plutonic welts in the Canadian Cordillera, *Geology*, *10*(2), 70-75, doi:10.1130/0091-7613(1982)10<70:taatoo>2.0.co;2.

Parsons, T., Mccarthy, J., Kohler, W. M., Ammon, C. J., Benz, H. M., Hole, J., and Criley, E. E. (1996), Crustal structure of the Colorado Plateau, Arizona: Application of new long-offset seismic data analysis techniques, *Journal of geophysical research*, *101*(B5), 11173-11111,11194.

Rusmore, M. E., Bogue, S. W., Dodson, K., Farley, K. A., and Woodsworth, G. J. (2010), Deformation of continental crust along a transform boundary, Coast Mountains, British Columbia, *Tectonics*, *29*(4), TC4007, doi:10.1029/2009TC002502.

Rusmore, M. E., Woodsworth, G. J., and Gehrels, G. E. (2005), Two-stage exhumation of midcrustal arc rocks, Coast Mountains, British Columbia, *Tectonics*, *24*(5), TC5013, doi:10.1029/2004TC001750.

Spence, G. D., and Mclean, N. A. (1998), Crustal seismic velocity and density structure of the Intermontane and Coast belts, southwestern Cordillera, *Canadian Journal of Earth Sciences*, *35*(12), 1362-1379.

Stephenson, A., Spence, G., Wang, K., Hole, J., Miller, K., Clowes, R., Harder, S., Kaip, G., and Mareschal, J.-C. (2011), Crustal velocity structure of the southern Nechako basin, British Columbia, from wide-angle seismic traveltime inversion 1 1 This article is one of a series of papers published in this Special Issue on the theme of New insights in Cordilleran

Intermontane geoscience: reducing exploration risk in the mountain pine beetle-affected area, British Columbia, *Canadian Journal of Earth Sciences*, *48*(6), 1050-1063.

Vidale, J. E. (1990), Finite-difference calculation of traveltimes in three dimensions, *Geophysics*, *55*(5), 521-526.

Wolf, D. E., Andronicos, C. L., Vervoort, J. D., Mansfield, M. R., and Chardon, D. (2010), Application of Lu–Hf garnet dating to unravel the relationships between deformation, metamorphism and plutonism: An example from the Prince Rupert area, British Columbia, *Tectonophysics*, *485*(1), 62-77.

Yuan, T., Spence, G., and Hyndman, R. (1992), Structure beneath Queen Charlotte Sound from seismic-refraction and gravity interpretations, *Canadian Journal of Earth Sciences*, *29*(7), 1509-1529.

Zandt, G., Hersh, G., Owens, T. J., Mihal, D., and Et Al. (2004), Active foundering of a continental arc root beneath the southern Sierra Nevada in California, *Nature*, *431*(7004), 41-46, doi:10.1038/nature02847.

Zelt, B. C., Ellis, R. M., Clowes, R. M., and Hole, J. A. (1996), Inversion of three-dimensional wide-angle seismic data from the southwestern Canadian Cordillera, *J. Geophys. Res.*, *101*(B4), 8503-8529, doi:10.1029/95JB02807.

Zelt, C. A. (1999), Modelling strategies and model assessment for wide-angle seismic traveltime data, *Geophysical Journal International*, *139*(1), 183.

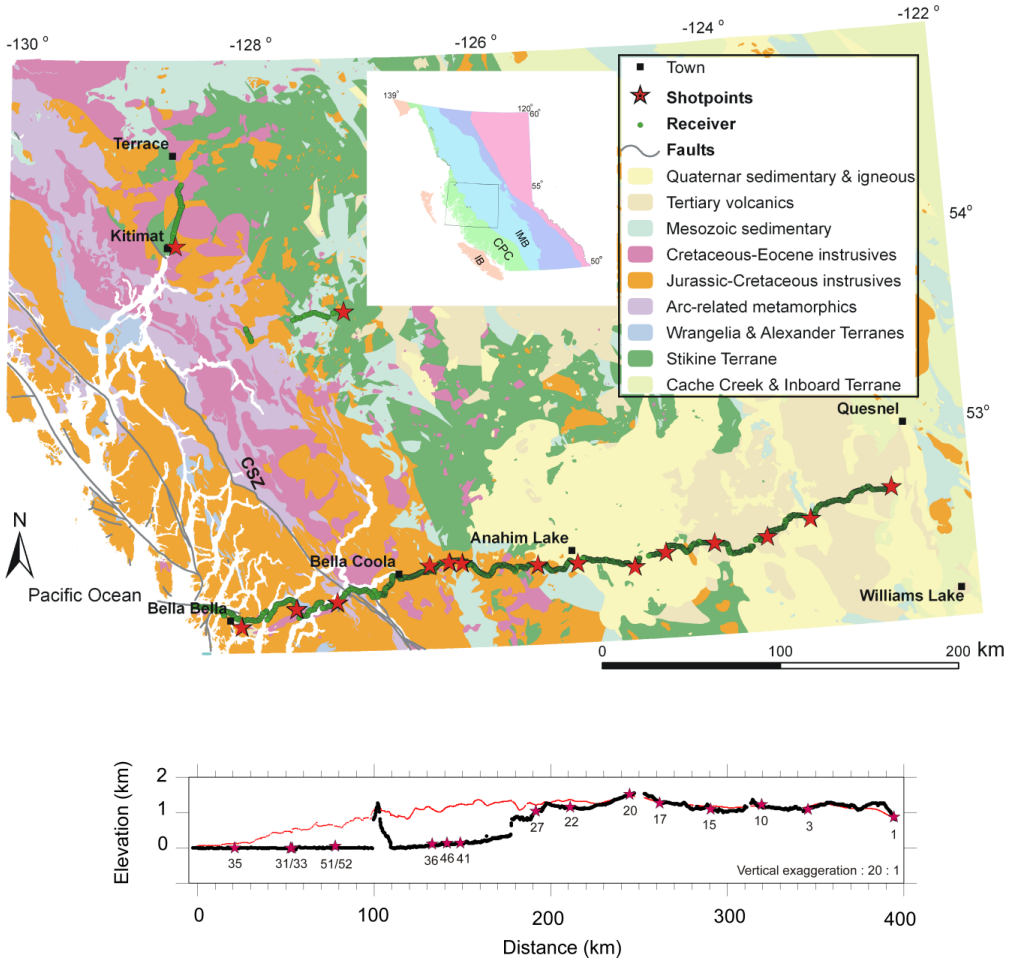

Figure 2.1 Map of the Batholiths wide-angle seismic survey and geology. Stars are seismic shots and green circles are the seismographs. Index map shows geologic provinces of British Columbia, Canada. CPC is Coast Plutonic Complex; IMB, Intermontain Belt superterrane; IB, Insular Belt superterrane. An elevation profile along the seismic line at a vertical exaggeration of 20:1 is shown in the lower panel. The red line is elevation averaged over

a 10x10 km area. Shots and seismographs in the CPC were deployed in deep glacial valleys and fjords.

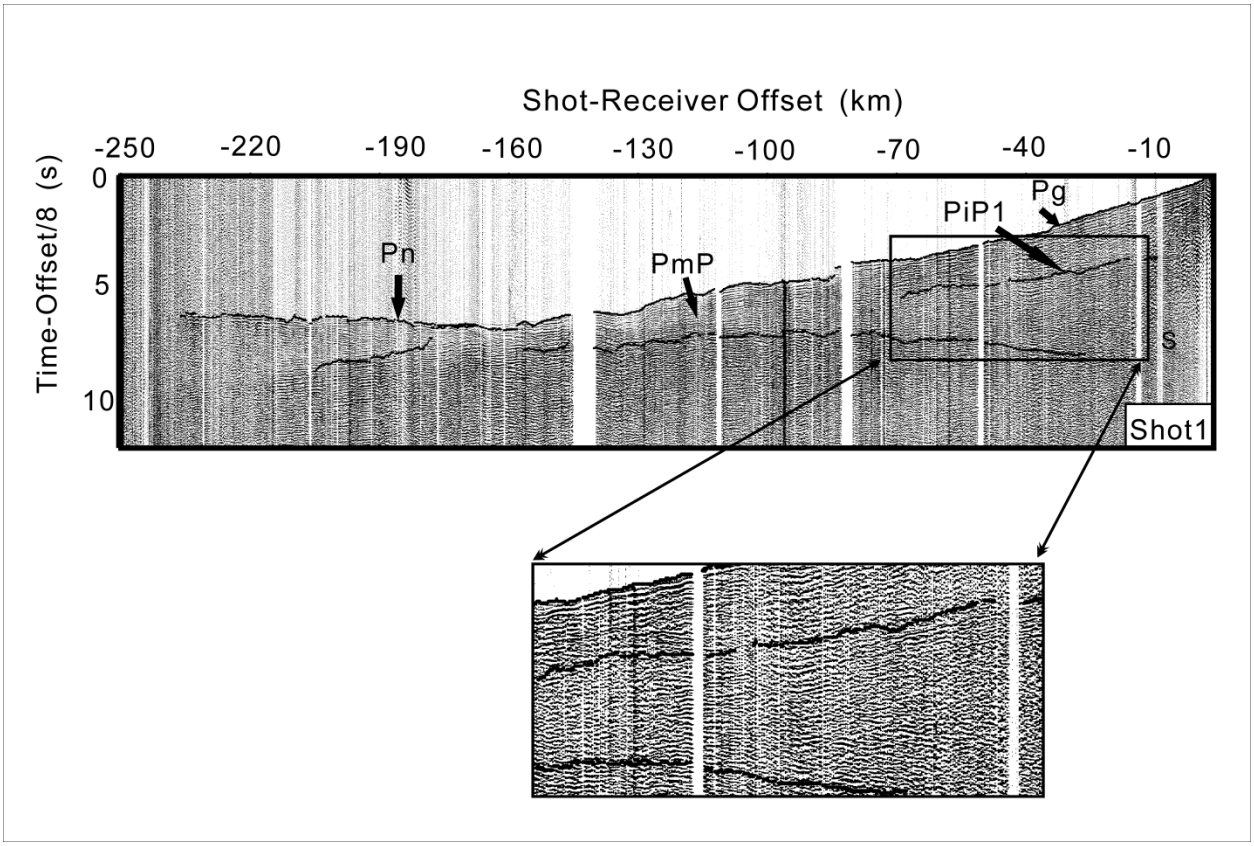

Figure 2.2 Shot 1 seismic gather. Travel-time picks are shown as darker symbols. The time axis is plotted with a reducing velocity of 8.0 km/s. A 2-18 Hz bandpass filter and trace amplitude balancing have been applied. Major seismic arrivals are labeled (see text for description).

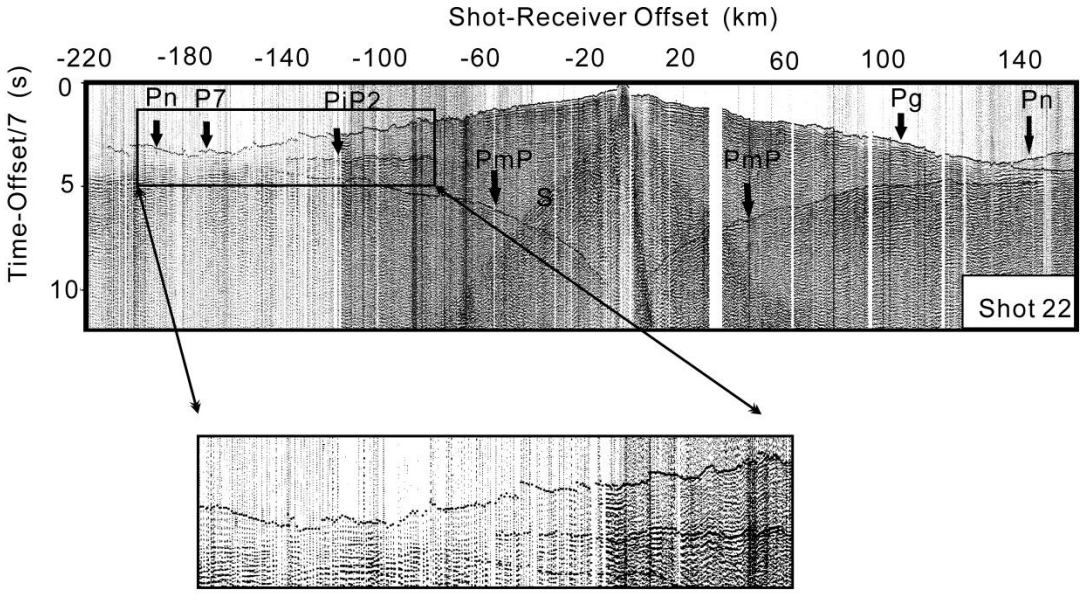

Figure 2.3 shot 22 seismic gather and travel-time picks, plotted as in Figure 2.2 A different reducing velocity of 7 km/s is used to better visualize the P7 arrival.

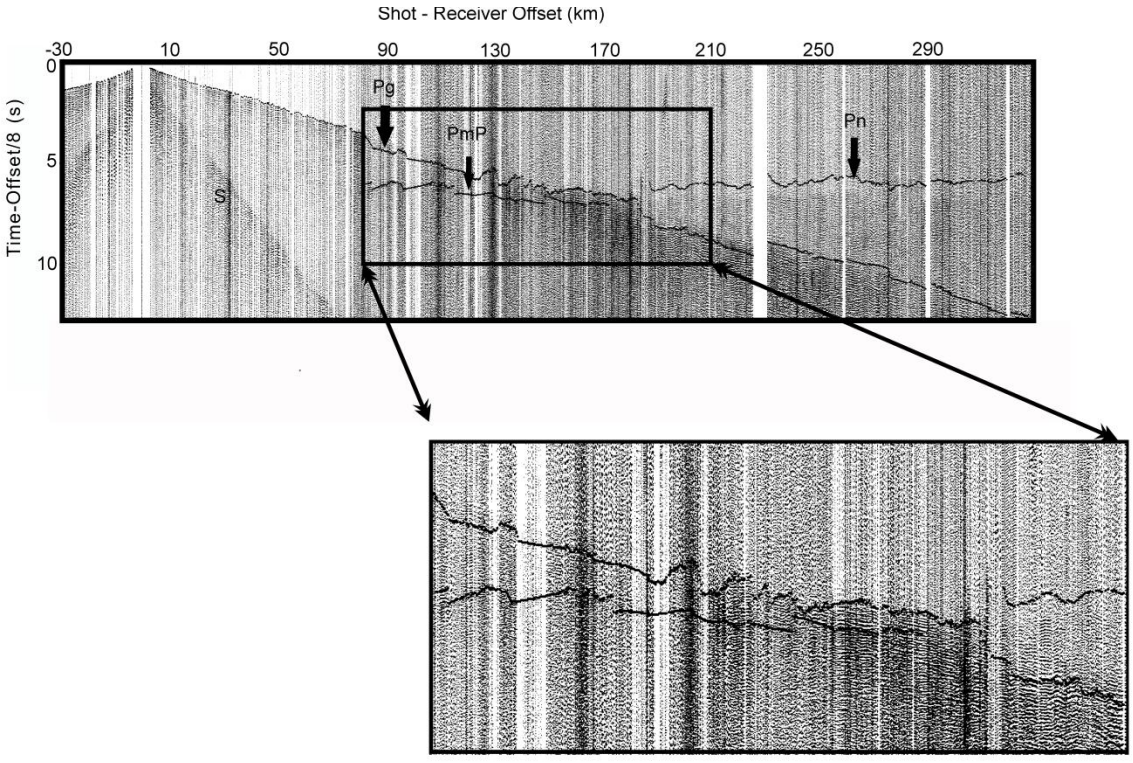

Figure 2.4 shot 35 seismic gather and travel-time picks, plotted as in Figure 2. 2

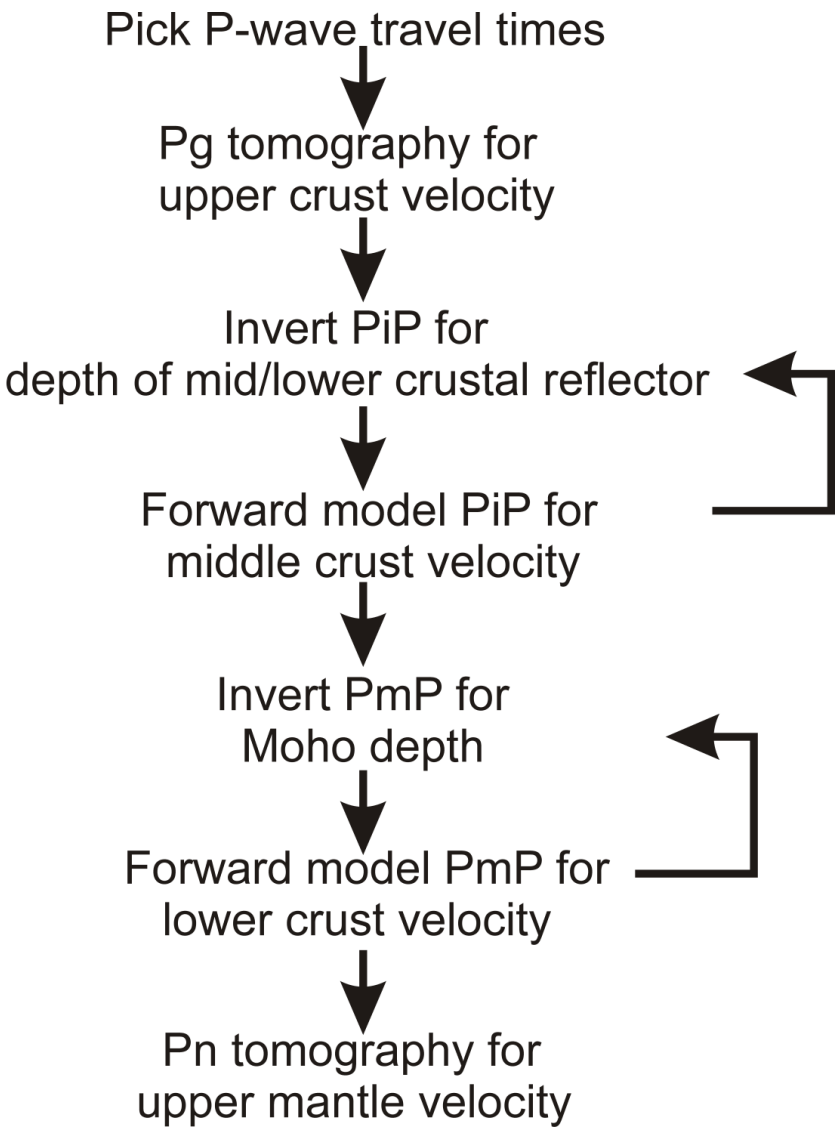

Figure 2.5 Flowchart of the 3-D modeling procedure, modified from [Parsons et al., 1996].

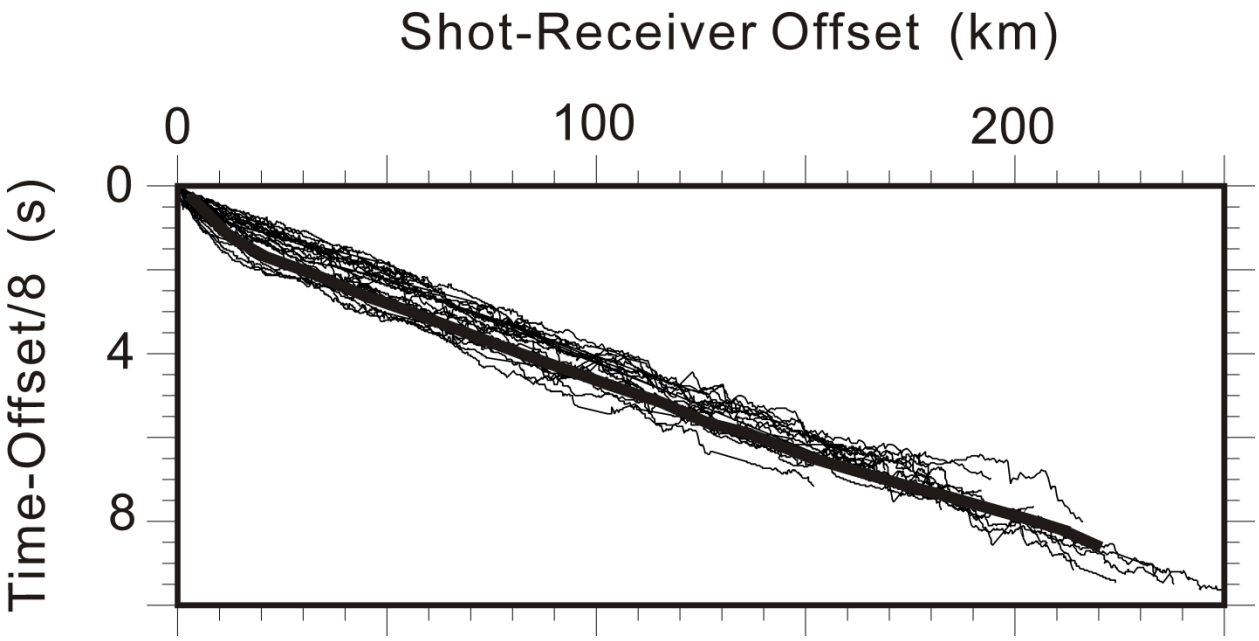

Figure 2.6 First arrival travel-time picks of the turning wave in the upper crust, Pg, plotted with a reducing velocity of 8 km/slines are individual shots; the average is the thick line.

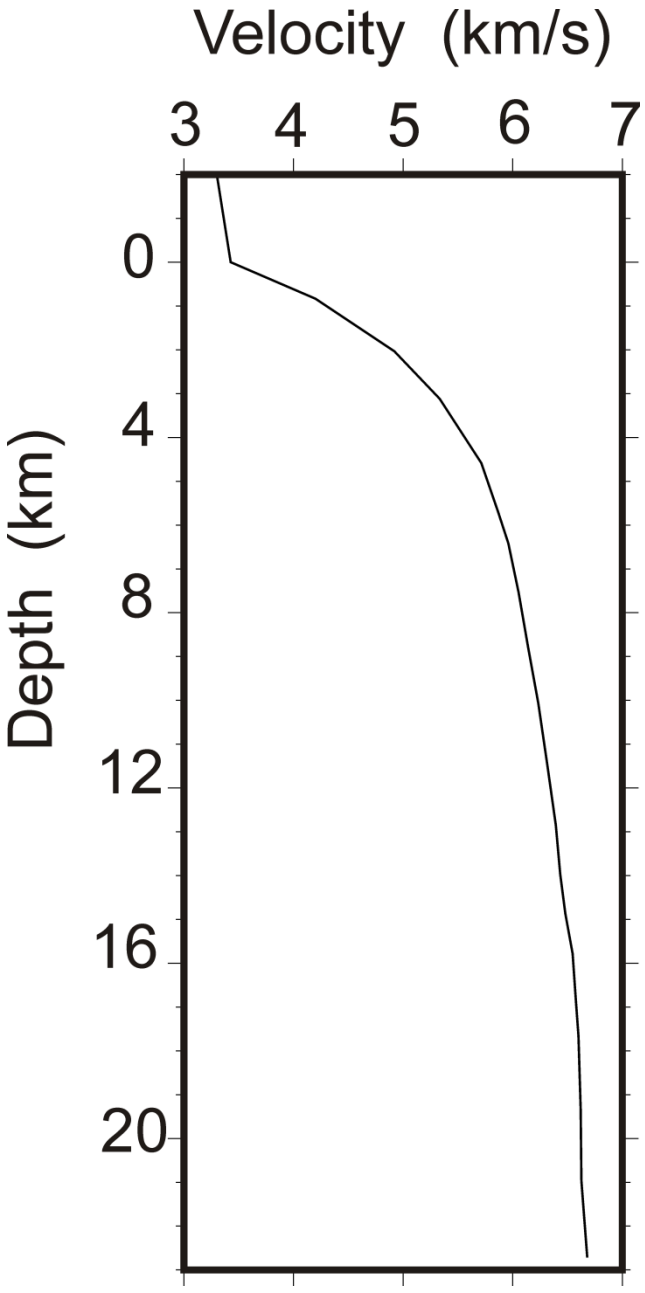

Figure 2.7 1-D starting velocity model derived from the average picks in Figure 2.6.

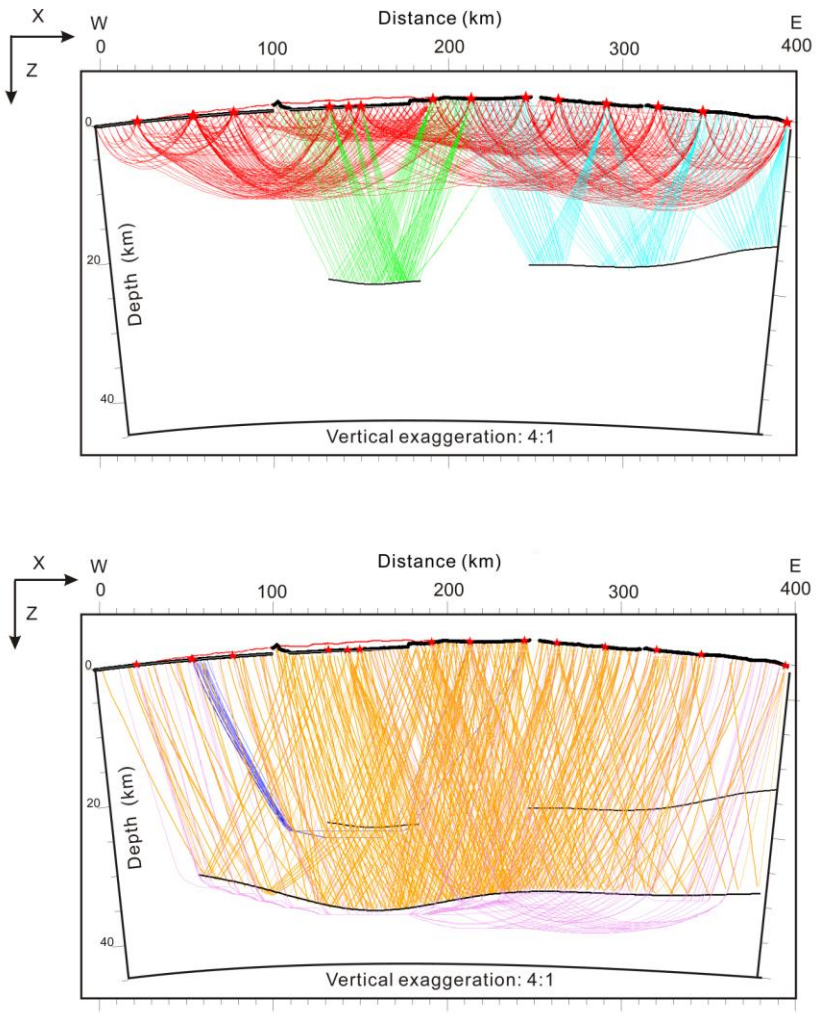

Figure 2.8 Ray cover for the model a). Ray coverage used to derive the seismic velocity model. Rays are traced to seismograph stations at a 5 km spacing; real coverage at 200 m station spacing is not shown for clarity. Pg is in red; PiP1 is cyan; PiP2 is green; P7 refraction is dark blue; b). PmP is orange; Pn is light purple. Thick black lines represent seismic reflectors. The non-parallel depth axes and curved Earth surface represent the spherical Earth. Modeling was

performed within a Cartesian coordinate system represented by the surrounding square box and X-Z directions.

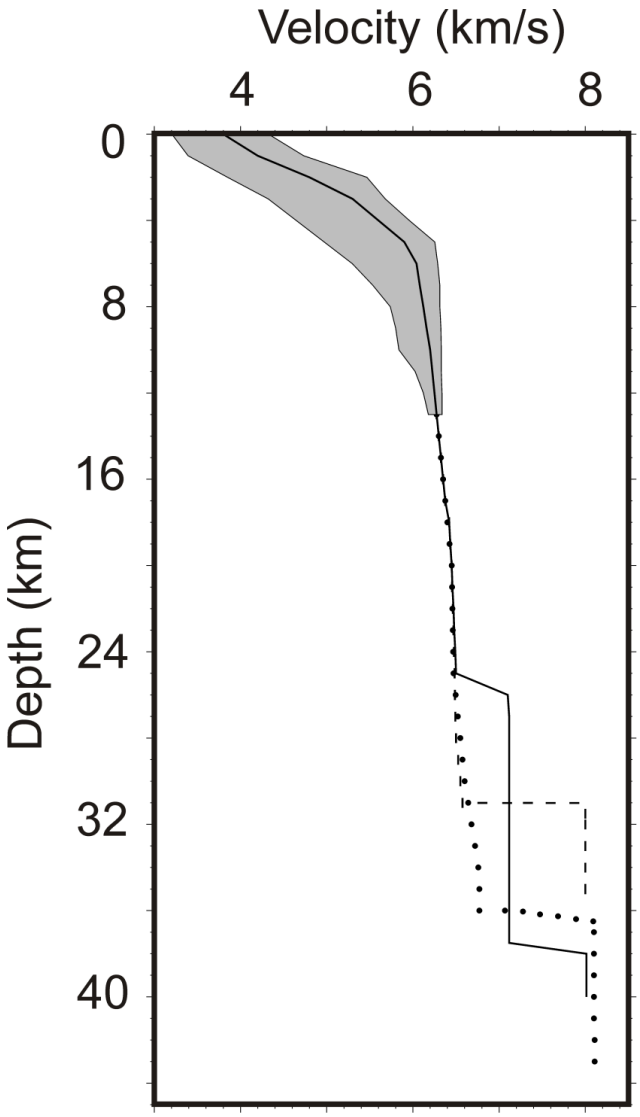

Figure 2.9 Average 1-D velocity model. Grey shading indicates the range of velocity and thick black line the average velocity in the upper crust. Below 13 km depth, the average is shown in each geologic region: solid line, Coast Plutonic Complex (CPC) east of the Coast Shear Zone (CSZ); dashed line CPC west of the CSZ; dotted line, Stikinia.

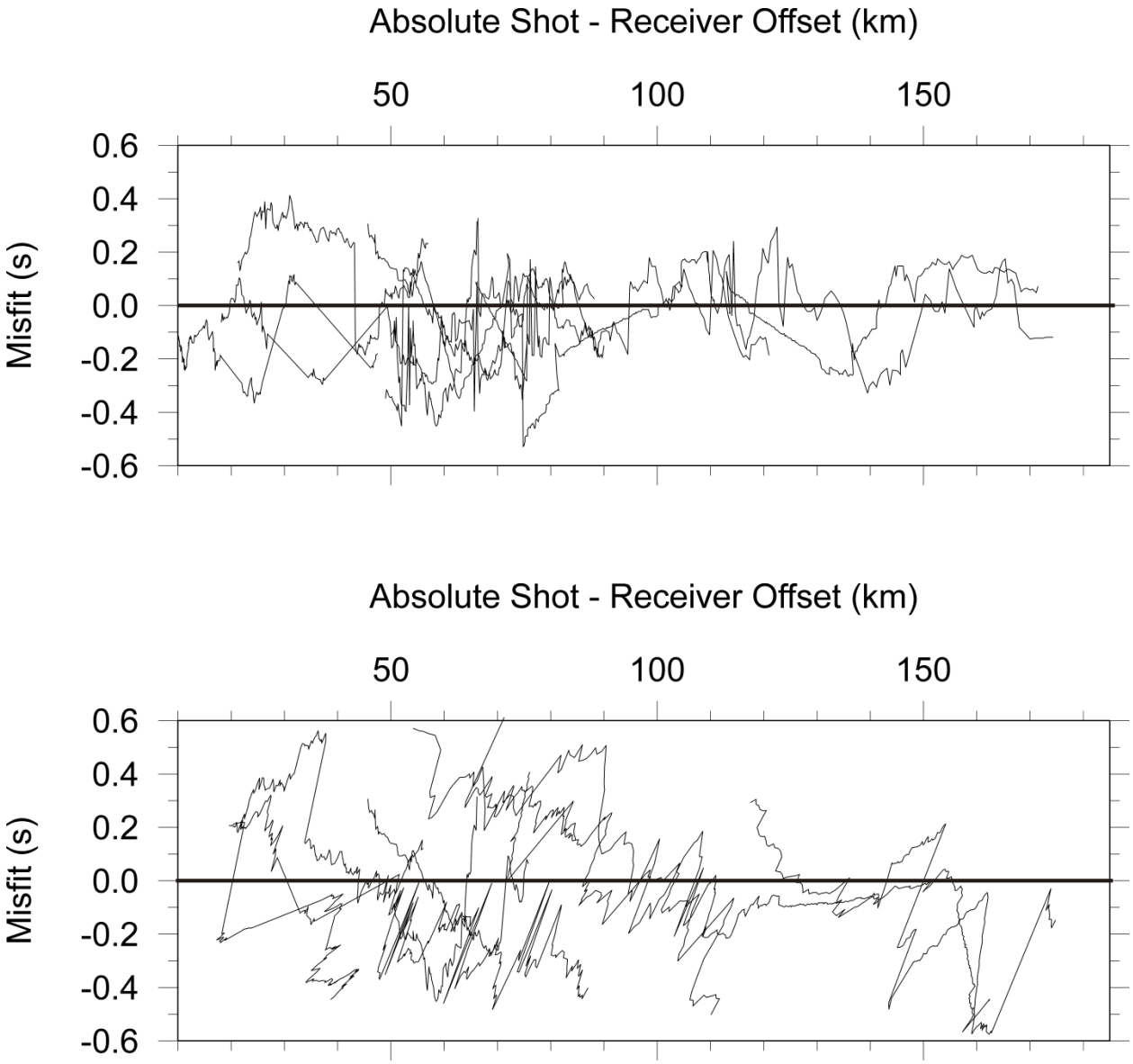

Figure 2.10 Travel-time misfit versus shot-receiver offset for the PmP reflection from the Moho under the eastern CPC. Each line represents a different shot. a) Misfits using the best velocity for the entire crust. b) Misfits using a velocity that is slightly too slow. The latter shows a weak systematic trend with offset, while the former is flat indicative of correct velocity.

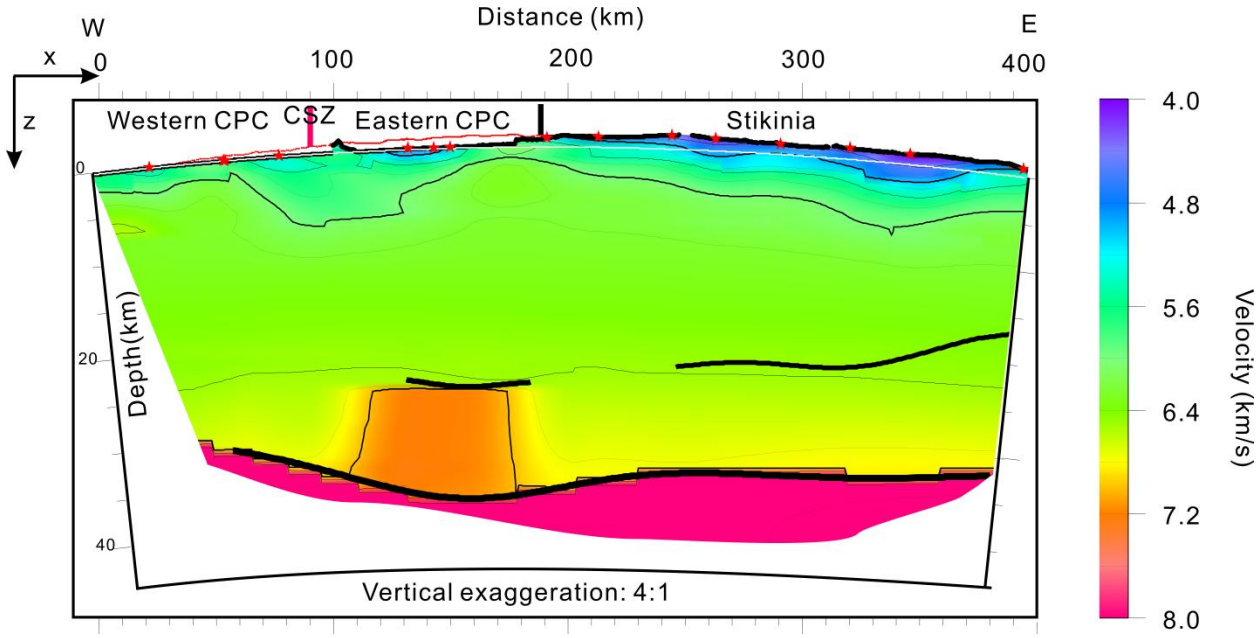

Figure 2.11 Seismic velocity model derived from the Batholiths controlled-source survey. Thick black lines indicate seismic reflectors. Velocity contour interval 0.25 km/s. Shots (stars) and seismographs (points) are shown at top. The red line is 10x10 km smoothed elevation. Thin white line indicates sea level. The curved surface, depth axes and the surrounding Cartesian box are the same as Figure 2.7. Simplified geology is shown at top: CPC, Coast Plutonic Complex; CSZ, Coast Shear Zone

	Shot 35	Shot 33	Shot 31	Shot 52	Shot 51	Shot 36	Shot 46	Shot 41	Shot 27	Shot 22	Shot 20	Shot 17	Shot 15	Shot 10	Shot 3	Shot1
Location-X (km)	21.27	53.11	55.55	76.55	76.42	131.52	142.76	149.7	190.95	213.03	244.23	262.85	290.65	320.36	346.1	394.6
Size (kg)	388	163	163	163	163	1020	265	959	898	959	714	510	816	592	796	816
Number of Pg	1110	931	951	538	621	901	825	1002	1535	1441	1321	1351	1251	1200	1323	1411
Number of PiP1	0	0	0	0	0	0	0	0	0	0	0	97	101	0	117	137
Number of PiP2	0	0	0	0	0	85	0	98	177	222	57	0	0	0	0	0
Number of P7	0	0	0	0	0	0	0	0	0	53	21	0	0	0	0	0
Number of PmP	871	0	0	0	0	327	432	644	1021	871	531	882	731	578	528	679
Number of Pn	538	0	0	0	0	0	0	331	358	287	131	245	231	107	198	254

Table 1. Shot information and number of travel-time picks for each phase at each shot

Chapter 3. Controlled-Source Shear-Wave Velocity Model of the Crust in the Coast Mountains Batholith Complex, Western Canada

3.1 Abstract

Body-wave seismic travel times were inverted to derive the crustal shear-wave velocity structure of the Coast Mountains in the central coast of British Columbia. The seismic refraction and wide-angle reflection data were acquired in 2009 as part of the multi-disciplinary Batholiths project investigating continental arc processes in the Jurassic to Eocene Coast Plutonic Complex. Previous P-wave modeling of the seismic data discovered a high-velocity (7 km/s) layer in the lower crust beneath the youngest (late Cretaceous to Eocene) portion of the arc complex. In addition to P waves, the seismic data also contain strong S-wave refracted arrivals from the upper crust and upper mantle, and S-wave reflections from the Lower crust and Moho. S-wave velocities of 3.3-3.6 km/s and a Vp/Vs ratio of 1.72 to 1.75 in the upper to middle crust are consistent with a felsic upper crust and a felsic to intermediate middle crust in both the batholith complex and the accreted Stikine island arc terrane. The lower crust under the Stikine terrane has velocity of 3.5-3.75 km/s and a ~1.78 Vp/Vs ratio, and is interpreted to consist of amphibolite or other hydrated mafic rocks. In contrast, the lower crust under the youngest portion of the batholith complex has a high S-wave velocity of >3.8 km/s coincident with the high P-wave velocity, and a ~1.81 VpVs ratio. This body is interpreted to have a bulk composition of mafic

garnet granulite. This garnet granulite and large volumes of granodiorite-dominated melt were created by arc dehydration melting of amphibolite (or hydrated gabbro) in the pre-existing lower crust.

3.2 Introduction

The average composition of continental crust is more felsic than the primary mafic magmatic differentiation product derived from the upper mantle [*Christensen,* 1996]. Large-scale re-melting of crustal materials occurs primarily in continental arcs above subduction zone, producing large felsic batholith complexes. However, a magmatic residue enriched with pyroxene and perhaps garnet is created by this second order differentiation [*Ducea,* 2002]. The fate of the residue plays an important role in the evolution of continental crust [*Herzberg et al.*, 1983; *Kay and Mahlburg-Kay*, 1991; *Ducea and Saleeby*, 1998].

The Coast Plutonic Complex (CPC) in western British Columbia is a huge Jurassic to Eocene batholith complex formed in a continental arc setting (Figure 3.1) [*Armstrong,* 1988]. After extensional collapse, the arc is now exposed at the middle crustal level [*Andronicos et al.*, 1999]. As a part of the Batholiths project, a 400-km long seismic refraction and wide-angle reflection profile was acquired across the CPC and adjacent Stikine terrane in 2009 (Figure 3.1) [*Stephenson et al.,* 2011; Chapter 2]. The P-wave velocity model generated by these data indicated the presence of a high-velocity 7.0-7.1 km/s layer in the lower crust beneath the Cretaceous to Eocene arc. Since knowledge of the S-wave velocity and Vp/Vs ratio would

provide stronger lithologic constraints on this structure, an S-wave velocity model is derived and discussed in this paper.

3.3 Tectonic and Geologic Setting

Collision and subduction processes, including voluminous magmatism, created the crust of British Columbia through interaction with oceanic plates of the Pacific basin [*Monger et al.,* 1982]. The Intermontane Belt amalgamated super-terrane, dominated in the study area by the Stikine volcanic arc terrane, and the Insular Belt super-terrane, dominated in the study area by the Wrangellia oceanic plateau, were accreted to North America by 170 Ma. Continental arc magmatism of the Coast Plutonic Complex obscured the suture between the super-terranes (Figure 3.1). Three main pulses of magmatism occurred in the CPC at ~150-120 Ma, ~120-80 Ma, and ~60-52 Ma [*Armstrong*, 1988; *Gehrels et al.*, 2009; *Cecil et al.*, 2011]. The CPC is cut by the ~800 km long Coast Shear Zone (CSZ), which experienced large-scale transpression and transextension [*Crawford et al.,* 1987; *Andronicos et al.,* 1999; 2003]. The batholiths to the west of the CSZ formed during the Jurassic to Cretaceous, while those to the east are Cretaceous to Eocene. A large Eocene magmatic pulse is synchronous with the end of subduction and initiation of arc extensional collapse [*Andronicos et al.,* 2003; *Depine et al.,* 2011].

3.4 Seismic Refraction and Wide-Angle Reflection Data

The Batholiths project acquired controlled-source seismic data across the CPC in 2009 (Figure 3.1, Chapter 2) [*Stephenson et al.,* 2011]. Sixteen inline contained explosive shots and 2

offline shots were recorded on 1811 vertical-component seismographs at 200 m spacing onshore and 500 m spacing along the channel shorelines. Shots were smaller in the west due to permit limitations, which, along with marine noise, affected the signal to noise ratio. In addition to P waves that illuminated the crust and upper-most mantle (Chapter 2), relatively strong S-wave arrivals are present in the data, despite the use of explosive shots (Figure 3.2). Observed S-wave arrivals include the direct or turning wave in the upper crust (Sg), weak reflections from the middle crust (SiS), reflections from the Moho (SmS), and a faint Moho refraction (Sn).

Because the S-wave energy arrives during the reverberating P-wave coda energy and is recorded on vertical-component seismometers, the signal to noise ratio is much worse than for the P waves. However, clear energy can be observed (Figure 3.2) and used to model the S-wave structure of the crust. Travel-time picking was aided by comparison to the P-wave travel times converted using geologically reasonable Vp/Vs ratios. On the eastern half of the line, the Sg arrivals are observed to ~140 km shot-receiver offset and picked with travel-time errors of ~80 ms. Because of the smaller shots and larger seismograph spacing, Sg could only be tracked to <100-120 km offset on the western half of the line. Mid-crustal reflections SiS are visible in the data, but cannot be accurately picked. Clear S-wave reflections from the Moho were observed from wide angles to zero offset, and were picked with an accuracy of about 60-80 ms. The S wave Moho refraction is weakly observed on east section of two shots in the middle of the line (shot 22, 27), and was picked with a large estimated error of 120-150 ms.

3.5 Data Analysis

The S wave travel time picks were inverted using a layer stripping approach similar to that of Chapter 2 (Figure 3.3). First arrival and reflection travel times were computed using a finite difference solution to the Eikonal equation [Hole and Zelt, 1995]. Travel time tomography [Hole, 1992] was used to invert 7982 Sg travel times from 10 shots to obtain the velocity of the upper crust. The starting velocity model was a linear gradient with depth. Smoothing with a horizontal to vertical aspect ratio of 8:1 was applied to the change in velocity at each iteration of the inversion. The initial smoothing was very large, and was decreased to a final smoothing of 40 x 6 km to produce the final upper crustal velocity model (Figure 3.5).

S-wave reflections were observed from the major P-wave reflectors (Figure 3.2), but the S-wave picks have much poorer accuracy. Therefore depth to the reflectors was fixed to the P-wave values and verified for consistency. The initial S-wave velocity of the middle and lower crust was derived from the results of Chapter 2 by dividing the P-wave velocity by the average crustal Vp/Vs ratio of 1.76 [Christensen, 1996]. The SiS and SmS arrival times were roughly consistent with the depths of the PiP7 and PmP reflectors. The S-wave reflection travel times were then used to fine-tune the S-wave velocity model for the middle and lower crust.

A strong reflector was observed in the P-wave data beneath the Cretaceous to Eocene arc east of the CSZ (Chapter 2). This reflector is present on shots (22 and 27) in the S-wave data, but is too weak to pick travel times (Figure 3.4). The P-wave travel-time picks converted at a range of Vp/Vs ratios were plotted directly on the S-wave data. The SiS phase is consistent with a

Vp/Vs ratio of 1.70-1.73, constraining the S-wave velocity above the reflector to be ~3.5 km/s (Figure 3.4).

A total of 5521 Moho reflection SmS travel times from 10 shots were then inverted for the velocity of the middle and lower crust using reflection tomography [*Zelt et al.,* 1996]. A non-geological boundary was derived from the base of the Sg ray coverage, and structure above this surface was kept fixed during modeling of deeper structure. Depth to the reflectors was also kept fixed. A very large smoothing of 60 x 15 km was applied to tomographic updates to the lower crustal velocity.

Finally, Sn arrivals from two shots were used to obtain the average S-wave velocity of the upper-most mantle.

The S-wave velocity model (Figure 3.5) was compared to the P-wave model of Chapter 2 to produce a smoothed 2-D model of the Vp/Vs ratio (Figure 3.6). However, since the accuracy of the travel times, the smoothing during tomography, and the final resolution are different for the two models, this image contains probable artifacts in the details. Taking the resolution of the images into account, average velocity in each major layer was estimated and Vp/Vs was computed. These larger-scale averages, printed on Figure 3.6, are accurate to ~0.02 and are more reliable estimates of bulk lithology.

3.6 Interpretation and Discussion

Shallow low velocity of <3 km/s extends to 3-5 km depth in the eastern half of the S-wave velocity model (Figure 3.5). A Vp/Vs of less than 1.7 is observed at lower resolution, with

probable smearing of shallow features to greater depth (Figure 3.6). The shallow low Vs and low Vp/Vs is interpreted to represent the Mesozoic Nechako Basin that locally overlies much of the Stikine terrane [*Stephenson et al.,* 2011]. Beneath the basin, the Stikine terrane east of the batholith complex has velocities of 3.4-3.5 km/s extending to ~20 km depth. The Vp/Vs ratio in the Stikine upper crust slowly increases to 1.73-1.74 (Figure 3.6). These values are consistent with previous work in the Stikine terrane [*Clowes et al.,* 2005], and are interpreted to represent a felsic to intermediate bulk composition in this accreted island arc complex. S-wave reflections from the Moho are consistent with the ~35 km Moho depth previously derived from the P-wave reflections (Chapter 2). The lower crust in the Stikine terrane has an S-wave velocity of 3.5-3.75 km/s and a ~1.78 Vp/Vs ratio (Figure 3.6), consistent with the results of Clowes et al. [2005]. The Stikine lower crust is interpreted to consist of amphibolite or other hydrated mafic rocks [*Christensen and Fountain,* 1975; *Christensen,* 1996].

In the Mesozoic CPC to the west of the CSZ, the S wave velocity is ~3.5 km/s through most of the crust and <3.7 km/s in the lower crust (Figure 3.5). The Vp/Vs ratio is ~1.75 (Figure 3.6). These values are in stark contrast to the mafic lower crust of the Wrangellia terrane to the west [*Yuan et al*., 1992], that exists in minor outcrops in the study area. The lower crustal Vs and Vp/Vs are more consistent with a diorite composition [*Christensen,* 1996]. Arc batholiths are interpreted to have mostly replaced the accreted terrane.

The youngest, Eocene, phase of the CPC is only located to the east of the CSZ. S wave velocity in this part of the model increases quickly to 3.5 km/s then remains nearly constant through the middle crust. The Vp/Vs ratio rises slowly from 1.72 to 1.75 by 25 km depth. These

values are consistent with felsic plutons of the CPC extending to the mid-crust, but are also similar to rocks of the Stikine terrane intruded by the arc.

S-wave reflections from the Moho are again consistent with the depth derived from the P-waves. The Moho deepens from ~35 km under Stikinia to ~37 km under the eastern batholith complex, then shallows toward the coast (Figure 3.5). The S-wave velocity of the upper-most mantle is about 4.7

In the lower crust, beneath the highest mountains and the youngest batholiths of the arc complex, where a high P-wave velocity was observed (Chapter 2), a high S wave velocity of >3.8km/s is also found (Figure 3.5). The Vp/Vs ratio in this layer exhibits a high value of ~1.81, consistent with the high Vp/Vs observed in an overlapping area by Calkins et al. [2010]. This high velocity and Vp/Vs ratio are interpreted to be mafic garnet granulite based on comparison to lab measurements [*Christensen and Fountain*, 1975; *Christensen*, 1996]. While the P-wave velocity is consistent with anhydrous gabbro composition, the Vs and Vp/Vs require the garnet granulite. This layer is interpreted to be the residue generated by partial melting of a hydrous mafic protolith such as amphibolite. The melting generated felsic melt of average granodiorite composition that rose to create the batholith complex in the upper crust [Armstrong, 1988]. The residue left behind by such melting would be mafic garnet granulite composed of clinopyroxene + orthopyroxene + garnet + quartz + plagioclase at >10kbar pressure at >25 km depth [*Beard and Lofgren*, 1991; *Douce and Beard*, 1995]. This more mafic residue could have been extracted from >35 to 40 km depth by magmatic differentation of previously accreted mafic arc magmas [*Ducea and Saleeby*, 1998; *Ducea*, 2002]. Alternatively, all of the accreted terranes that make up

the pre-existing crust in this region are of island arc or oceanic plateau origin, and could provide the protolith for continental arc formation.

3.7 Acknowledgements

This work was funded by National Science Foundation (NSF) grant numbers EAR-0310126 and EAR-XXXXXX in the USA and by the Natural Sciences and Engineering Research Council (NSERC) in Canada. We gratefully acknowledge the 67-person field crew, mostly student volunteers from 13 different universities. IRIS-PASSCAL provided the seismic instruments and field support. Several First Nations bands allowed the project on their traditional lands.

3.8 References

Andronicos, C. L., Hollister, L. S., Davidson, C., and Chardon, D. (1999), Kinematics and tectonic significance of transpressive structures within the Coast Plutonic Complex, British Columbia, *Journal of Structural Geology*, *21*(2), 229-243, doi:http://dx.doi.org/10.1016/S0191-8141(98)00117-5.

Armstrong, R. L. (1988), Mesozoic and early Cenozoic magmatic evolution of the Canadian Cordillera, *Geological Society of America Special Papers*, *218*, 55-92, doi:10.1130/SPE218-p55.

Beard, J. S., and Lofgren, G. E. (1991), Dehydration Melting and Water-Saturated Melting of Basaltic and Andesitic Greenstones and Amphibolites at 1, 3, and 6. 9 kb, *Journal of Petrology*, *32*(2), 365-401.

Calkins, J. A., Zandt, G., Girardi, J., Dueker, K., Gehrels, G. E., and Ducea, M. N. (2010), Characterization of the crust of the Coast Mountains Batholith, British Columbia, from P to S converted seismic waves and petrologic modeling, *Earth and Planetary Science Letters*, *289*(1–2), 145-155, doi:http://dx.doi.org/10.1016/j.epsl.2009.10.037.

Cecil, M. R., Gehrels, G., Ducea, M. N., and Patchett, P. J. (2011), U-Pb-Hf characterization of the central Coast Mountains batholith: Implications for petrogenesis and crustal architecture, *Lithosphere*, *3*(4), 247-260, doi:10.1130/l134.1.

Christensen, N. I. (1996), Poisson's ratio and crustal seismology, *J. Geophys. Res.*, *101*(B2), 3139-3156, doi:10.1029/95JB03446.

Christensen, N. I., and Fountain, D. M. (1975), Constitution of the Lower Continental Crust Based on Experimental Studies of Seismic Velocities in Granulite, *Geological Society of America Bulletin*, *86*(2), 227-236, doi:10.1130/0016-7606(1975)86<227:cotlcc>2.0.co;2.

Clowes, R. M., Hammer, P. T. C., Fernández-Viejo, G., and Welford, J. K. (2005), Lithospheric structure in northwestern Canada from Lithoprobe seismic refraction and related studies: a synthesis, *Canadian Journal of Earth Sciences*, *42*(6), 1277-1293, doi:10.1139/e04-069.

Crawford, M. L., Hollister, L., and Woodsworth, G. (1987), Crustal deformation and regional metamorphism across a terrane boundary, Coast Plutonic Complex, British Columbia, *Tectonics*, *6*(3), 343-361.

Depine, G. V., Andronicos, C. L., and Hollister, L. S. (2011), Response of continental magmatic arcs to regional tectonic changes recorded by synorogenic plutons in the middle crust: An example from the Coast Mountains of British Columbia, *Journal of Structural Geology*, *33*(6), 1089-1104, doi:http://dx.doi.org/10.1016/j.jsg.2011.03.012.

Douce, A. E. P., and Beard, J. S. (1995), Dehydration-melting of biotite gneiss and quartz amphibolite from 3 to 15 kbar, *Journal of Petrology*, *36*(3), 707-738.

Ducea, M. N. (2002), Constraints on the bulk composition and root foundering rates of continental arcs: A California arc perspective, *J. Geophys. Res.*, *107*(B11), 2304, doi:10.1029/2001JB000643.

Ducea, M. N., and Saleeby, J. B. (1998), The age and origin of a thick mafic–ultramafic keel from beneath the Sierra Nevada batholith, *Contr. Mineral. and Petrol.*, *133*(1-2), 169-185, doi:10.1007/s004100050445.

Gehrels, G., Rusmore, M., Woodsworth, G., Crawford, M., Andronicos, C., Hollister, L., Patchett, J., Ducea, M., Butler, R., Klepeis, K., Davidson, C., Friedman, R., Haggart, J., Mahoney, B., Crawford, W., Pearson, D., and Girardi, J. (2009), U-Th-Pb geochronology of the Coast Mountains batholith in north-coastal British Columbia: Constraints on age and tectonic evolution, *Geological Society of America Bulletin*, *121*(9-10), 1341-1361, doi:10.1130/b26404.1.

Hole, J. A. (1992), Nonlinear high-resolution three-dimensional seismic travel time tomography, *Journal of Geophysical Research: Solid Earth*, *97*(B5), 6553-6562, doi:10.1029/92JB00235.

Hole, J. A., and Zelt, B. C. (1995), 3-D finite-difference reflection travel times, *Geophysical Journal International*, *121*(2), 427-434, doi:10.1111/j.1365-246X.1995.tb05723.x.

Kay, R., and Mahlburg-Kay, S. (1991), Creation and destruction of lower continental crust, *Geologische Rundschau*, *80*(2), 259-278.

Mahoney, J. B., Gordee, S. M., Haggart, J. W., Friedman, R. M., Diakow, L. J., and Woodsworth, G. J. (2009), Magmatic evolution of the eastern Coast Plutonic Complex, Bella Coola region, west-central British Columbia, *Geological Society of America Bulletin*, *121*(9-10), 1362-1380, doi:10.1130/b26325.1.

Monger, J.W.H., and Brown, E.H. Tectonic evolution of the southern Coast-Cascade Orogen, northwestern Washington and southwestern British Columbia. Rocks, Fire, and Ice: The Geology of Washington. Edited by E. S. Cheney. University of Washington Press. In press

Monger, J. W. H., Price, R. A., and Tempelman-Kluit, D. J. (1982), Tectonic accretion and the origin of the two major metamorphic and plutonic welts in the Canadian Cordillera, *Geology*, *10*(2), 70-75, doi:10.1130/0091-7613(1982)10<70:taatoo>2.0.co;2.

Parsons, T., Mccarthy, J., Kohler, W. M., Ammon, C. J., Benz, H. M., Hole, J., and Criley, E. E. (1996), Crustal structure of the Colorado Plateau, Arizona: Application of new long-offset seismic data analysis techniques, *Journal of geophysical research*, *101*(B5), 11173-11111,11194.

Stephenson, A., Spence, G., Wang, K., Hole, J., Miller, K., Clowes, R., Harder, S., Kaip, G., and Mareschal, J.-C. (2011), Crustal velocity structure of the southern Nechako basin, British Columbia, from wide-angle seismic traveltime inversion 1 1 This article is one of a series of papers published in this Special Issue on the theme of New insights in Cordilleran Intermontane geoscience: reducing exploration risk in the mountain pine beetle-affected area, British Columbia, *Canadian Journal of Earth Sciences*, *48*(6), 1050-1063.

Yuan, T., Spence, G., and Hyndman, R. (1992), Structure beneath Queen Charlotte Sound from seismic-refraction and gravity interpretations, *Canadian Journal of Earth Sciences*, *29*(7), 1509-1529.

Zelt, B. C., Ellis, R. M., Clowes, R. M., and Hole, J. A. (1996), Inversion of three-dimensional wide-angle seismic data from the southwestern Canadian Cordillera, *J. Geophys. Res.*, *101*(B4), 8503-8529, doi:10.1029/95JB02807.

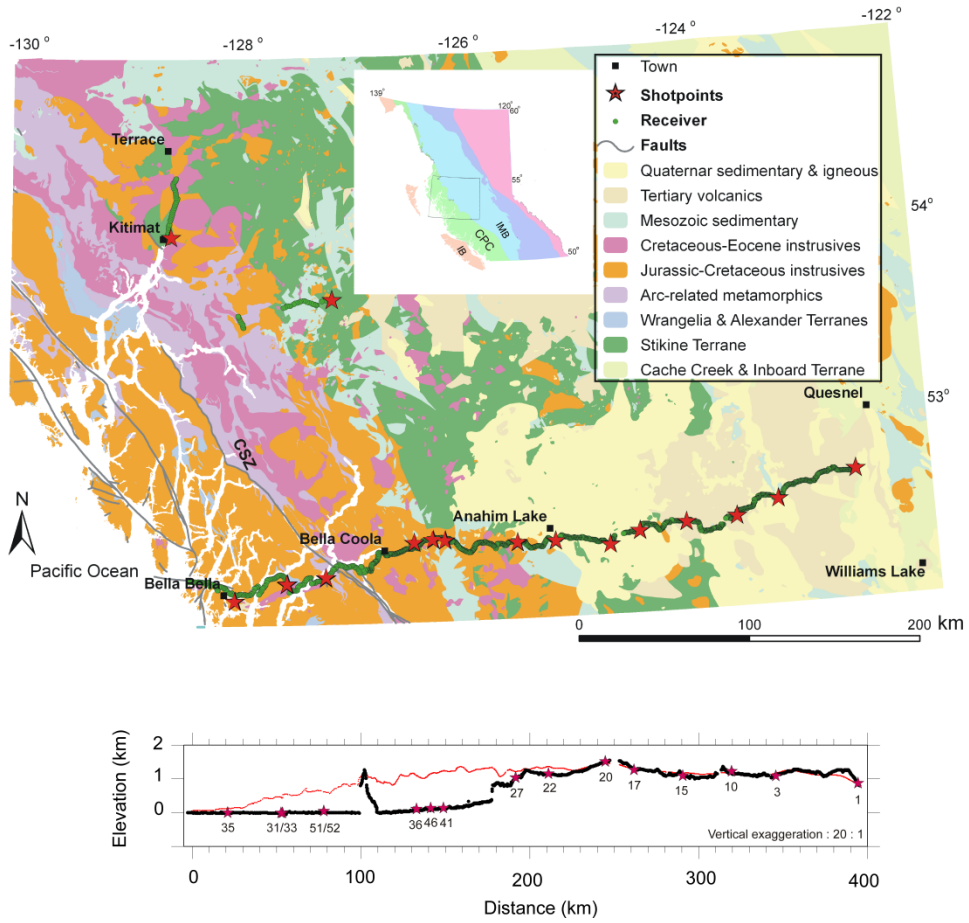

Figure 3.1 Map of the Batholiths wide-angle seismic survey and geology. Stars are seismic shots and green circles are the seismographs. Index map shows geologic provinces of British Columbia, Canada. CPC is Coast Plutonic Complex; IMB, Intermontaine Belt superterrane; IB, Insular Belt superterrane. At bottom is an elevation profile along the seismic

line at a vertical exaggeration of 20:1. The red line is elevation averaged over a 10x10 km area. Shots and seismographs in the CPC were deployed in deep glacial valleys and fjords.

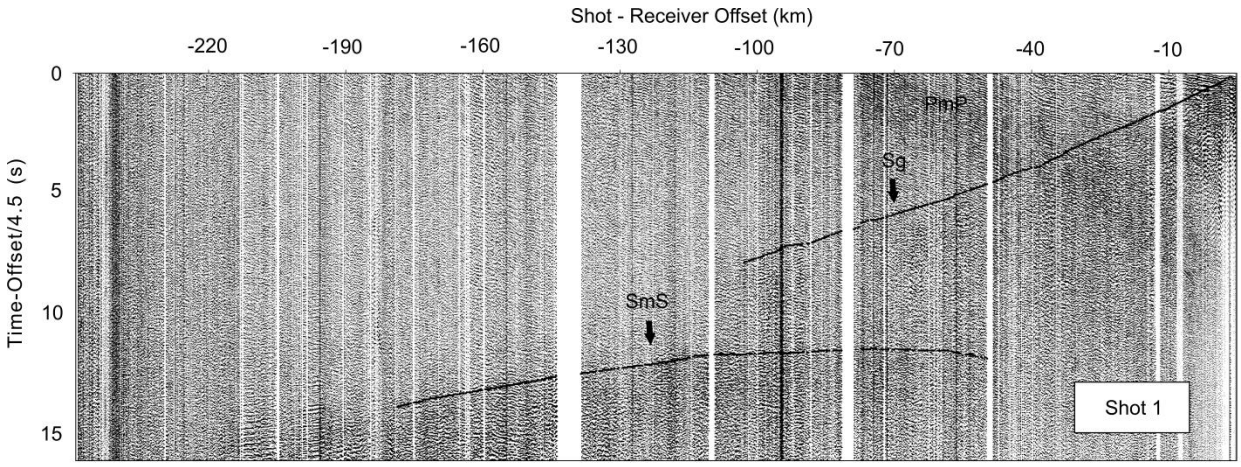
Shot - Receiver Offset (km)
-220
-190
-160
-130
-100
-70
-40
-10
0
5
10
15
Time-Offset/4.5 (s)
PmP
Sg
SmS
Shot 1

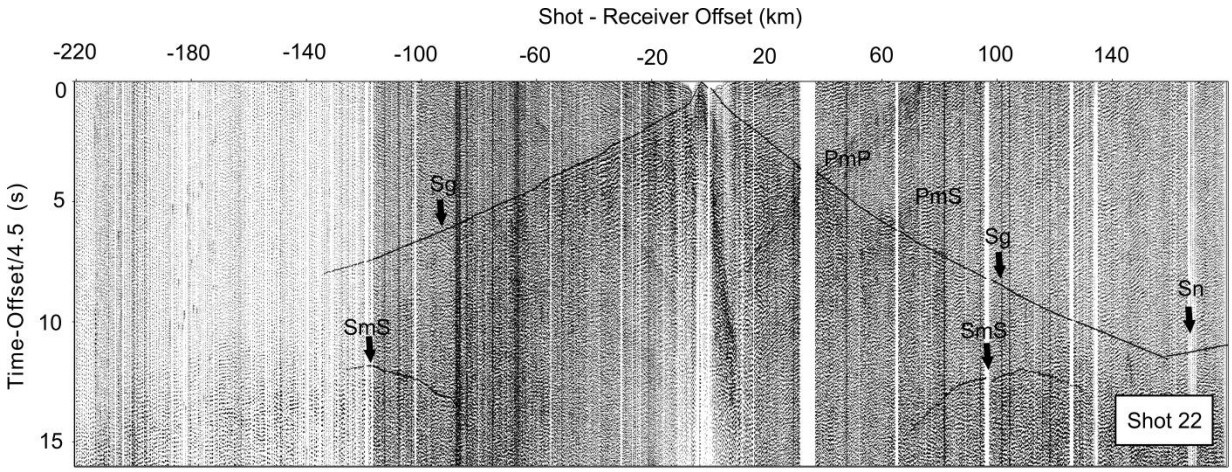
Shot - Receiver Offset (km)
-220
-180
-140
-100
-60
-20
20
60
100
140
0
5
10
15
Time-Offset/4.5 (s)
Sg
SmS
PmP
PmS
Sg
Sn
SmS
Shot 22

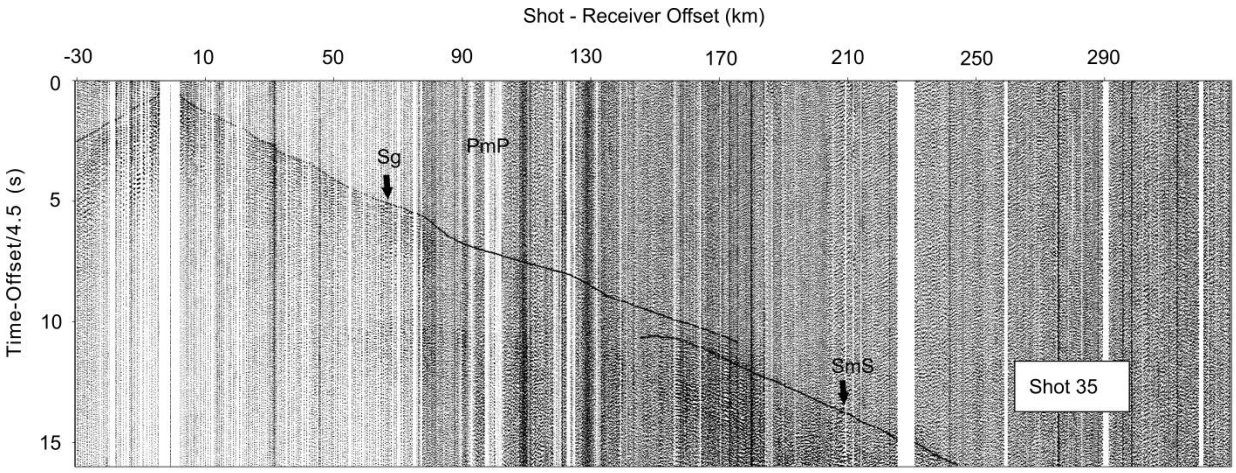

Figure 3.2 Shot 1, 22, 35 seismic gather. Travel-time picks are shown as darker symbols. The time axis is plotted with a reducing velocity of 4.51 km/s. A 2-18 Hz bandpass filter and trace amplitude balancing have been applied. Major Shear wave seismic arrivals are labeled (see text for description).

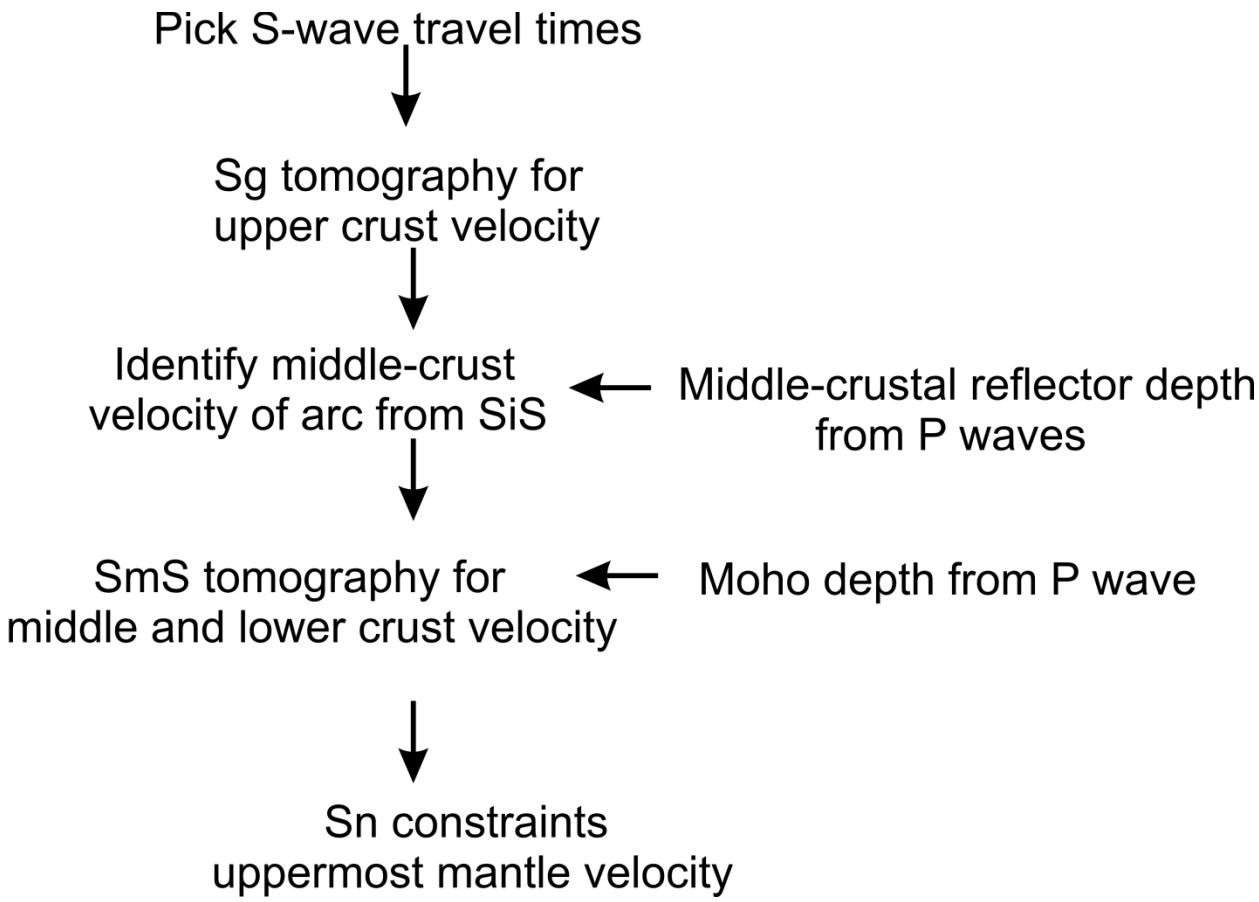

Figure 3.3 Flowchart of the 3-D modeling procedure, modified from [*Parsons et al.*, 1996]

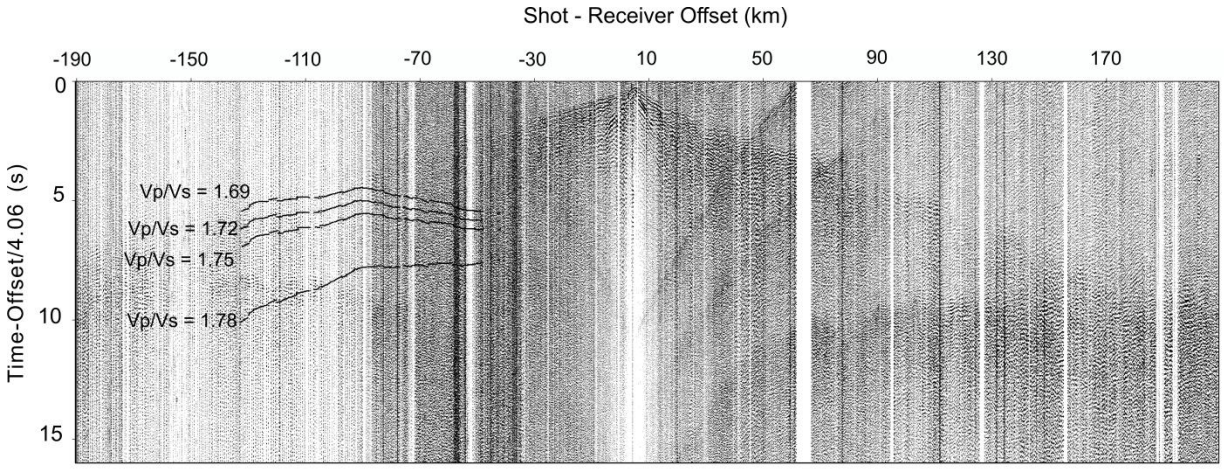

Figure 3.4 Lower crust P wave reflection PmP divided by different Vp/Vs ratio to match the S wave reflection SmS for middle crust velocity analysis

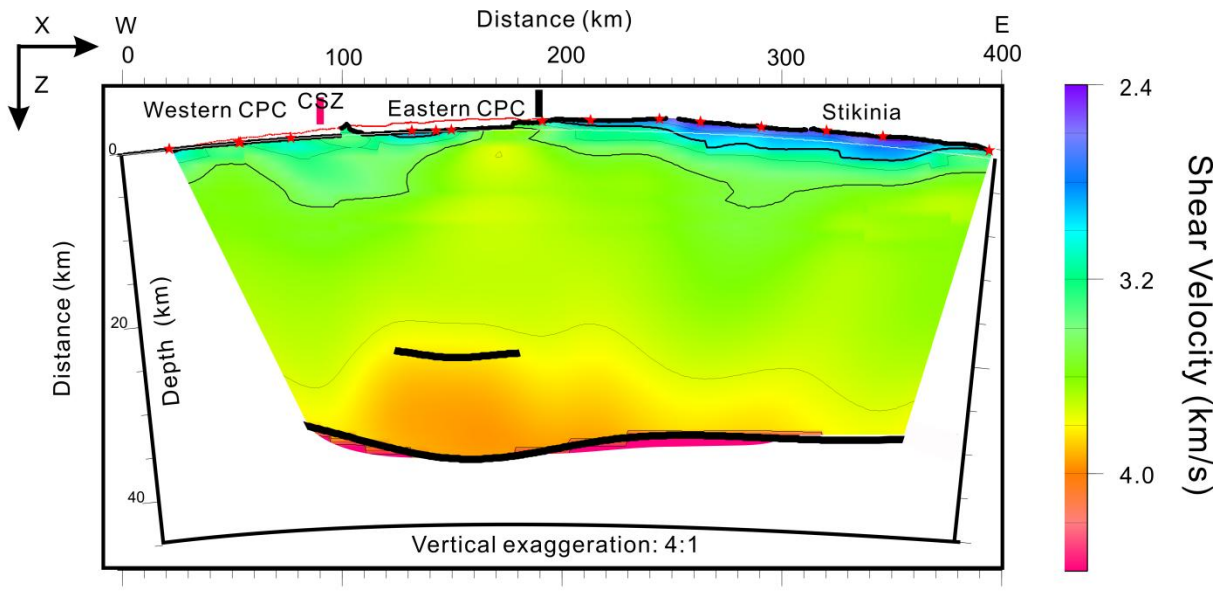

Figure 3.5 Shear wave velocity model derived from the Batholiths controlled-source survey. Thick black lines indicate seismic reflectors. Velocity contour interval 0.25 km/s. Shots (stars) and seismographs (points) are shown at top. The red line is 10x10 km smoothed elevation. Thin white line indicates sea level. The non-parallel depth axes and curved Earth surface represent the spherical Earth. Modeling was performed within a Cartesian coordinate system represented by the surrounding square box and X-Z directions. Simplified geology is shown at top: CPC, Coast Plutonic Complex; CSZ, Coast Shear Zone.

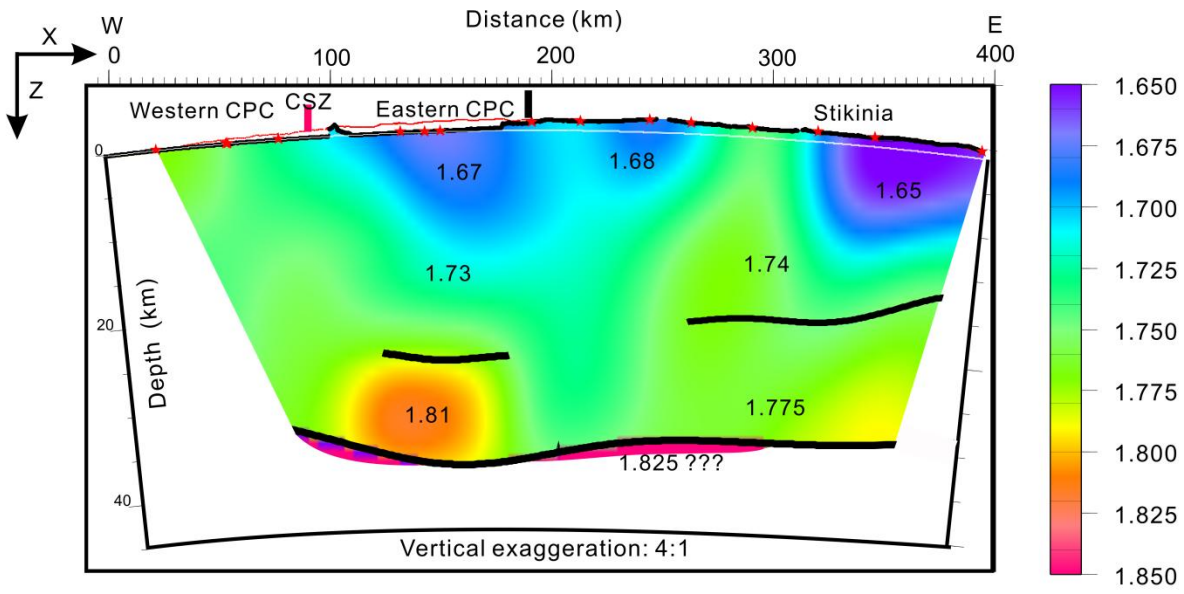

Figure 3.6 Smoothed Vp/Vs ratio model derived from the P-wave model of Chapter 2 and the S-wave model of Figure 3.5. Larger-scale averages of the major layers are written on the model, and are probably more representative than the color image.

Chapter 4. Aftershock Source Imaging using Reverse Time Migration from the Dense AIDA Array Deployed after the 2011 Virginia Earthquake

4.1 Abstract

Reverse time migration was applied to image aftershocks of the 2011 magnitude 5.8 earthquake in Virginia. The data were recorded AIDA (Aftershock Imaging with Dense Arrays), which deployed stations at 200-400 m spacing (200-400 m) to record wavefields with reduced spatial aliasing. AIDA detected events with magnitudes as small as –2, and an earlier study produced a high-resolution velocity model and hypocenters. In this study, events with signal smaller than the noise were successfully migrated to a point source with a spatial resolution of ~200 m. Events larger than magnitude 2.5, including the largest event at magnitude 3.7, showed three-dimensional energy propagation as a function of time. This slip propagation is real, as it is not observed for smaller point sources and is much larger than resolution of the array in synthetic data tests. The distance of slip propagation, however, is too large for an earthquake of that magnitude, and the speed of slip propagation is also too large, comparable to the P-wave speed. The amount of slip expected is not much larger than the spatial resolution of the images, so the slip propagation may be over-estimated. Alternatively, the events may be doublets, with the second sub-event triggered by the P-wave. The resolution of the images was limited by the low temporal sampling rate, which was caused by the limited memory of the seismographs. Synthetic

data tests show that a higher sampling rate would have resulted in proportionally better spatial resolution.

4.2 Introduction

The seismic reverse time migration (RTM) method was developed in the 1980's for reflection imaging in the petroleum industry [*McMechan,* 1982; *Baysal et al.,* 1983, *Chang and McMechan,* 1987]. The method takes advantage of the reversibility of the wave equation to study the propagation of an observed wavefield backwards through a known velocity model to a source, scattering point, or seismic reflector. Compared with other migration imaging methods, RTM is more stable in the presence of strong velocity variation and produces better resolution of complex structures [e.g., *Zhu and Lines, 1998*]. However, an accurate velocity model is necessary and it is more computationally expensive. The method has been used in industry to image complex subsurface structures such as petroleum reservoirs beneath salt tectonics.

Early papers showed that RTM could be used to directly image earthquake sources [*McMechan,* 1982; *McMechan et al*., 1985; *Chang and McMechan,* 1991]. However, the method requires recording a densely sampled, spatially non-aliased, and wide-aperture wavefield. It also requires the existence of an accurate seismic velocity model. Datasets that satisfied these conditions were rare until recently. Using data from regional arrays that are both spatially large and densely sampled, RTM has recently been used to back-project energy through global velocity models to the source region of large earthquakes [*Ishii et al.,* 2005; *Kiser et al.,* 2011; *Kiser and Ishii,* 2012]. The resulting images have had sufficient resolution to illuminate energy

release as a function of time and space, tracking slip along the fault surface and improving our understanding of rupture mechanics. In addition to large subduction-zone earthquakes [e.g., *Ishii et al.,* 2007; *Kiser and Ishii,* 2012], the method has been applied to earthquakes in China [*Xu et al.,* 2009] and Italy [*D'Amico et al.,* 2010] and is likely becoming routine for large earthquakes globally. The network station spacing and knowledge of the 3-D velocity model limit the shortest period that can be used, providing the ultimate limit on the spatial resolution. The stacking of amplitude envelopes, rather than full waveforms [e.g., *Jakka et al.,* 2010; *Chao et al.,* 2013], allows the migration of events using sparser networks, but also limits the spatial resolution. Slip propagation along the fault has only been resolved to date for earthquakes greater than magnitude 6.8.

At the other end of the spatial scale, industry has recently been using RTM to image hydraulic fracturing events and induced seismicity [e.g., *Gajewski and Tessmer,* 2005; *Chambers et al.,* 2010; *Artman et al.,* 2010; *Zhebel and Eisner* 2012]. Imaging is achieved through temporary, dense seismic arrays in the borehole or at the surface. Events with signal-to-noise ratio much less than one, with no visible arrivals on the individual seismograms, have been imaged [e.g., *Chambers et al.,* 2010]. Only point sources are imaged, not slip propagation, due to the very small magnitude (less than –2) of hydraulic fracturing events.

This paper addresses the gap between industry application for migration of tiny hydraulic fracturing events and academic application for migration of large, damaging earthquakes. RTM is used to image aftershocks of the 2011 magnitude 5.8 earthquake in central Virginia. Four days after the main shock, the Aftershock Imaging with Dense Arrays (AIDA) project deployed a

dense array to record 12 days of the aftershock sequence [*Davenport et al.*, 2014]. AIDA deployed high-frequency vertical-component seismographs at up to 201 stations at a 200-400 m spacing to drastically reduce spatial aliasing. The AIDA array easily detected aftershocks smaller than magnitude –1.5 [*Davenport et al.*, 2014], much smaller than the detection threshold of the overlapping traditional sparser aftershock networks. Davenport et al. [2014] used AIDA arrival time data to produce a velocity model of the epicentral area with a spatial resolution of ~1 km. Aftershocks were located with an absolute hypocentral accuracy of ~100 m without using the double-difference method.

In this paper, this velocity model is used for three-dimensional RTM of selected events, and the results are calibrated with known hypocenters. Migration results are shown for aftershocks with magnitudes from 3.7 to about –2. Synthetic data from a single point source and a multiple-asperity fault-plane source are used to test the spatial and temporal resolution of the RTM method and AIDA dataset.

4.3 2011 Virginia Earthquake

On August 23, 2011, a magnitude 5.8 earthquake occurred in Louisa County in central Virginia (Figure 4.1). The 2011 event is the largest ever recorded within the central Virginia seismic zone (CVSZ) [*Bollinger,* 1969; *Bollinger and Sibol,* 1985; *Chapman,* 2013]. Seismicity within the CVSZ occurs from 4 to 12 km depth over a broad area, within overthrust sheets of the crystalline Piedmont province of central Appalachia. Both reverse and strike-slip motion have

been recorded, both with a southeast - northwest compression direction [*Munsey and Bollinger,* 1985; *Kim and Chapman,* 2005].

The 2011 event occurred at a depth of 8.0 km on a southeast-dipping thrust fault [*Chapman,* 2013]. The depth and focal plane do not correspond with any known fault [*Pratt et al.,* 2014]. The main shock consisted of three distinct sub-events which together propagated to the northeast and up dip [*Chapman,* 2013]. Stress drops on the main and previous events are high 50-75MPa, with relatively slow rupture velocities of 1.3-1.7 km/s [*Chapman,* 2013].

4.4 AIDA Dataset

AIDA used high-frequency 4.5 Hz vertical geophones and single-component RT-125A "Texan" seismographs from the EarthScope Flexible Array maintained by IRIS/PASSCAL [*Davenport et al.,* 2014]. The instruments were designed for controlled-source data acquisition, and due to their light weight and ease of use, a large number can be deployed by a small crew in a single day. The shortcomings of the seismographs are that they are single-component and have limited battery life and data memory. A low sampling rate of 100 samples per second was used, which required swapping batteries in the field every third day and picking up the instruments for data recovery every six days.

A higher sampling rate would have been preferred but would have required more rapid battery changes and data recovery. The sampling rate ultimately limited imaging resolution.

On August 27th, 4 days after the main shock, 103 stations were deployed along two 7-11 km linear profiles at 200m spacing (lines 1 and 2, Figure 4.1b). On September 1st, an additional

30 three-component "triple-Texan" stations were deployed along a 60-km regional profile at 2 km spacing (line 3, Figure 4.1b). The original 103 seismographs were picked up for data download on September 2nd, and re-deployed on September 3rd with 14 new seismographs along the original and additional lines at 200-400m spacing (Figure 4.1b). The new lines were better centered on the aftershock zone. With the exception of the 3-component line, which was not used here, the aperture of AIDA is ~12 km.

Plots of the data (Figure 4.2) demonstrate strong correlation between stations and clear P, S, and secondary phases. The arrival time curvature, or moveout, depends upon the hypocenter location and time and the three-dimensional seismic velocity structure. Signal correlation between the densely spaced stations enabled AIDA to detect over 1700 aftershocks in the first 100 hours [*Davenport et al.*, 2014].

The largest aftershock recorded by AIDA had a magnitude of 3.7 (Figure 4.2a). Events larger than about magnitude 2 were clipped by the seismometers, which were not designed for strong ground motions. However, the timing and phase of the recorded energy can still be used to migrate for source location.

AIDA recorded many tiny aftershocks less than magnitude 0 and detected aftershocks as small as magnitude –2 (Figures 4.2b and 2d). These very small events have a signal-to-noise ratio less than 1 and are only detectable due to correlation between closely spaced stations. Traditional aftershock networks cannot detect such small events. Traditional arrival time and amplitude methods are very difficult to use with such low signal-to-noise ratio, but direct imaging methods can take advantage of the coherence of the energy across the array.

The aftershocks generated signal up to AIDA's 50 Hz Nyquist frequency and probably much beyond. As a result, the dominant frequency of the AIDA data is about 25 Hz. The sampling rate may limit resolution for the reverse time migration.

4.5 Reverse Time Migration Method

The seismograms received by the seismic array contain information about source through the arrival time, amplitude, and changes in the waveforms as a function of station location. The energy contained in each seismogram can be reverse-time migrated back to each grid point of potential source locations to unravel the source energy release.

The ground shaking $S_i(t)$ that originated at the ith potential source location as a function of time t is computed from:

$$S_i(t) = \frac{1}{N} * \sum_{k=1}^{n} a_k u_k(t - t_{ik}) \qquad (1)$$

where $u_k(t)$ is the observed seismogram at the kth station, and t_{ik} is the predicted travel time between source point i and station k calculated within the 3-D velocity model [e.g., *Ishii et al.*, 2007]. The weighting factor a_k is equal to ±1, and accounts for polarity of the observed waveform due to the moment tensor or propagation effects. It is calculated by cross-correlation of each seismogram with a reference trace for that event. The maximum cross-correlation produces two useful by-products: the polarity can be used to constrain the moment tensor, and the arrival times can be used for traditional tomography. Cross-correlation will not

work with a low signal-to-noise ratio. If no clear spatial pattern is observed in the polarity, a_k is set to one and it is hoped that positive and negative polarities will not perfectly cancel during stacking.

Equation (1) is trace stacking along the moveout curve defined by . It is a simplification of full-wavefield RTM as it accounts only for travel time and not for wave-propagation effects upon amplitude. Si(t) is computed for all potential source points i to create a 4-D volume of source emission as a function of 3-D position and time. Instead of plotting the phase of the stacked seismograms $S_i(t)$, energy is computed by squaring the samples and integrating over a time corresponding to the dominant period. This is not absolute energy, as wave-propagation effects were not computed, but it is relative energy within a limited source region.

Travel times were computed in a 3-D seismic velocity model that was determined from a tomographic inversion of aftershock arrival times [Davenport et al., 2014]. P and S-wave arrival times for over 300 aftershocks were picked from the AIDA array and inverted in a joint hypocenter and velocity inversion. Even though the data are capable of resolving structure at the kilometer scale, the observed arrival times are consistent to <20 ms with a homogeneous P-wave velocity of 6.2 km/s between the aftershock zone and AIDA array. This homogeneous velocity is consistent with the earthquake occurring within a single crystalline-rock terrane [*Davenport et al.*, 2014]. Predicted travel times in equation (1) were computed in 3-D using the finite-difference eikonal algorithm of Hole and Zelt [1995], even though in this case the velocity was homogeneous. One advantage of this algorithm is that, treating each station as a source, it efficiently computes travel times to all nodes of a complex gridded velocity model.

4.6 Synthetic Data Tests

In order to test the resolution of RTM with AIDA data, synthetic data were computed in the same velocity model and station geometry. Travel times were computed to generate a Green's function for a spatial and temporal point source. The delta-function seismograms were computed at a high sampling rate for accuracy, then anti-alias filtered for a 50 Hz Nyquist frequency and re-sampled to the AIDA sampling rate of 100 samples per second. The resulting synthetic seismograms have a dominant frequency of ~25 Hz, similar to the real data. Ten percent random noise was added to the synthetic data.

4.6.1 Point Source

Synthetic data for a point source under the array (Figure 4.3) were migrated to a 50m grid spacing. The results (Figure 4.4) successfully image the source at the correct location with a spatial resolution of <100m and temporal resolution of the dominant period. No significant artifacts are observed; the modest 10% noise is destructively stacked out by the migration.

The resolution of RTM is constrained by the array geometry and data frequency. To test the effects of AIDA's sampling rate and geometry, synthetic data were created with an anti-alias Nyquist frequency of 250 Hz and sample rate of 500 samples per second. RTM at a grid spacing of 10 m (Figure 4.4b) produced a much sharper image, with a spatial resolution of <30 m and a temporal resolution corresponding to the dominant period of 8ms. Minor smearing is visible from the effects of the array geometry.

These results indicate that AIDA's low sampling rate will be the primary limiting factor for RTM spatial resolution. The low sampling rate was required only by memory and power limitations of the 1990's-era seismographs. For AIDA aftershocks with modest noise and an accurate velocity model, RTM should produce a source resolution of ~100 m. Errors caused by the velocity model should be minimal as the arrival time data were fit to less than half of the dominant period. The velocity model itself was limited in part by the sampling rate, as picked arrival times would have been more accurate if higher frequencies had been recorded. It is difficult to simulate the effects of migrating aftershocks with a poor signal-to-noise ratio, as realistic noise is correlated between closely spaced stations. Aftershocks that occur outside the array were not migrated, but could be smeared due to the array aperture [e.g., Ishii et al., 2007].

4.6.2 Fault Plane Source

In order to test the ability of the AIDA array to resolve slip propagation along a larger fault, synthetic data were created for a 1.4 x 0.7 x 0.7 km fault with strike and dip at angles relative to the migration grid (Figure 4.5). Point-source sub-events were set off at a rupture velocity of 2.7 km/s, a realistic rupture speed for the study area. A total of 64 sub-events at 100 m spacing occurred over a duration of 500 ms. The synthetic data have a correspondingly long signal duration (Figure 4.5).

The RTM results (Figure 4.6) show clear propagation of slip along the fault. However, only a subset of the sub-events that occur within a short time, less than the dominant period, are imaged. Energy is correctly imaged at 200-300 m resolution, with larger errors in the vertical direction. The average rupture speed and direction are accurately resolved. Migration of a similar

fault, but with sub-events spaced 200 m apart, clearly resolved individual asperities, each with ~100 m resolution. These tests suggest that sub-events more than 200 m apart or more than 40 ms apart can be resolved by the AIDA data. Perhaps not unrelated, the dominant wavelength in these data is ~250 m – and could have been shorter if a faster sampling rate was used.

4.7 Virginia Aftershock Imaging

Representative aftershocks recorded by AIDA were imaged by reverse time migration at a 50 m grid spacing in the velocity model derived from travel time tomography.

4.7.1 Magnitude 3.7 Earthquake

The magnitude 3.7 earthquake (Figure 4.2a) was the largest event recorded by AIDA. Amplitudes were clipped by AIDA's controlled-source seismometers, but the recorded waveforms still indicate timing and polarity for migration. Cross-correlation indicates first motions were upward for all AIDA stations (Figure 4.7a). During the first deployment, the AIDA array aperture was limited and displaced mostly to the east of the primary aftershock zone. Upward motion on this array is consistent with the moment tensors of both the main shock and this aftershock, which indicate an east-southeast – west-northwest thrust mechanism and nodal planes that project to the west and east of the AIDA array [*Herrmann,* 2011].

The RTM images of this aftershock show a zone of energy release ~200 m across that moves ~300 m southward and ~500 m shallower in later time slices (Figure 4.8). Using only the stations that recorded the M3.7 event, RTM of a point source does not produce an image that

moves through time. Migration of the planar source indicates a spatial resolution of ~300m, with larger errors in the vertical direction. Figure 4.8 shows slip propagation much larger than the resolution of the synthetic tests and larger than the resolution of point-source events, and it is therefore interpreted to be real. However, it is spatially poorly resolved, particularly in the vertical direction. Slip apparently propagates at ~6 km/s, more than double realistic values for this region. The slip propagates very roughly along the σ_2 intermediate stress direction, so cannot distinguish whether slip occurred on a plane parallel or conjugate to that of the main event. It is unclear whether these unusual numbers are indicative of spatial resolution of the images or whether the apparent slip represents sub-events on different faults.

4.7.2 Magnitude –0.1 Earthquake

The ability of RTM was tested with a magnitude –0.1 aftershock that was only recorded on the poorer array of the first AIDA deployment (Figure 4.2b). The signal-to-noise ratio for the P waves for this event ranged from 3:1 to less than 1:1. Determination of the first motion polarity is less accurate, however, cross-correlation indicates that most stations moved up and the remainder are randomly distributed (Figure 4.7b). Again, this is consistent with the focal mechanism of the main shock. RTM successfully produces a point-source image of this event with a spatial resolution of ~200 m (Figure 4.9). The image is not as sharp, and is stretched in the southward and depth directions due to the limited array geometry. RTM provided a stable and effective way to accurately locate this small event.

4.7.3 Magnitude 2.6 Earthquake

During the second week of the AIDA deployment, additional lines 3, 4, 5, and 6 were deployed to better cover the aftershock zone (Figure 4.1). The magnitude 2.6 aftershock of Figure 4.2c was the largest event recorded by this improved array. First motions determined by cross-correlation indicate a distinct focal plane striking 35-50˚ (Figure 4.7c). This orientation is 5-15˚ clockwise from the strike of the aftershock zone is ~3 km to the east of the projection of the aftershock zone. Distance of the focal plane from the hypocenter indicates a >70˚ dip. Motions are consistent with reverse fault motion. This event occurred in the northern portion of the aftershock zone, where Davenport et al. [2014] suggested a minor clockwise change in strike and a more curving dip of the aftershock zone.

RTM images of this event show that the source moved ~150m eastward, and ~450m upward (Figure 4.10). This direction is inconsistent with the focal plane defined by cross-correlation. The direction is too steep for a shallowly dipping conjugate focal plane, yet the first motions do not detect a second steeply dipping plane crossing the array. Similar to the M3.7 event, the rate of slip propagation is ~6 km/s. Again, the images appear to clearly indicate slip propagation, but are hard to reconcile with slip on a single fault.

4.7.4 Magnitude –2 Earthquake

To demonstrate the ability to image events with signal smaller than the noise, the aftershock of Figure 4.2d was migrated. The event is estimated to have a magnitude of about –2 (negative two). Coherent S-wave arrivals can be seen on several stations, but the P-waves are barely visible. The epicenter can be estimated by the visual observation of coherent arrivals, but

arrival times cannot be picked for hypocenter determination. Cross-correlation was not consistently able to determine first motions (Figure 4.7d), so polarity was ignored during migration. This assumes that positive and negative polarities are not balanced, and therefore will not fully cancel one another. RTM successfully imaged focused energy for this event with a spatial resolution of ~300 m (Figure 4.11). The location of the event is within the dominant aftershock zone of Davenport et al. [2014].

4.8 Discussion and Conclusions

The densely sampled AIDA array enabled direct wavefield migration imaging of small aftershocks of the 2011 Virginia M5.8 earthquake. The RTM method requires a good velocity model, which was be derived from the AIDA data by traditional arrival time picking and joint velocity-hypocenter tomography. For all aftershocks with signal above noise, cross-correlation is a simple, efficient process to derive arrival times for traditional hypocenter-velocity tomography and to derive first motions for a focal mechanism. The density of stations enables a high-resolution velocity model and hypocenters [*Davenport et al.*, 2014]. If the aperture of the array is sufficiently large to include a focal plane, the location of this plane can be determined very accurately.

The AIDA array imaged and located events too small to detect on traditional aftershock arrays. Events as small as magnitude –2, with signal smaller than the noise, were successfully imaged. RTM could be used for automated detection and location of tiny events, but this has not yet been performed due to the computational effort. The only need is a good velocity model over

the volume to be scanned. The resolution for small, effectively point-source events is ~200 m for the AIDA dataset, slightly better horizontally and worse vertically.

Migration of AIDA data for aftershocks larger than magnitude 2.5 imaged energy at later times that propagated away from the hypocenter. This is not an artifact, as similarly propagating energy was not observed for smaller point sources. The synthetic tests for a finite fault showed that the resolution of distinct sub-events was 2-3 times worse than for a point source, with the largest errors in the vertical direction. Events larger than magnitude ~3 should have a slip patch larger than the ~200 m resolution of point sources, but even the magnitude 3.7 event is in the range where distinct sub-events could be difficult to resolve. Slip on the magnitude 2.6 and 3.7 events apparently moved 400-600 m over 70-100 ms. Other events in the CVSZ suggest a high stress drop [*Kim and Chapman,* 2005; *Chapman,* 2013], which would suggest a smaller slip patch for magnitude 2.6-3.7 events. The imaged energy propagated at ~6 km/s, which is too fast for slip propagation on a single fault. The largest imaged motion was vertical, which is the direction of largest errors in the synthetic tests. It is possible that the amount of movement was over-estimated by marginal resolution. Alternatively, both of the aftershocks may have triggered a nearby secondary event. The apparent speed of slip propagation is appropriate for P-wave triggering. Double and triple events are known in the CVSZ, including the 2011 main shock [*Kim and Chapman,* 2005; *Chapman,* 2013], but the relative timing of these events indicated much slower propagation.

The synthetic data tests show that the temporal sampling rate is the limiting factor for the resolution of migration images from AIDA data. Much higher frequencies were available in

Virginia due to the shallow depth of the earthquakes, short distance between the earthquakes and array, and low attenuation in crystalline bedrock. AIDA's sampling rate was low to enable a longer deployment with the limited memory of the seismographs. Had a higher sampling rate been used, the images would have been of proportionally better resolution.

On the other hand, AIDA's spatial geometry, both station density and array aperture, are sufficient for high-resolution migration imaging of the aftershocks. The first deployment's aperture was too small to identify a focal plane, and produced a migration image with lower resolution. The grid of lines from the second deployment had excellent horizontal coverage and modest vertical smearing that could have been reduced by wider aperture. A wider aperture would also have decreased the minor velocity-depth tradeoff encountered during tomography. A grid of densely sampled lines, as opposed to a 2-D areal grid, was sufficient for imaging, likely because the velocity model was simple and easy to resolve. More complete areal coverage may be needed if significant 2-D or 3-D velocity structure exists. While temporal sampling was the limiting factor for AIDA migration resolution, denser station spacing would become the limiting factor if very high frequencies were recorded.

The rapid deployment of a large numbers of stations is possible by using controlled-source instruments. However, the current instruments in the IRIS pool have limited memory and power, requiring reduced temporal sampling and a short deployment duration. They are not three-component or capable of recording strong ground motions. Overcoming these limitations would enable high-resolution imaging of aftershock sequences. This could allow comprehensive

of stress release in the aftershock zone at the 100-meter scale, improving our understanding of fault mechanics and the strain transient.

4.9 Acknowledgements

Funding was provided by NSF grants EAR-1160666 (RAPID) and EAR-1215739 to Virginia Tech and EAR-1060663 (RAPID) to Cornell University. We used EarthScope Flexible Array instruments and technical support from IRIS PASSCAL.

4.10 References

Artman, B., Podladtchikov, I., and Witten, B. (2010), Source location using time-reverse imaging, *Geophysical Prospecting*, *58*(5), 861-873.

Baysal, E., Kosloff, D., and Sherwood, J. (1983), Reverse time migration, *GEOPHYSICS*, *48*(11), 1514-1524, doi:doi:10.1190/1.1441434.

Bollinger, G. (1969), Seismicity of the central Appalachian states of Virginia, West Virginia, and Maryland—1758 through 1968, *Bulletin of the Seismological Society of America*, *59*(5), 2103-2111.

Bollinger, G., and Sibol, M. (1985), Seismicity, seismic reflection studies, gravity and geology of the central Virginia seismic zone: Part I. Seismicity, *Geological Society of America Bulletin*, *96*(1), 49-57.

Chambers, K., Kendall, J., Brandsberg-Dahl, S., and Rueda, J. (2010), Testing the ability of surface arrays to monitor microseismic activity, *Geophysical Prospecting*, *58*(5), 821-830.

Chang, W.-F., and Mcmechan, G. A. (1991), Wavefield extrapolation of body waves for 3-D imaging of earthquake sources, *Geophysical Journal International*, *106*(1), 85-98, doi:10.1111/j.1365-246X.1991.tb04603.x.

Chang, W., and Mcmechan, G. (1987), Elastic reverse-time migration, *GEOPHYSICS*, *52*(10), 1365-1375, doi:doi:10.1190/1.1442249.

Chapman, M. C. (2013), On the Rupture Process of the 23 August 2011 Virginia Earthquake, *Bulletin of the Seismological Society of America*, *103*(2A), 613-628, doi:10.1785/0120120229.

D'amico, S., Koper, K. D., Herrmann, R. B., Akinci, A., and Malagnini, L. (2010), Imaging the rupture of the Mw 6.3 April 6, 2009 L'Aquila, Italy earthquake using back-projection of teleseismic P-waves, *Geophysical Research Letters*, *37*(3), L03301.

Gajewski, D., and Tessmer, E. (2005), Reverse modelling for seismic event characterization, *Geophysical Journal International*, *163*(1), 276-284.

Ishii, M., Shearer, P. M., Houston, H., and Vidale, J. E. (2005), Extent, duration and speed of the 2004 Sumatra-Andaman earthquake imaged by the Hi-Net array, *Nature*, *435*(7044), 933-936, doi:http://www.nature.com/nature/journal/v435/n7044/suppinfo/nature03675_S1.html.

Ishii, M., Shearer, P. M., Houston, H., and Vidale, J. E. (2007), Teleseismic P wave imaging of the 26 December 2004 Sumatra-Andaman and 28 March 2005 Sumatra earthquake ruptures using the Hi-net array, *Journal of Geophysical Research: Solid Earth*, *112*(B11), B11307, doi:10.1029/2006JB004700.

Jakka, R., Cochran, E., and Lawrence, J. (2010), Earthquake source characterization by the isochrone back projection method using near-source ground motions, *Geophysical Journal International*, *182*(2), 1058-1072.

Kim, W.-Y., and Chapman, M. (2005), The 9 December 2003 Central Virginia Earthquake Sequence: A Compound Earthquake in the Central Virginia Seismic Zone, *Bulletin of the Seismological Society of America*, *95*(6), 2428-2445, doi:10.1785/0120040207.

Kiser, E., Ishii, M., Langmuir, C. H., Shearer, P. M., and Hirose, H. (2011), Insights into the mechanism of intermediate-depth earthquakes from source properties as imaged by back projection of multiple seismic phases, *Journal of Geophysical Research: Solid Earth*, *116*(B6), B06310, doi:10.1029/2010JB007831.

Mcmechan, G. A. (1982), Determination of source parameters by wavefield extrapolation, *Geophysical Journal of the Royal Astronomical Society*, *71*(3), 613-628, doi:10.1111/j.1365-246X.1982.tb02788.x.

Mcmechan, G. A., Luetgert, J. H., and Mooney, W. D. (1985), Imaging of earthquake sources in Long Valley Caldera, California, 1983, *Bulletin of the Seismological Society of America*, *75*(4), 1005-1020.

Munsey, J. W., and Bollinger, G. (1985), Focal mechanism analyses for Virginia earthquakes (1978-1984), *Bulletin of the Seismological Society of America*, *75*(6), 1613-1636.

Pratt, T. L., Çoruh, C., Costain, J. K., and Glover, L. (1988), A geophysical study of the Earth's crust in central Virginia: Implications for Appalachian crustal structure, *Journal of Geophysical Research: Solid Earth*, *93*(B6), 6649-6667, doi:10.1029/JB093iB06p06649.

Xu, X., Wen, X., Yu, G., Chen, G., Klinger, Y., Hubbard, J., and Shaw, J. (2009), Coseismic reverse-and oblique-slip surface faulting generated by the 2008 Mw 7.9 Wenchuan earthquake, China, *Geology*, *37*(6), 515-518.

Zhebel, O., and Eisner, L. (2012), Simultaneous microseismic event localization and source mechanism determination, in *SEG Technical Program Expanded Abstracts 2012*, edited, pp. 1-5, Society of Exploration Geophysicists.

Zhu, J., and Lines, L. R. (1998), Comparison of Kirchhoff and reverse-time migration methods with applications to prestack depth imaging of complex structures, *Geophysics*, *63*(4), 1166-1176, doi:10.1190/1.1444416.

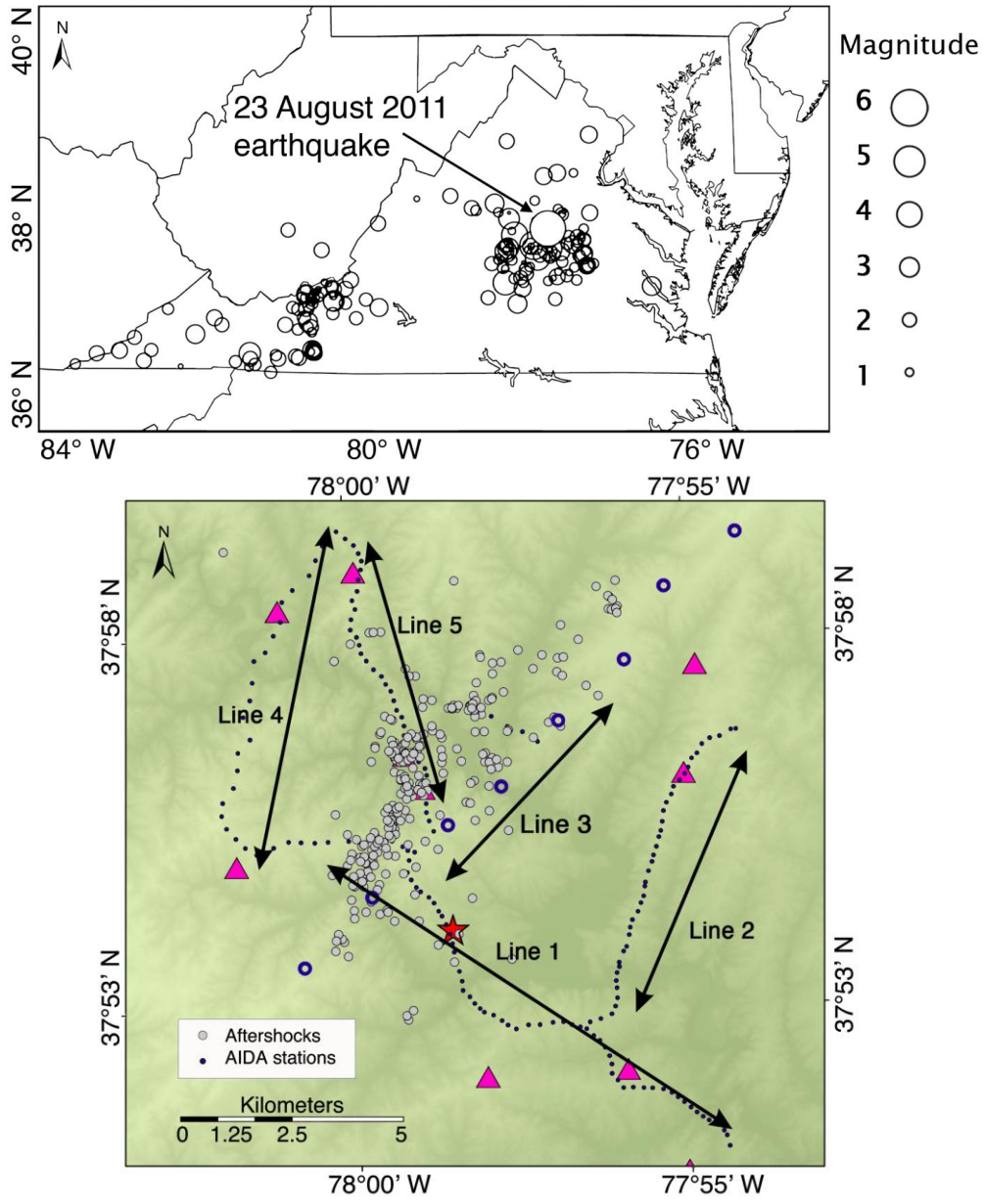

Figure 4.1 (a) Seismicity of Virginia from 1977 to 2011, including the central Virginia seismic zone. (b) Map of AIDA aftershock array (black points). Lines 1 and 2 were deployed during the first 6 days, Lines 3, 4, 5, and 6 were added during the second 6 days. The 2011 M5.8

event is the white star. Aftershocks (small squares OR whatever symbol is used) are from Davenport et al. [2014].

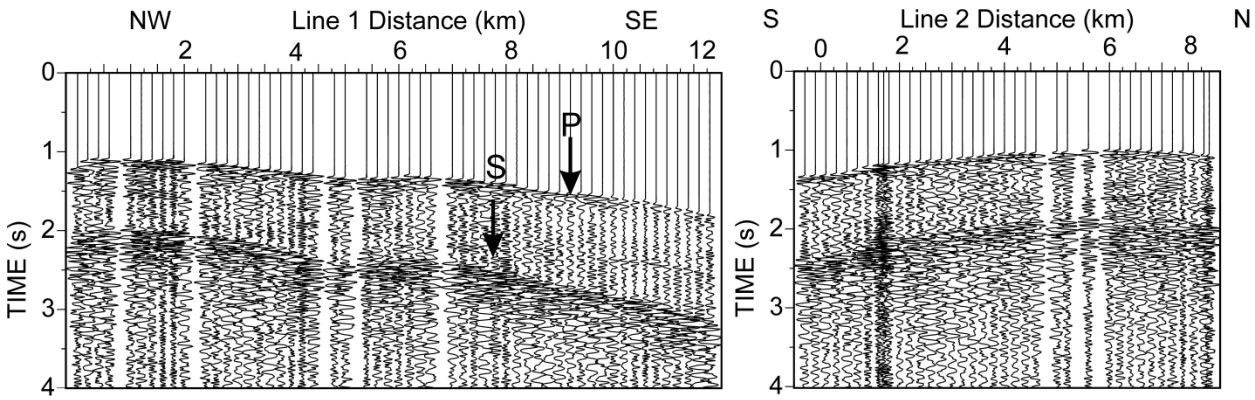

Magnitude 3.7 Sep 1,2011 09:09:38-09:09:43 UTC

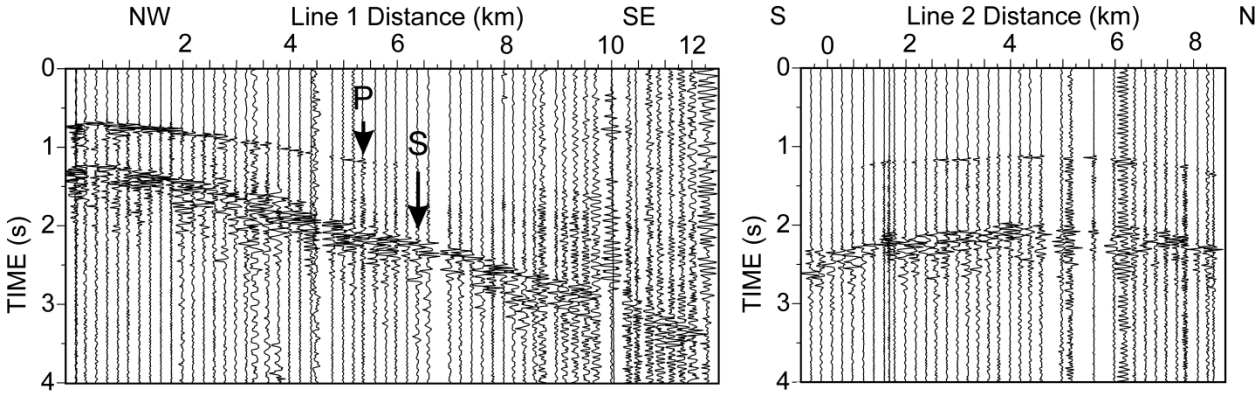

Magnitude -0.1 Aug 29,2011 01:50:52-01:50:57 UTC

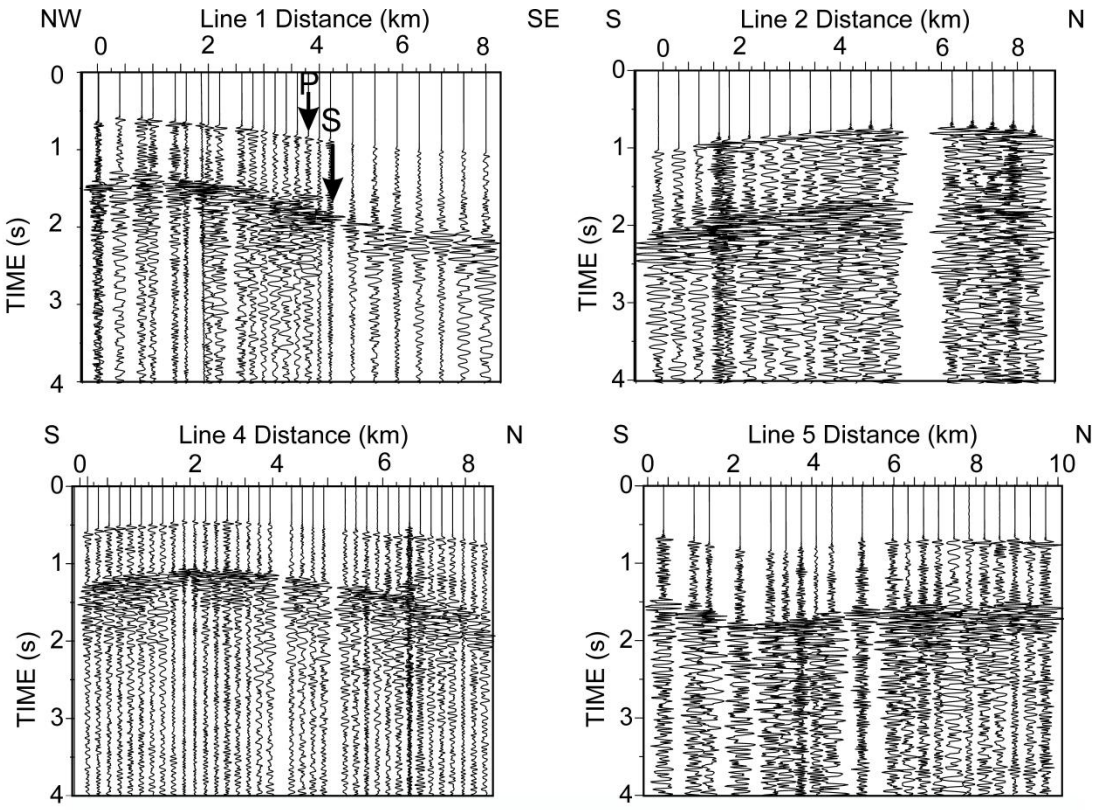
NW
Line 1 Distance (km)
SE
S
Line 2 Distance (km)
N
S
Line 4 Distance (km)
N
S
Line 5 Distance (km)
N
TIME (s)
P
S
Magnitude 2.5 Sep 5,2011 16:54:54-16:54:59 UTC

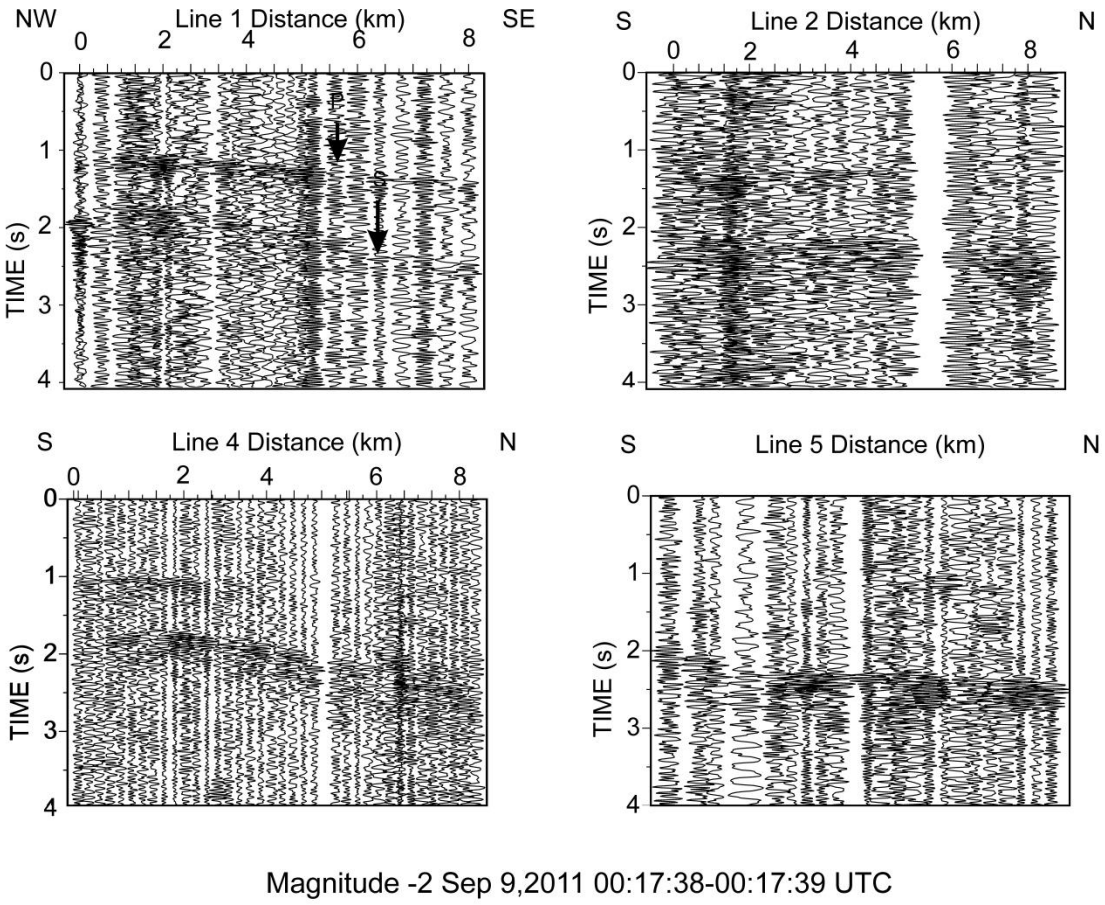

Figure 4.2 Aftershock data from AIDA for events of magnitude (a) 3.7 and (b) –0.1 recorded during week one, and (c) 2.6, and (d) –2 during week two. The lines recorded by AIDA were different for each week. For each event, the data are scaled to true relative amplitude, but each event is scaled separately. The data are unfiltered except to remove a 0 Hz signal. The trace start time is not the earthquake time.

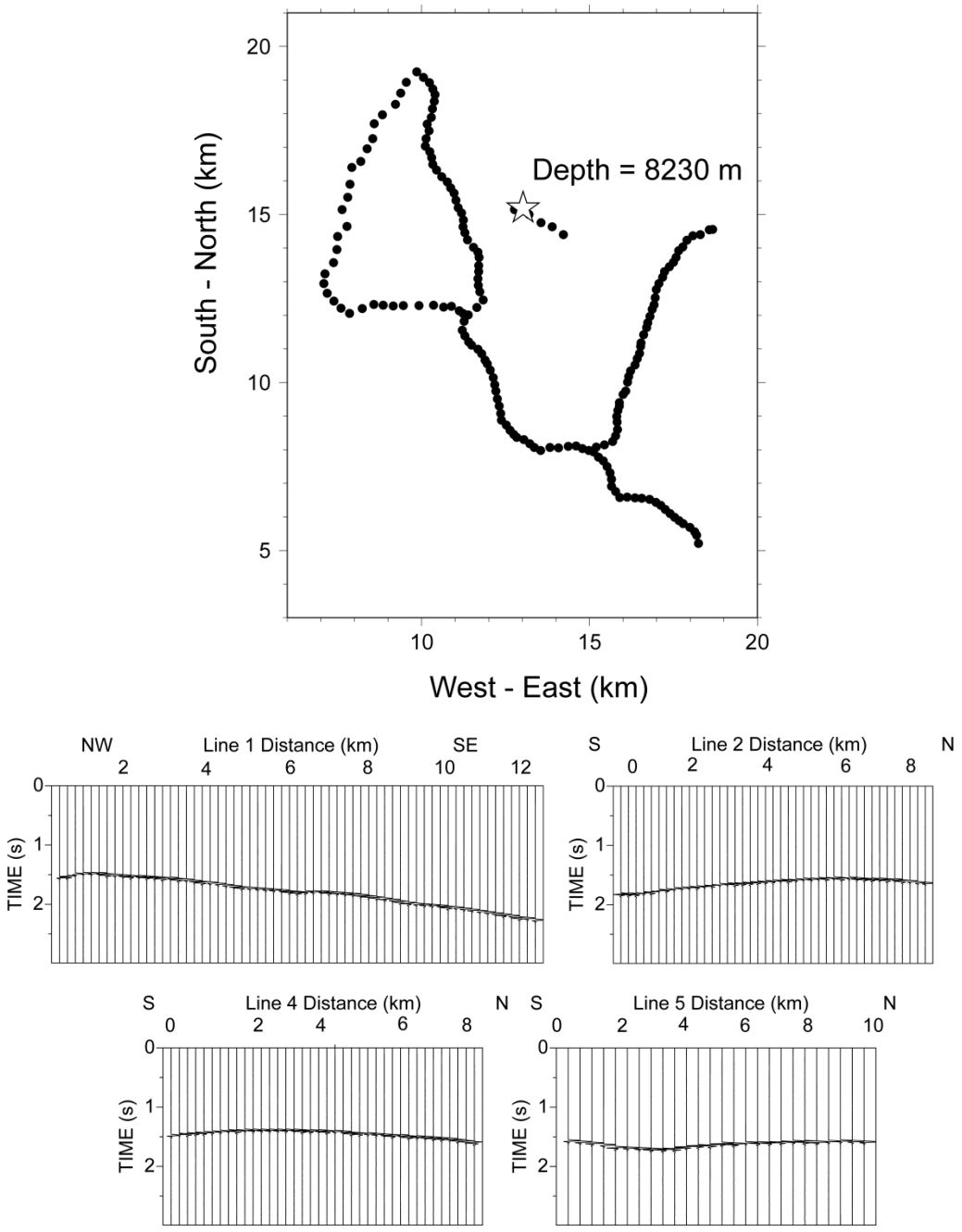

Figure 4.3 Synthetic data for a point source. (a) Location map. The source is the star and AIDA stations are the black circles. (b) Synthetic data anti-alias filtered to a sampling rate of 100 samples per second.

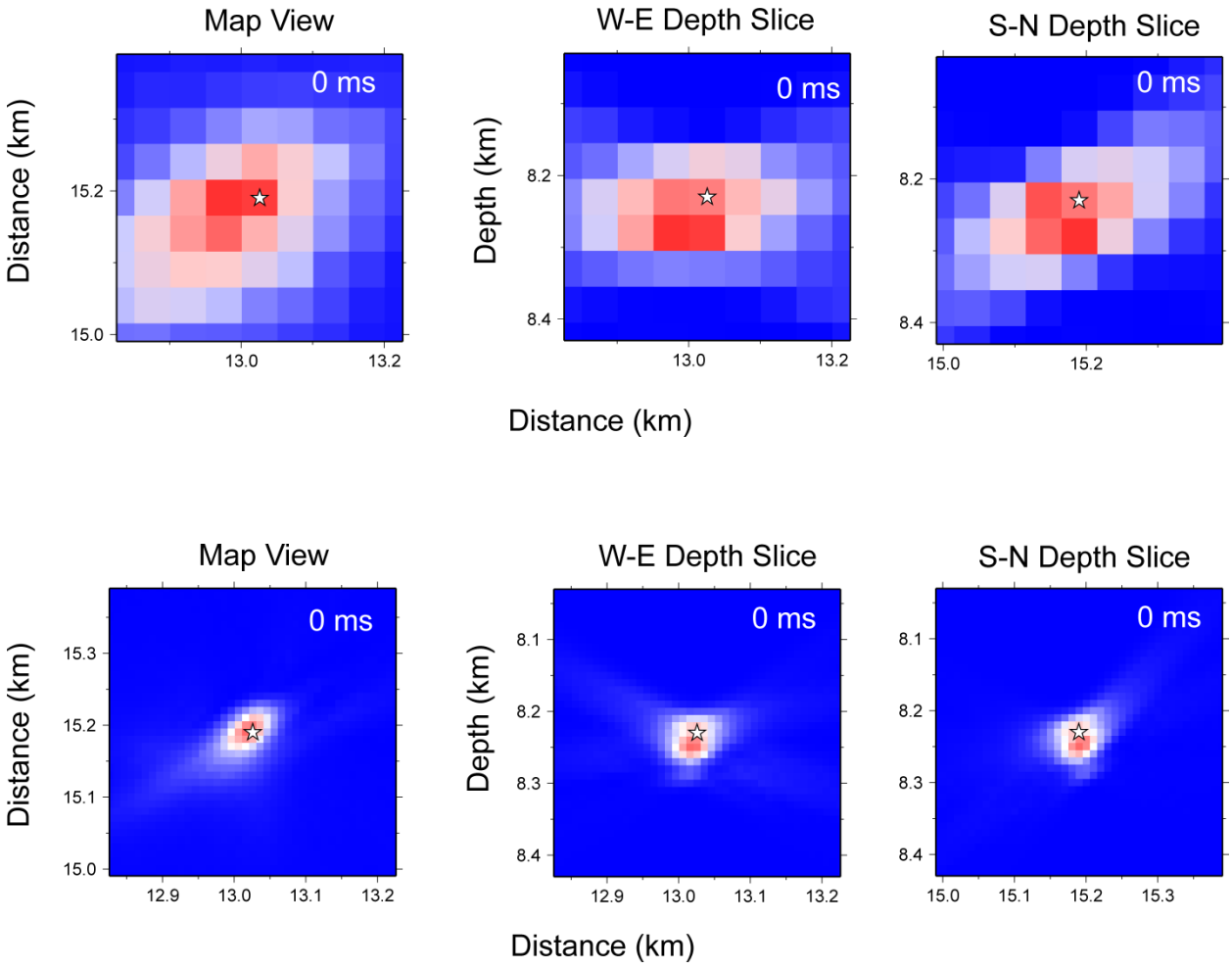

Figure 4.4 Reverse time migration of the point source synthetic data of Figure 4.3. (a) Results for data anti-aliased filtered for a sampling rate of 100 samples per second. (b) Results for data anti-alias filtered for 500 samples per second.

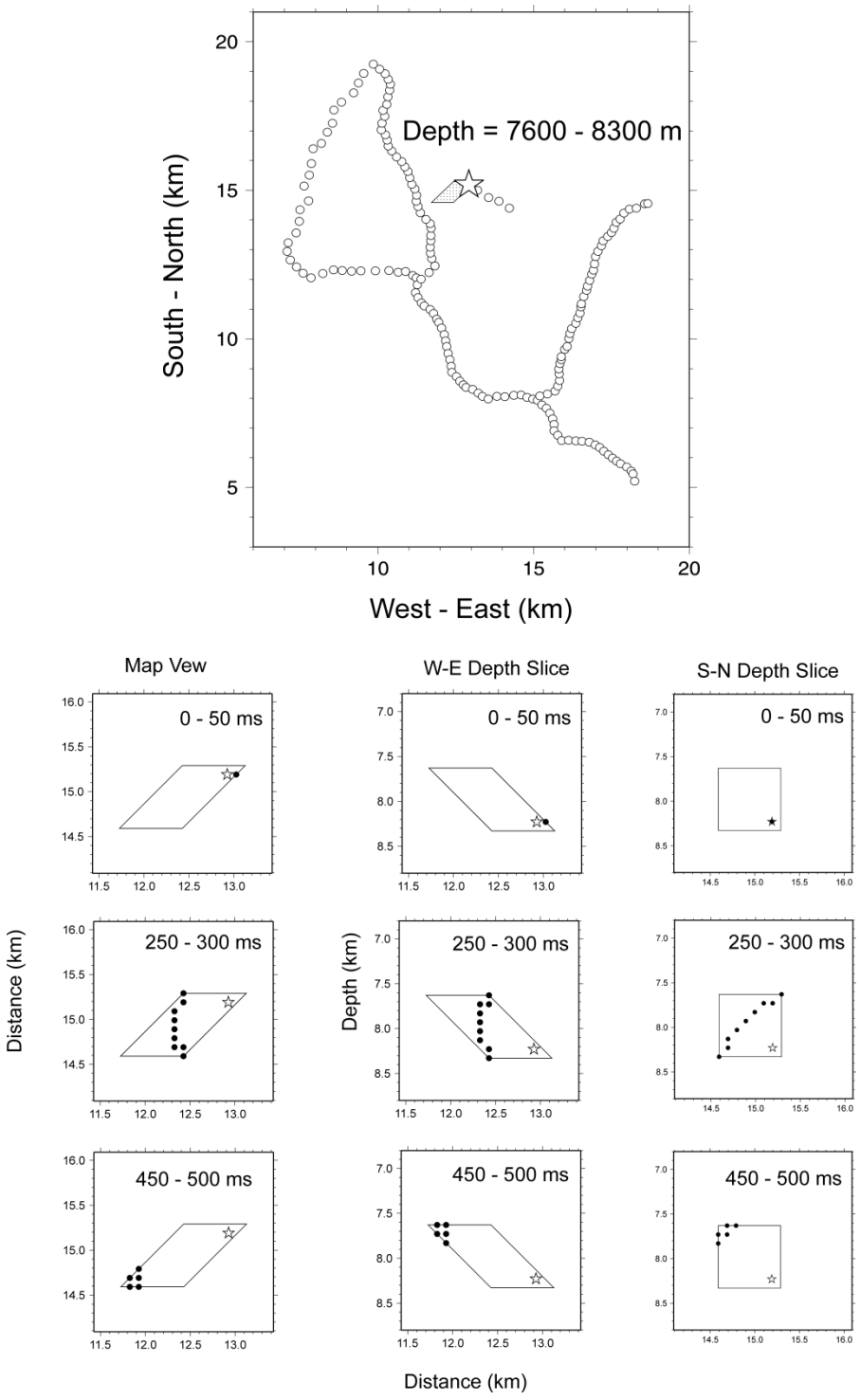
Depth = 7600 - 8300 m
South - North (km)
West - East (km)
Map Vew
W-E Depth Slice
S-N Depth Slice
0 - 50 ms
250 - 300 ms
450 - 500 ms
Distance (km)
Depth (km)
Distance (km)

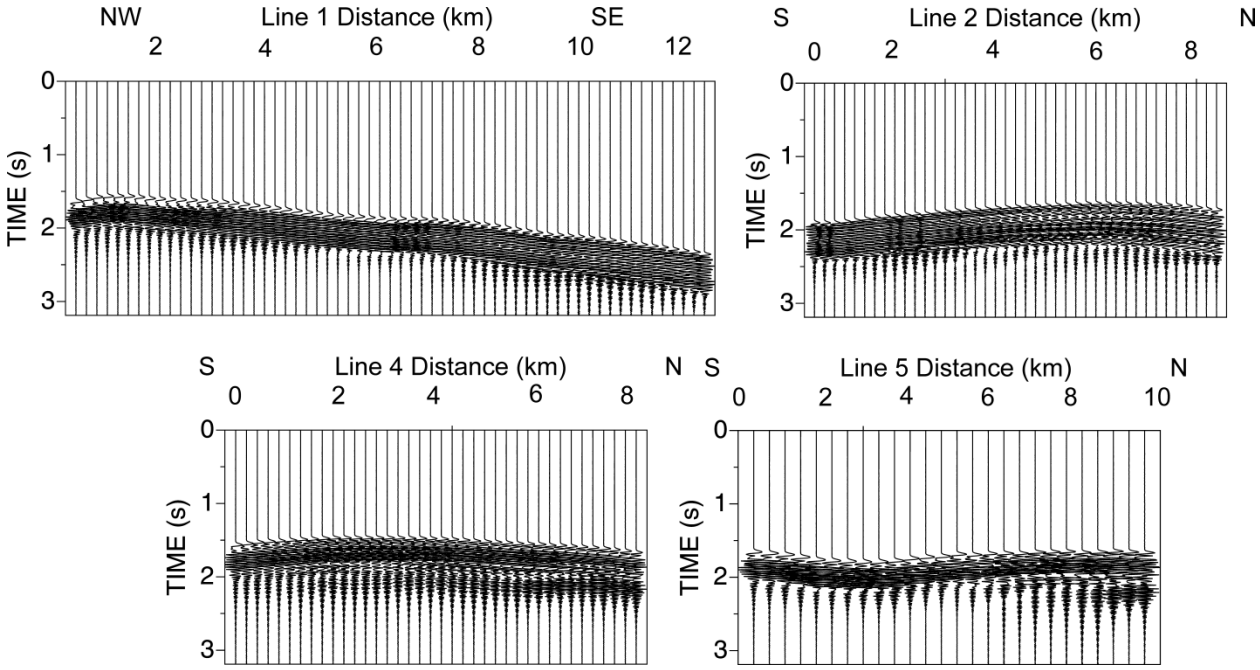

Figure 4.5 . (a) Results for data anti-aliased filtered for a sampling rate of 100 samples per second. (b) Results for data anti-alias filtered for 500 samples per second. (a) Location map. The hypocenter is the star and 64 sub-events are black points. (b) Cross-sections for 50 ms time windows showing sub-events at 100 m spacing. Rupture propagates at 2.7 km/s to trigger the sub-events. (c) Synthetic data anti-alias filtered to a sampling rate of 100 samples per second.

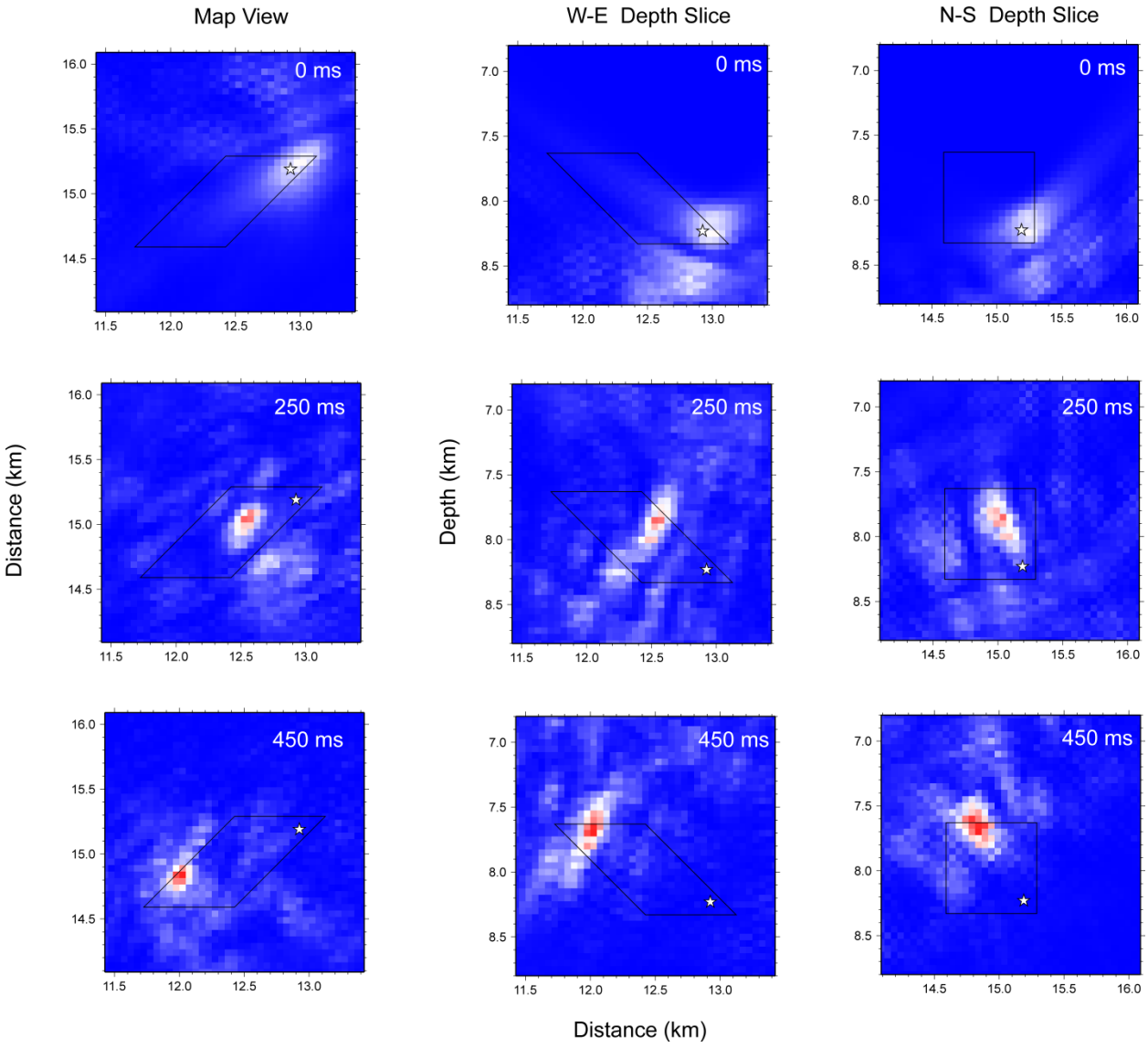

Figure 4.6 RTM images at different times of the fault data of Figure 4.5.

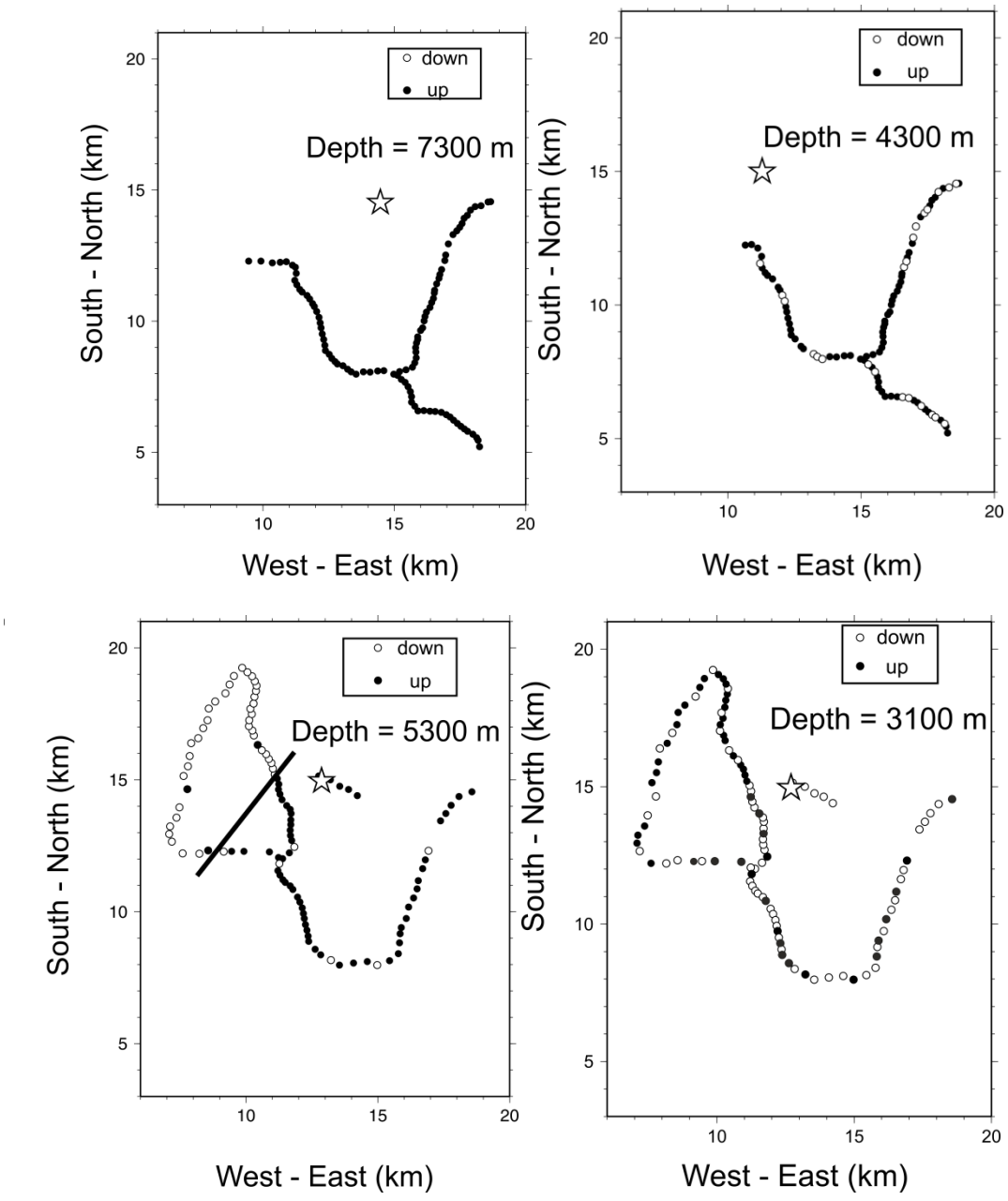

Figure 4.7 Station maps showing the direction of first motion for the aftershocks shown in Figure 2. Upward first motions are black and downward are hollow circles. The epicenters are stars. The thick black lines show the local strike of the focal planes, where constrained to cross the AIDA array.

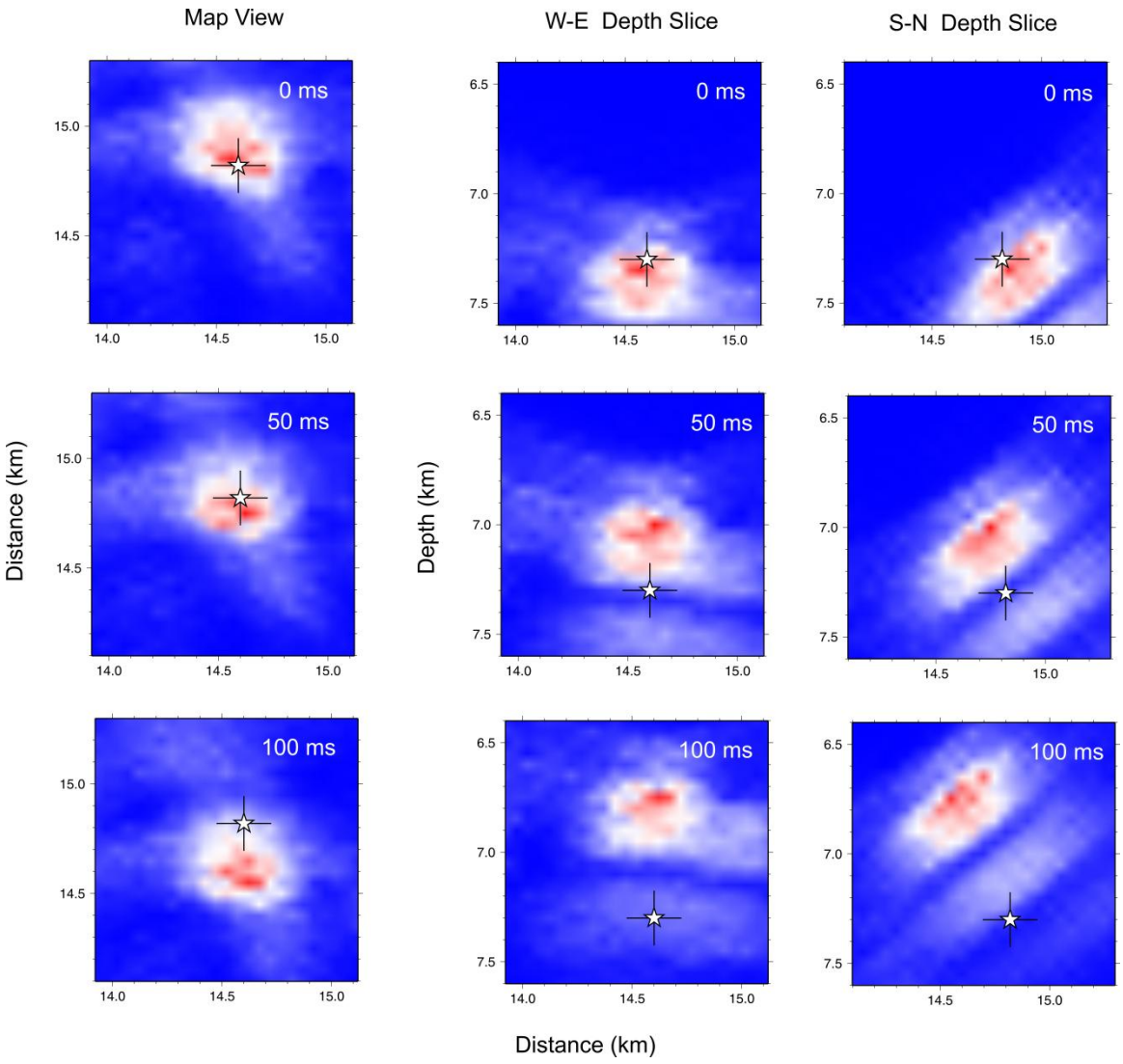

Figure 4.8 images at different times for the magnitude 3.7 aftershock of Figures 4.2a and 4.7a. The cross-hairs indicate the location of the initial energy peak. The star is the hypocenter.

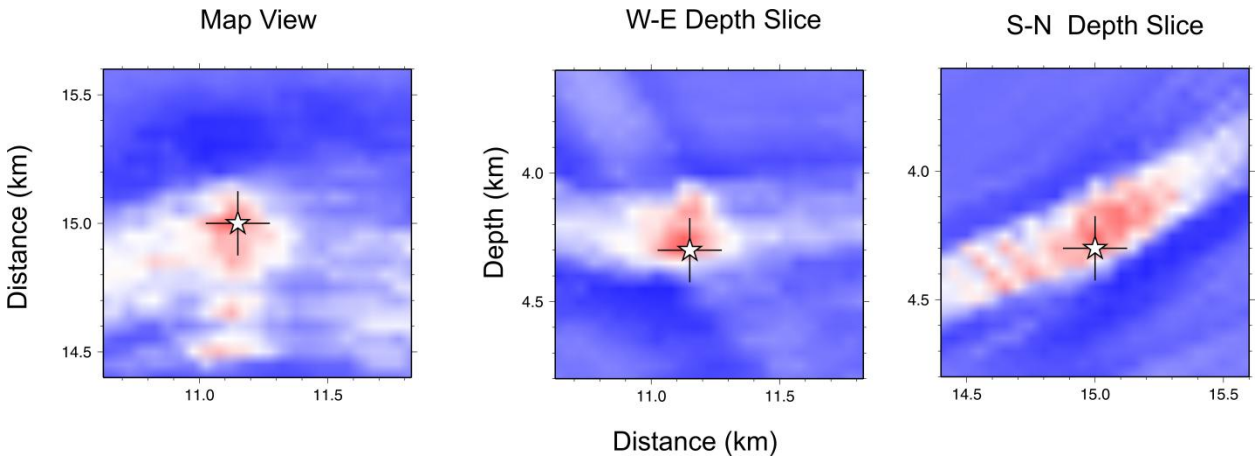

Figure 4.9 Migrated images at different times for the magnitude 3.7 aftershock of Figures 4.2a and 4.7a. The cross-hairs indicate the location of the initial energy peak. The star is the hypocenter.

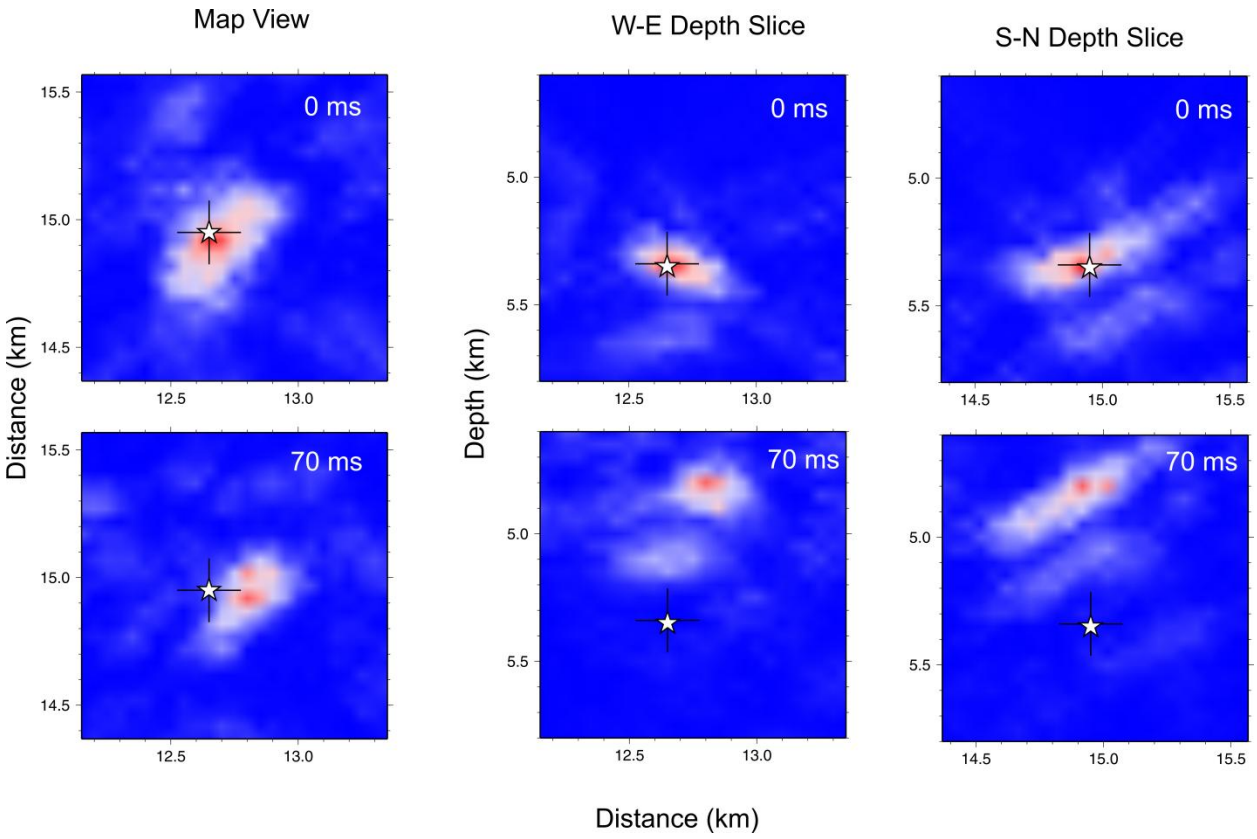

Figure 4.10 Migrated images at different times for the magnitude 2.6 aftershock of Figures 4.2c and 4.7c.

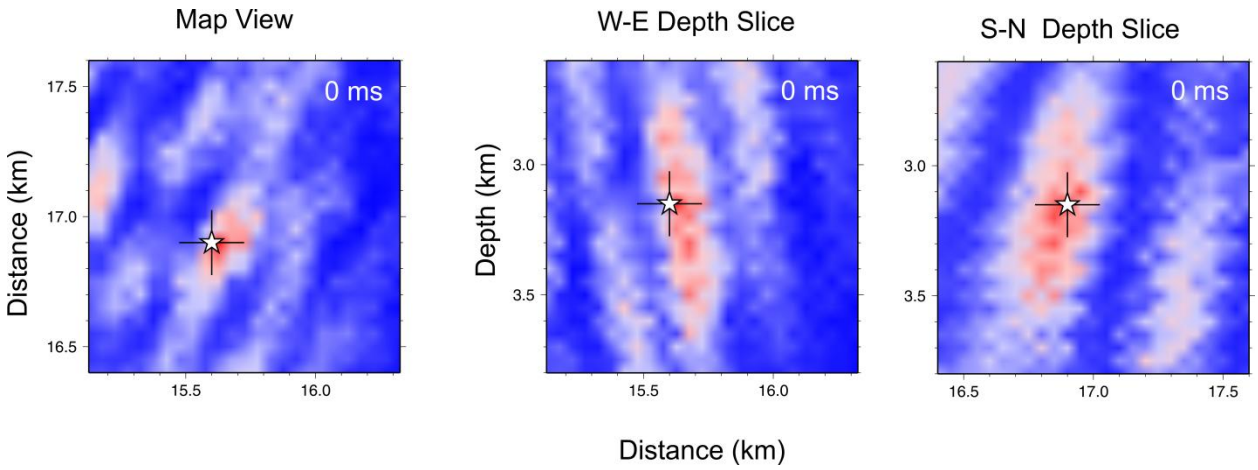

Figure 4.11 Migrated images at different times for the magnitude -2 aftershock of Figures 2d and 7d.

Chapter 5. Discussion

5.1 Future Work for the Batholith Project

Generation and evolution of continental arc crust are the fundamental and long term problem in geophysics and geology. In order to study the process of the continental crust formation from the magma derived from the mantle and the fate of the complementary ultra-mafic residue generated during the melting [*Kay and Mahlburg-Kay*, 1991; *Kay and Mahlburg Kay*, 1993],multi-discipline projects [*Yuan et al.*, 1992; *Spence and Long*, 1995; *Zelt et al.*, 1996; *Morozov et al.*, 1998; *Zhang*, 1998; *Zelt*, 1999; *Morozov et al.*, 2001; *Clowes et al.*, 2005; *Stephenson et al.*, 2011; *Bustin et al.*, 2013] have been carried on applying different research methods [*Ducea*, 2002; *Gehrels et al.*, 2009; *Calkins et al.*, 2010; *Cecil et al.*, 2011] to analyze the Coast Mountain Batholith, which is the largest Phanerozoic arc complex and was generated by several pulses of magmatim during rapid subduction of Pacific basin plates beneath the North American margin [*Monger et al.*, 1982; *Armstrong*, 1988].

The high velocity zone under the younger CPC indicated by the P wave and S wave velocity is critical to understand the crustal evolution process in the arc area. The composition of this high velocity zone is interpreted as representing a bulk composition of mafic garnet granulite. which is confirmed by the Vp/Vs ratio and tel-seismic study in the study area [*Calkins et al.*, 2010]. This garnet granulite and large volumes of granodiorite-dominated melt were created by arc dehydration melting of amphibolite (or hydrated gabbro) in the pre-existing lower crust [*Beard and Lofgren*, 1991; *Douce and Beard*, 1995]. On the other hand, in order to provide

more composition constraint on this high velocity mafic residue, integration analysis with other Batholith project dataset based on the previous seismic velocity model should be the next research direction. Since the seismic line was mainly east to west direction, the extension of the mafic residue is mainly constraint by the lower crust reflection and refraction in east to west direction, so the north to south extension of the residue should be detected in the future study as well which could provide more accurate volume estimation of the residue. During the shear wave modeling, because only vertical component S wave has been applied to the modeling, the signal to noise ratio significantly reduces the resolution of the S wave velocity model since larger scale smooth was utilized. Particularly, in the upper mantle level, the ray coverage of the Sn is very sparse which could not provide accurate enough estimation of the upper mantle velocity and the Vp/Vs ratio. However, the upper mantle velocity just below the mantle, especially for the part under the younger CPC, is critical to the estimation of the upper mantle structure and composition as well as the interpretation of the crust evolution.

By subtracting the lateral variations in crustal velocity and thickness provided by the active source velocity model, velocity model derived from passive source broadband sesimic data with longer period could be used to delineate the upper mantle structure and composition [*Calkins et al.*, 2010]. Density analysis is another method worth to be applied. Gravity inversion modeling method could provide crustal density model which is important to estimate if a mass excess indicative mafic residue is present below the younger CPC [*Bustin et al.*, 2013]. The north to south extension of the residue could be estimated as well. By comparing the density modeling result to the laboratory rock density measurement under similar underground pressure and temperature, more critical composition constraint of this mafic residue is expected.

After the conformation of the volume and composition estimation from gravity analysis, the petrological model should be built based on the geophysical modeling result to interpret the fate of the mafic residue during the formation and deformation of the arc process. Other than only focusing on silicic melt that was extracted from the dehydration melting in the lower arc crust, the mafic to ultramafic residue formed by the extraction of silicic melt from gabbroic melt in the lower crust level should also be considered [*Ducea*, 2002; *Hollister and Andronicos*, 2006]. The two phase including tranpression and tranextension process during the accretion and arc collapse of the continental crust evolution process could be relative to the fate the mafic residue under the younger CPC as well as other geology model in the study area [Monger and Brown, in press].

5.2 Future Work for the Reverse Time Migration Application on Earthquake Process

Previous study has already demonstrated that, the reverse time migration method was an efficient way of analyzing large earthquakes [*Ishii et al.*, 2005; 2007; *Kiser et al.*, 2011]. Here based on both the synthetic and real data analysis, the reverse time migration method has been proved to be a critical method worth to be applied in the future research on the analysis of the aftershock process as well as microseismic analysis [*Mcmechan*, 1982; *Mcmechan et al.*, 1985; *Chang and Mcmechan*, 1991]. The conclusion derived from chapter 3 demonstrated several ways to improve the resolution of the method application in future studies.

The 100 samples/s AIDA data was proved to be too low to record the whole signal of the larger magnitude aftershocks as well as decreasing both the time and spatial resolution of the reverse time migration method. Higher frequency data which could prevent the amplitude clips of the larger magnitude aftershocks as well as the time alias of the seismic data is worth to be recorded in the future. Full waveform migration or inversion could also be tested if the amplitude of the earthquake could be recorded completely. Larger volume memory card and better battery should be utilized to improve the receiver's longevity and the deployment efficiency.

The result from the reverse time migration application to the AIDA data also indicated that besides increasing the frequency of the data, large number of stations is another critical effect to the image resolution. The AIDA data demonstrated that large number of stations deployed with ideal station space could effectively prevent the spatial alias of the seismic data. Meanwhile, more stations extending longer distance could provide better wiggle curvature. All the factors mentioned above are very important to increase image resolution during the stack of the reverse time migration. On the other hand, more portable stations with smaller size but stronger battery is requested as well as good deployment plan before the survey for larger number of the stations deployment.

During the data processing of the reverse time migration, accurate velocity and super computer are the two main factors [*Zhu and Lines*, 1998]. Velocity model derived from the local high resolution travel time tomography was applied to the migration. As the development of the super computer in the past few years, GPU computing application has been applied more and more in the super computing algorithms. Compared to the traditional supper computer cluster, the GPU machine requires smaller space, lower price but could provide faster computing speed,

because there is no data communication between each thread during the migration on each grid point, which perfectly fits the requirement that data parallel preferred of GPU programming. The application of thousands of threads during the calculation will greatly reduce the calculation time especially when smaller grid space with higher sampling rate was used and the full waveform was applied. In advance, the application of super computer with large amount of memory on reverse time migration could also handle large amount of data to auto detect the very smaller magnitude earthquakes in a very long period.

The reverse time migration algorithm itself could also be improved in the future,. Different kind of stack method [*Anikiev et al.*; *Artman et al.*, 2010] has already been applied in the industry micro seismic area focusing on different type of seismic data such as borehole deployment, micro earthquake sources and hydraulic fracturing [*Chambers et al.*, 2010; *Artman et al.*, 2010; *Zhebel and Eisner*, 2012; *Chambers et al.*, 2013]. Both P and S wave could be utilized during the migration. The P and S wave adjoint migration may be the new research direction, which may be able to provide more accurate earthquake location and process analysis, leading to better isotropic estimation images.

The application of reverse time migration to the AIDA data in chapter 3 has already demonstrated that with a good waveform analysis such as cross correlation, the focal mechanism of the earthquake could be calculated before the migration as an extra bonus of the algorithm. But the accuracy of the calculation result of the polarity is greatly affected by the signal to noise ratio , and it will eventually affect the reverse time migration result by changing the weighting factor during the stack [Ishii et al., 2007]. Better polarity analysis algorithm [*Anikiev et al.*] is preferred rather than the simple cross correlation method, especially when the imaging process

was applied to the tiny aftershocks. Meanwhile, new data mining algorithm fitting to parallel computing is worth to be tested on more large amount data with higher frequency, because the higher the frequency is, the more complex the waveform will be. The real data analysis of AIDA geometry result also illustrated that, only when the receivers was set on the different focal planes of the earthquakes, the different polarities of the stations could be observed during the calculation. Better deployment plan is required before the field work in the future studies.

When all the details about the program has been considered and resolved, the program could be applied to a large amount of data, working on both detecting very tiny aftershocks and imaging the rupture propagation directions. By comparing the location of all the aftershocks and the energy moving direction of the larger aftershocks, the relationship between the fault systems and the aftershock zone could be revealed [Ishii et al., 2005; Ishii et al., 2007].

5.3 References

Anikiev, D., Stanek, F., Valenta, J., and Eisner, L. Imaging microseismic events by diffraction stacking with moment tensor inversion, in *SEG Technical Program Expanded Abstracts 2013*, edited, pp. 2013-2018, doi:doi:10.1190/segam2013-0830.1.

Armstrong, R. L. (1988), Mesozoic and early Cenozoic magmatic evolution of the Canadian Cordillera, *Geological Society of America Special Papers*, *218*, 55-92, doi:10.1130/SPE218-p55.

Artman, B., Podladtchikov, I., and Witten, B. (2010), Source location using time-reverse imaging, *Geophysical Prospecting*, *58*(5), 861-873.

Beard, J. S., and Lofgren, G. E. (1991), Dehydration Melting and Water-Saturated Melting of Basaltic and Andesitic Greenstones and Amphibolites at 1, 3, and 6. 9 kb, *Journal of Petrology*, *32*(2), 365-401.

Bustin, A. M. M., Clowes, R. M., Monger, J. W. H., and Journeay, J. M. (2013), The southern Coast Mountains, British Columbia: New interpretations from geological, seismic reflection, and gravity data, *Canadian Journal of Earth Sciences*, *50*(10), 1033-1050, doi:10.1139/cjes-2012-0122.

Calkins, J. A., Zandt, G., Girardi, J., Dueker, K., Gehrels, G. E., and Ducea, M. N. (2010), Characterization of the crust of the Coast Mountains Batholith, British Columbia, from P to S converted seismic waves and petrologic modeling, *Earth and Planetary Science Letters*, *289*(1–2), 145-155, doi:http://dx.doi.org/10.1016/j.epsl.2009.10.037.

Cecil, M. R., Gehrels, G., Ducea, M. N., and Patchett, P. J. (2011), U-Pb-Hf characterization of the central Coast Mountains batholith: Implications for petrogenesis and crustal architecture, *Lithosphere*, *3*(4), 247-260, doi:10.1130/l134.1.

Chambers, K., Clarke, J., and Wilson, S. (2013), Imaging Moment Tensors from Surface Arrays, paper presented at 4th EAGE Passive Seismic Workshop.

Chambers, K., Kendall, J., Brandsberg-Dahl, S., and Rueda, J. (2010), Testing the ability of surface arrays to monitor microseismic activity, *Geophysical Prospecting*, *58*(5), 821-830.

Chang, W.-F., and Mcmechan, G. A. (1991), Wavefield extrapolation of body waves for 3-D imaging of earthquake sources, *Geophysical Journal International*, *106*(1), 85-98, doi:10.1111/j.1365-246X.1991.tb04603.x.

Clowes, R. M., Hammer, P. T. C., Fernández-Viejo, G., and Welford, J. K. (2005), Lithospheric structure in northwestern Canada from Lithoprobe seismic refraction and related studies: a synthesis, *Canadian Journal of Earth Sciences*, *42*(6), 1277-1293, doi:10.1139/e04-069.

Douce, A. E. P., and Beard, J. S. (1995), Dehydration-melting of biotite gneiss and quartz amphibolite from 3 to 15 kbar, *Journal of Petrology*, *36*(3), 707-738.

Ducea, M. N. (2002), Constraints on the bulk composition and root foundering rates of continental arcs: A California arc perspective, *J. Geophys. Res.*, *107*(B11), 2304, doi:10.1029/2001JB000643.

Gehrels, G., Rusmore, M., Woodsworth, G., Crawford, M., Andronicos, C., Hollister, L., Patchett, J., Ducea, M., Butler, R., Klepeis, K., Davidson, C., Friedman, R., Haggart, J.,

Mahoney, B., Crawford, W., Pearson, D., and Girardi, J. (2009), U-Th-Pb geochronology of the Coast Mountains batholith in north-coastal British Columbia: Constraints on age and tectonic evolution, *Geological Society of America Bulletin*, *121*(9-10), 1341-1361, doi:10.1130/b26404.1.

Hollister, L. S., and Andronicos, C. L. (2006), Formation of new continental crust in Western British Columbia during transpression and transtension, *Earth and Planetary Science Letters*, *249*(1–2), 29-38, doi:http://dx.doi.org/10.1016/j.epsl.2006.06.042.

Ishii, M., Shearer, P. M., Houston, H., and Vidale, J. E. (2005), Extent, duration and speed of the 2004 Sumatra-Andaman earthquake imaged by the Hi-Net array, *Nature*, *435*(7044), 933-936, doi:http://www.nature.com/nature/journal/v435/n7044/suppinfo/nature03675_S1.html.

Ishii, M., Shearer, P. M., Houston, H., and Vidale, J. E. (2007), Teleseismic P wave imaging of the 26 December 2004 Sumatra-Andaman and 28 March 2005 Sumatra earthquake ruptures using the Hi-net array, *Journal of Geophysical Research: Solid Earth*, *112*(B11), B11307, doi:10.1029/2006JB004700.

Kay, R., and Mahlburg-Kay, S. (1991), Creation and destruction of lower continental crust, *Geologische Rundschau*, *80*(2), 259-278.

Kay, R. W., and Mahlburg Kay, S. (1993), Delamination and delamination magmatism, *Tectonophysics*, *219*(1), 177-189.

Kiser, E., Ishii, M., Langmuir, C. H., Shearer, P. M., and Hirose, H. (2011), Insights into the mechanism of intermediate-depth earthquakes from source properties as imaged by back

projection of multiple seismic phases, *Journal of Geophysical Research: Solid Earth*, *116*(B6), B06310, doi:10.1029/2010JB007831.

Mcmechan, G. A. (1982), Determination of source parameters by wavefield extrapolation, *Geophysical Journal of the Royal Astronomical Society*, *71*(3), 613-628, doi:10.1111/j.1365-246X.1982.tb02788.x.

Mcmechan, G. A., Luetgert, J. H., and Mooney, W. D. (1985), Imaging of earthquake sources in Long Valley Caldera, California, 1983, *Bulletin of the Seismological Society of America*, *75*(4), 1005-1020.

Monger, J. W. H., Price, R. A., and Tempelman-Kluit, D. J. (1982), Tectonic accretion and the origin of the two major metamorphic and plutonic welts in the Canadian Cordillera, *Geology*, *10*(2), 70-75, doi:10.1130/0091-7613(1982)10<70:taatoo>2.0.co;2.

Morozov, I. B., Smithson, S. B., Chen, J., and Hollister, L. S. (2001), Generation of new continental crust and terrane accretion in Southeastern Alaska and Western British Columbia: constraints from P- and S-wave wide-angle seismic data (ACCRETE), *Tectonophysics*, *341*(1-4), 49-67.

Morozov, I. B., Smithson, S. B., Hollister, L. S., and Diebold, J. B. (1998), Wide-angle seismic imaging across accreted terranes, southeastern Alaska and western British Columbia, *Tectonophysics*, *299*(4), 281-296.

Spence, G. D., and Long, D. T. (1995), Transition from oceanic to continental crustal structure: seismic and gravity models at the Queen Charlotte transform margin, *Canadian Journal of Earth Sciences*, *32*(6), 699-717, doi:10.1139/e95-060.

Stephenson, A. L., Spence, G. D., Wang, K., Hole, J. A., Miller, K. C., Clowes, R. M., Harder, S. H., and Kaip, G. M. (2011), Crustal velocity structure of the southern Nechako basin, British Columbia, from wide-angle seismic traveltime inversion11 This article is one of a series of papers published in this Special Issue on the theme of New insights in Cordilleran Intermontane geoscience: reducing exploration risk in the mountain pine beetle-affected area, British Columbia, *Canadian Journal of Earth Sciences*, *48*(6), 1050-1063, doi:10.1139/e11-006.

Yuan, T., Spence, G., and Hyndman, R. (1992), Structure beneath Queen Charlotte Sound from seismic-refraction and gravity interpretations, *Canadian Journal of Earth Sciences, 29*(7), 1509-1529.

Zelt, B. C., Ellis, R. M., Clowes, R. M., and Hole, J. A. (1996), Inversion of three-dimensional wide-angle seismic data from the southwestern Canadian Cordillera, *J. Geophys. Res.*, *101*(B4), 8503-8529, doi:10.1029/95JB02807.

Zelt, C. A. (1999), Modelling strategies and model assessment for wide-angle seismic traveltime data, *Geophysical Journal International*, *139*(1), 183-204, doi:10.1046/j.1365-246X.1999.00934.x.

Zhang, J. (1998), Inversion of surface wave spectra for source parameters of large earthquakes using aspherical earth models, *Physics of the Earth and Planetary Interiors*, *107*(4), 327-350, doi:http://dx.doi.org/10.1016/S0031-9201(98)00080-6.

Zhebel, O., and Eisner, L. (2012), Simultaneous microseismic event localization and source mechanism determination, in *SEG Technical Program Expanded Abstracts 2012*, edited, pp. 1-5, Society of Exploration Geophysicists.

Zhu, J., and Lines, L. R. (1998), Comparison of Kirchhoff and reverse-time migration methods with applications to prestack depth imaging of complex structures, *Geophysics*, *63*(4), 1166-1176, doi:10.1190/1.1444416.